

© 2020 by Roberto E. Fairhurst Agosta. All rights reserved.

MOLTRES APPLICATION TO PRISMATIC GAS-COOLED REACTORS AND
HIGH-TEMPERATURE HYDROGEN PRODUCTION

BY

ROBERTO E. FAIRHURST AGOSTA

THESIS

Submitted in partial fulfillment of the requirements
for the degree of Master of Science in Nuclear, Plasma, and Radiological Engineering
with a concentration in Computational Science and Engineering
in the Graduate College of the
University of Illinois at Urbana-Champaign, 2020

Urbana, Illinois

Master's Committee:

Assistant Professor Kathryn D. Huff, Advisor
Associate Professor and Associate Head for Undergraduate Programs Tomasz Kozlowski

Abstract

Abstract.

A mi familia, for their unconditional support.

Acknowledgments

I wish to express my gratitude to my advisor Dr. Kathryn Huff, who guided me from my academic beginnings. I would also like to thank Dr. Tomasz Kozlowski for his help and invaluable comments as the second reader of this thesis. I wish to acknowledge Dr. Paul Fischer, Dr. Rizwan Uddin, and Dr. Caleb Brooks for their time and discussions helpful to this work.

Besides the support from several Faculty, this work was possible due to day-to-day motivation from my fellow group-mates Sam Dotson, Greg Westphal, Kip Kleimenhagen, Andrei Rykhlevskii, Gwen Chee, and Sun Myung Park. I also much appreciate Gavin Davis' help with proofreading my writing. Finally, I want to acknowledge my family, who, even though we were more than five thousand miles apart, their support and encouragement were always present. I also wanted to express my gratitude to Daniela Calero for her moral support throughout the pandemic.

Table of Contents

List of Tables	vii
List of Figures	viii
Chapter 1 Introduction	1
1.1 The Prismatic High-Temperature Gas-Cooled Reactor	1
1.2 Motivation	3
1.3 Objectives	4
Chapter 2 Literature Review	7
2.1 Prismatic HTGR Diffusion Solvers	7
2.1.1 Energy group structure analysis	10
2.2 Prismatic HTGR Thermal-fluids	11
2.3 Prismatic HTGR Multi-physics	16
Chapter 3 Methodology	19
3.1 Computational tools	19
3.1.1 MOOSE	19
3.1.2 Moltres	20
3.1.3 Serpent	20
3.2 Mathematical basis	21
3.2.1 Diffusion and precursors equations	21
3.2.2 Thermal-fluids	22
3.3 OECD/NEA MHTGR-350 MW Benchmark	24
3.4 MHTGR-350 Reactor Description	25
Chapter 4 Neutronics	29
4.1 Preliminary studies	29
4.1.1 Homogeneous vs. heterogeneous isotope distribution	29
4.1.2 Problem set-up	30
4.2 Serpent-Moltres comparison	33
4.2.1 Fuel column	33
4.2.2 Full-core	38
4.3 OECD/NEA MHTGR-350 MW Benchmark: Phase I Exercise 1	43
4.3.1 Periodic vs Reflective Boundary Conditions	46
4.4 Conclusions	47
Chapter 5 Thermal-fluids	49
5.1 Preliminary studies	49
5.1.1 Verification of the thermal-fluids model	49
5.1.2 Unit cell problem	49
5.2 Fuel column	53
5.2.1 Flow distribution analysis	55

5.3	Mesh convergence analysis	58
5.4	OECD/NEA MHTGR-350 MW Benchmark: Phase I Exercise 2	59
5.5	OECD/NEA MHTGR-350 MW Benchmark: Phase I Exercise 3	64
5.6	Conclusions	64
Chapter 6	Hydrogen Production	67
6.1	Introduction	67
6.2	Illinois Climate Action Plan	69
6.3	Objectives	70
6.4	Hydrogen production methods	70
6.4.1	Electrolysis	70
6.4.2	Sulfur-Iodine Thermochemical Cycle	72
6.5	Microreactors and Small Modular Reactors	74
6.6	Methodology	74
6.7	Results	76
6.7.1	Transportation	76
6.7.2	Electricity Generation	78
6.8	Conclusions	81
Chapter 7	Conclusions	83
7.1	Contribution	83
7.2	Future Work	83
8.2	Verification of the thermal-fluids model	85
References		87

List of Tables

3.1	MHTGR-350 Characteristics [88].	25
3.2	MHTGR350 fuel element characteristics [88].	27
3.3	TRISO and fuel compact characteristics [88].	27
3.4	LBP compact characteristics [88].	28
4.1	Neutron mean free path in different materials. Values expressed in <i>cm</i>	32
4.2	Energy group structure.	33
4.3	Serpent and Moltres eigenvalues.	36
4.4	Axial flux relative error L_2 -norm for various energy group structures. Values expressed in percentage.	38
4.5	Serpent and Moltres eigenvalues.	39
4.6	Macroscopic regions.	44
4.7	Global parameters.	45
4.8	Global parameters comparison for different types of BCs.	47
5.1	Problem characteristics.	50
5.2	Problem characteristics.	51
5.3	Comparison between In et al. and Moltres/MOOSE results.	53
5.4	Problem characteristics.	53
5.5	Thermal conductivity coefficients.	54
5.6	Mass flow rate [g/s]. Values form [107].	54
5.7	Maximum temperatures.	55
5.8	Mass flow rates [g/s].	57
5.9	Comparison of the maximum temperatures that the different cases yield.	58
5.10	Maximum temperatures.	59
5.11	Problem characteristics.	61
5.12	First bottom core level average temperatures.	61
5.13	First bottom core level average temperatures.	62
6.1	Energy requirements of the different methods.	75
6.2	H_2 necessary to replace a gallon of fuel [96] [20].	76
6.3	H_2 requirement for MTD and UIUC fleets.	76
6.4	CO_2 savings in pounds per gallon of fuel burned [1].	77
6.5	CO_2 yearly savings.	77
6.6	Microreactor designs.	78

List of Figures

1.1	Drawing of a TRISO fuel particle. Image reproduced from [43].	2
3.1	MHTGR reactor layout.	26
3.2	MHTGR-350 fuel assembly layout.	26
4.1	Relative error of the group constants generated with a homogeneous isotope distribution.	30
4.2	Fuel column of the MHTGR-350. xy -plane in the active core region.	31
4.3	Two group axial flux comparison.	32
4.4	Case no LBP at 600K. 3-group axial neutron flux.	34
4.5	Case no LBP at 1200K. 3-group axial neutron flux.	35
4.6	Case LBP at 600K. 3-group axial neutron flux.	35
4.7	Case LBP at 1200K. 3-group axial neutron flux.	35
4.8	No LBP case. L_2 -norm relative error for different number of energy group structures.	36
4.9	LBP case. L_2 -norm relative error for different number of energy group structures.	37
4.10	Computational time and memory requirements for different number of energy group structures. . .	37
4.11	MHTGR-350 full-core models.	39
4.12	Radial power distribution at 600 K.	40
4.13	Radial power distribution at 1200 K.	40
4.14	Axial view of the flux detector locations.	41
4.15	Axial flux at 600 K.	41
4.16	Radial flux at 600 K.	42
4.17	Axial flux at 1200 K.	42
4.18	Radial flux at 1200 K.	42
4.19	1/3-rd of the MHTGR-350 geometry.	44
4.20	Radially averaged axial power distribution.	45
4.21	Axially averaged radial power distribution.	46
5.1	Scaled-down version of the model geometry.	50
5.2	Temperature profiles.	51
5.3	Moltres/MOOSE input parameters.	52
5.4	Temperature profiles.	52
5.5	Outlet plane temperature along the line A-B and line A-C.	55
5.6	Full fuel column model geometry.	58
5.7	Model geometry.	60
5.8	Model geometry.	61
5.9	Model geometry.	63
5.10	Axial temperatures.	63
6.1	Total US GHG emissions by economic sector in 2017. Image reproduced from [36].	67
6.2	The duck curve. Image reproduced from [12].	68
6.3	Energy required by HTE at 3.5 MPa.	72
6.4	Diagram of the Sulfur-Iodine Thermochemical process. Image reproduced from [9].	73

6.5 Energy required by the Sulfur-Iodine Thermochemical Cycle.	74
6.6 Diagram of a reactor coupled to a hydrogen plant.	75
6.7 Fuel consumption data.	76
6.8 H ₂ requirement for MTD and UIUC fleets.	77
6.9 Hydrogen production rate by the different microreactor designs.	78
6.10 Prediction of the electricity generation in the US for 2050. Data from [2].	79
6.11 Prediction of the UIUC's net demand for 2050.	79
6.12 H ₂ production.	80
6.13 Peak reduction by using the produced H ₂	81

Chapter 1

Introduction

1.1 The Prismatic High-Temperature Gas-Cooled Reactor

The history of prismatic High-Temperature Gas-Cooled Reactors (HTGRs) or simply Prismatic Modular Reactors (PMRs) begins in the 1960s with the deployment of the Dragon reactor in the United Kingdom (UK). Its initial objective was to demonstrate the feasibility and launch the technology of the HTGR. The Dragon reactor experiment first operated in July 1965 and reached its full-power operation of 20 MWt in April 1966. The reactor operated for 11 years, demonstrating many components' successful operation and providing information on fuel and material irradiation tests. Simultaneously, interest in the United States (US) led to the 40 MWe HTGR at Peach Bottom. This reactor achieved initial criticality in March 1966 and went into commercial operation in June 1967. Peach Bottom demonstrated the HTGR concept by confirming the core physics calculations, verifying the design analysis methods, and providing a database for further design activities. Most importantly, the plant demonstrated the ability of HTGRs to function in a load-following manner [14]. After the deployment of these two prototype reactors came the first HTGR demonstration plant - the Fort St. Vrain (FSV) Generating Station. Its electric power generation started in December 1976, reaching full-power operation in November 1981. The FSV plant generated 842 MWt to achieve a net output of 330 MWe. This reactor laid the foundation for future prismatic designs. Beginning with FSV, the US core design included ceramic coated Tristructural Isotropic (TRISO) particles embedded within rods placed in large hexagonal-shaped graphite elements [14].

The HTGR's most fundamental characteristic is the unique safety philosophy embodied in its design [51]. The control of radionuclides does not rely on active systems or operator actions. TRISO particles, pictured in Figure 1.1, play a significant role in this task. They consist of various layers acting as containment to limit the radioactive product release. A TRISO particle is a microsphere of about 0.8 mm in diameter. It includes a fuel kernel surrounded by a porous carbon layer (or buffer), followed successively by an inner pyrolytic carbon (IPyC) layer, a silicon carbide (SiC) layer, and an outer pyrolytic carbon (OPyC) layer. The buffer layer allows for limited kernel migration and provides some retention of gas compounds [88]. The IPyC layer protects the kernel from chloride during the SiC decomposition and contributes to fission gas retention [27]. The SiC layer ensures the particle's structural integrity

under constant pressure and helps retain non-gaseous fission products. The OPyC layer contributes to fission gas retention and protects the SiC layer during handling. As an additional advantage, TRISO particles increase the proliferation resistance of HTGRs. They are unattractive and the least desirable route for diversion or theft of weapons-usable materials [50].

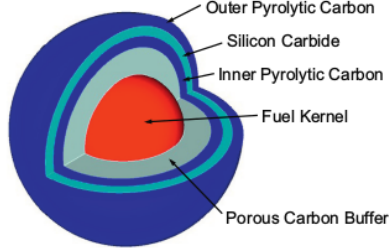


Figure 1.1: Drawing of a TRISO fuel particle. Image reproduced from [43].

Another contributor to the passive safety of the HTGR design is its materials. Combining a graphite core structure, ceramic fuel, and inert helium permits exceedingly high operating temperatures [7]. Graphite has a high heat capacity and maintains its strength at temperatures beyond 2760 °C. As a result, temperature changes in the core occur slowly and without damage to the core structure during transients. The annular core geometry and low core power density also enable passive heat transfer mechanisms to remove the decay heat following postulated accidents [90]. These passive heat transfer mechanisms rely primarily on the natural processes of conduction, thermal radiation, and convection.

A desirable feature of the HTGR is its higher operating temperature. Higher temperatures offer increased cycle efficiencies. The early HTGR designs converted their heat into electricity using the Rankine steam cycle [48]. In such a system, the helium coolant passes through a heat exchanger generating steam to drive a turbine. This arrangement is around 38% efficient [13]. Some of these designs would superheat the steam to increase their efficiency, but this complicates the plant layout [7]. A practical temperature limit is around 300-400 °C. To take advantage of the high core outlet temperature of the HTGR, the Brayton cycle is a better option because the helium coolant can directly drive a gas turbine in a closed cycle. With such configuration, the system can achieve an energy conversion efficiency of around 48% [13]. Additionally, having helium circulating in a closed cycle removes external sources of contamination of the nuclear circuit. This reduces the need for on-line cleanup systems [51].

Higher outlet temperatures and increased cycle efficiencies in HTGRs enable a wide range of process heat applications. Some applications use steam for coal gasification processes, oil refinery processes, and production of synthesis gas, methanol, and hydrogen. Hydrogen can be a decisive response to energy and climate challenges, as it can decarbonize the transport and power sectors [86]. Several hydrogen production processes benefit from high temperatures, such as high-temperature electrolysis or thermochemical water splitting. Utilizing the HTGR as the

energy source of the process eliminates the need to burn fossil fuels to generate the steam those processes require [51].

This thesis focuses primarily on the Modular High-Temperature Gas-Cooled Reactor (MHTGR)-350 [90] [109]. Under the sponsorship of the US Department of Energy (DOE), a team consisting of General Atomics, Combustion Engineering, General Electric, Bechtel National, Stone & Webster Engineering, and Oak Ridge National Laboratory (ORNL) developed the MHTGR [90]. They designed the basic module to deliver superheated steam at 17.3 MPa and 538 °C. Based on both economic and technological considerations, a 350 MWt modular reactor defines the optimal configuration. The team completed in 1986 the preliminary safety information document for the MHTGR and the complete draft pre-application in 1989 [50].

1.2 Motivation

This work's ultimate goal is to support the development of HTGR technology. More specifically, we focus on the development of computational methods for modeling HTGRs with *Moltres* as our primary analysis tool.

The Generation IV Roadmap project identified reactor concepts that could meet the future's energy demands in an efficient, economical, and environmentally safe manner [81]. One of these reactor concepts is the Very High Temperature Gas Cooled Reactor (VHTR). The VHTR is distinct from the HTGR as its coolant outlet temperature reaches higher temperatures. However, the literature often uses these terms interchangeably. In this work, the term HTGR encompasses both terms. The DOE selected this reactor concept for the Next Generation Nuclear Power (NGNP) Project. This project intended to demonstrate emissions-free nuclear-assisted electricity and hydrogen production by 2015.

Although the DOE canceled the NGNP Project, HTGRs may become a reality in the near term. Some microreactor designs embody this type of technology and may be operational before 2030. Additionally, as Section 1.1 has already described, the HTGR technology has several favorable characteristics. To recapitulate the most relevant features, the HTGR relies on passive heat transfer mechanisms, uses TRISO particles as its fuel which inhibits proliferation, achieves high temperatures, and benefits from increased cycle efficiencies. Another beneficial characteristic is that high temperatures enable a wide range of process heat applications, among which we find hydrogen production.

Modeling and prediction of core thermal-hydraulic behavior is necessary for assessing the safety characteristics of a reactor. Determining the temperature inside a reactor, for both normal and transient operation, is of paramount importance as several materials' integrity depends on it. Undesirably high temperatures endanger the TRISO particles' integrity and, consequently, jeopardize a fission product release [118]. Furthermore, the fuel blocks' complex geometry hinders accurate calculations of the fuel temperatures requiring elaborate numerical calculations.

The characteristics of an HTGR are different from those of conventional Light Water Reactors (LWRs). Such differences demand for new reactor analysis tools. These new tools should take into account the following peculiarities of HTGRs [105][11]:

- Hexagonal structure: the shape of the fuel blocks hinders conformity to any orthogonal coordinate system.
- Double heterogeneity: the TRISO particles form the first heterogeneity level, consisting of four layers. The second level arises from the fuel elements, as they encompass the compacts, the coolant, and the moderator.
- Strong temperature dependence: the fuel temperatures have a large effect on the neutron spectrum and the macroscopic cross-sections.
- High thermal inertia: the large graphite structures cause long transients.

Historically, linking a stand-alone neutronics solver to a thermal-hydraulics solver allowed for simulating an entire reactor. The coupling of the programs occurred in a black-box fashion, such that one code's output served as the other's input and vice versa. This coupling technique is commonly known as the operator-splitting technique [102]. In such an approach, each individual physics isolates the action of the governing equations upon the variables. Nonetheless, these physical models describe processes that rely heavily on the solution of one another's. The neutron flux determines the power distribution, and the power distribution strongly influences the temperature field. Due to the HTGR strong temperature feedback, the temperature affects the neutron flux distribution in the core. Because of a time-scale separation between the different phenomena, multiphysics transient simulations coupled via the operator-splitting approach may introduce significant numerical errors [102] [100].

Multi-physics Object-Oriented Simulation Environment (MOOSE) [39] is a computational framework targeted at solving fully coupled systems. All the software built on the MOOSE framework shares a joint code base. These features facilitate relatively easy coupling between separate phenomena and allow for great flexibility, even with a large variance in time scales [93]. Additionally, all programs use Message Passing Interface (MPI) for parallel communication and allow for deployment on massively-parallel cluster-computing platforms.

Moltres [80] is an open source, Finite Element Method (FEM) simulation code built within the MOOSE framework. *Moltres* solves arbitrary-group neutron diffusion, precursor, and temperature governing equations. All these characteristics make *Moltres* suitable for solving the type of physical phenomena described above.

1.3 Objectives

As mentioned earlier, the ultimate goal of this work is to support the development of HTGR technology. The following list of main objectives expands on that goal.

Extend Moltres modeling capabilities to HTGRs. Moltres is a multi-physics solver of Molten Salt Reactors (MSRs). Enhancing Moltres will allow it to model HTGRs as well.

Couple the different physics phenomena present in an HTGR. Moltres's current capabilities allow for solving some of the physics in the HTGR design. Nevertheless, the solver needs to capture the inherent physics in an HTGR and adequately integrate them into the current capabilities.

Develop safety analysis capabilities in Moltres. Steady-state simulations help understand the fundamental behavior of an HTGR and, like transient simulations, assist in reactor design. Transient simulations also assess the reactor response in design basis events.

Understand HTGR contribution to stopping climate change. HTGRs are an attractive technology due to attaining high temperatures. With such high temperatures, the efficiency of hydrogen production increases.

The main objectives are somewhat broad. The following list presents secondary objectives which will lead to the fulfillment of the main objectives:

Predict neutronics. Moltres should have the ability to carry out eigenvalue calculations appropriately. Additionally, Moltres should predict the flux shape and magnitude accurately, during steady-state and transient simulations.

Understand the impact of some simulation parameters. The underlying physics of HTGRs differ from the physics of other reactors. Consequently, the simulation results will be sensitive to different parameters from other reactor type simulations. This work will focus on the energy group structure and its effects on the diffusion calculations. We will also assess how such parameters affect the performance of the simulations.

Calculate power distribution correctly. The value of an accurate neutronics behavior prediction lies in the accurate prediction of the power distribution. The power distribution is the most influential parameter over the thermal-hydraulics as it determines the temperature profile in the reactor.

Predict temperature profile accurately. Undesirably high temperatures endanger the integrity of the TRISO particles. Additionally, the temperature influences the neutronics. Hence, an accurate neutronics calculation will be inaccurate without a correct thermal-hydraulics calculation and vice versa.

Develop a hydrogen production calculation tool. High temperatures enable high-efficiency hydrogen production methods. Most of them have different energy requirements and production rates. We will develop a tool to determine such quantities.

Chapter 2

Literature Review

2.1 Prismatic HTGR Diffusion Solvers

Nowadays, several codes solve the neutronics of prismatic HTGRs. Most of these codes rely on one of the following methods: stochastic transport (Monte Carlo), deterministic transport, or deterministic diffusion. We focus our interest on the last method.

The history of deterministic diffusion solvers begins in the late 1950s with the Finite Difference Method (FDM) application to the analysis of LWRs. In FDM, mesh spacings are usually of the order of the diffusion length. While solving large multi-dimensional problems, this feature causes the mesh points to reach intractable numbers [77]. The computational expense of these calculations motivated the generation of more computationally efficient techniques [70]. Although substantial overlaps exist, the most common techniques fall into two broad categories: nodal methods and FEM.

FLARE [26] is a three-dimensional Boiling Water Reactor (BWR) simulator, and it is representative of the first generation of nodal methods. Such an approach used adjusted parameters to match actual operating data or the results of more accurate calculations. Most of these methods were implementations of the so-called "1.5 group theory" [42]. The second generation of nodal methods derived spatial coupling relationships by applying the transverse integration procedure (TIP). Such a procedure obtains equivalent one-dimensional equations by integrating the multi-dimensional diffusion equation over directions transverse to each coordinate axis [70]. This approach proved to be highly efficient and accurate in Cartesian geometries.

In 1981, a formulation based on the Nodal Expansion Method (NEM) first demonstrated the feasibility of nodal methods in hexagonal geometries [33]. However, this method would introduce non-physical singular terms that required the utilization of discontinuous polynomials. This drawback motivated the development of more effective formulations. HEXNOD, introduced in 1988 by Wagner [129], is an example of such formulations. This algorithm uses the TIP and, in contrast to the NEM, solves the resulting differential equation analytically. Wagner's article demonstrated the method's good accuracy by comparing to FDM and Monte Carlo calculations for a few benchmark problems.

Another example of more effective methods is HEXPEDITE [38]. HEXPEDITE uses the TIP formulation to derive a pseudo-one-dimensional equation. The resulting differential equation is solved analytically. The difference from HEXNOD is that HEXPEDITE uses a simpler and more efficient coupling scheme. Different works [38][37] on the HEXPEDITE methodology tested the approach against the NEM and the FDM. These studies established HEXPEDITE's superiority in terms of accuracy and runtime. HEXPEDITE's use prevailed in the analysis of HTGRs until recently. In 2010, Idaho National Laboratory (INL) conducted a study [98] in which they compared HEXPEDITE's results against several diffusion codes, as well as the Monte Carlo codes MCNP5 [23] and Serpent [75].

DIF3D [69] and PARCS [31] are other examples of nodal diffusion codes whose use has prevailed until the present. DIF3D has several solution options such as the diffusion FDM, diffusion NEM based on TIP, and the VARIANT nodal transport method. PARCS has several solution options as well, such as a diffusion FDM, diffusion NEM based on TIP, P_N transport methods, and the multigroup transport simplified P_3 with FDM and NEM discretizations.

Nodal methods solve relatively coarse meshes for approximate solutions. This characteristic makes the process efficient. On the other hand, the method does not provide detailed point-wise accurate solutions [64]. Additionally, the derivation of nodal methods happens in a specific coordinate system for a particular node shape. The application to complex problems is not flexible as different geometries require the integration over other coordinate systems. This lack of flexibility limits the applications of nodal methods to regular geometries only.

The FEM is a well-established method in applied mathematics and engineering. FEM is a numerical technique for finding approximate solutions to partial differential equations by deriving their weak or variational form. Most applications make FEM preferable due to its flexibility in the treatment of curved or irregular geometries. Also, the use of high order elements attains higher rates of convergence [18]. The first engineering application of FEM was in the field of structural engineering dating back to 1956. In successive years, FEM became the most extensively used technique in almost every branch of engineering. FEMs have several advantages over the nodal methods. It provides flexibility in the geometry definition, a firm mathematical basis, ease in extension to the multi-group application, and high computational efficiency [72].

In 1973, Kang et al. [64] described the first application of FEM to the neutron diffusion theory. The fundamental motivation for this development was the impractical application of the FDM to three-dimensional problems. In this early work, the author compared different FEM approaches to the FDM in one-dimensional and two-dimensional problems. The studies showed a higher order of convergence achieved by the FEM.

Throughout the last four decades, many codes utilized the FEM to solve the diffusion equation. Some of the most recent software for diffusion simulations are CRONOS2 [68], CAPP [73], and Rattlesnake [131]. The list of FEM diffusion solvers is more extensive, but we focus on the best-documented software in the open literature.

Commissariat a l'Energie Atomique (CEA) developed CRONOS2 [68] as part of the SAPHYR system. It solves

steady-state and transient multi-group calculations, taking into account thermal-fluids feedback effects. CRONOS2 solves either the diffusion equation or the transport equation using the S_N method and an FDM or a FEM discretization. In 2008, Damian et al. [25] conducted a study aimed at understanding the physical aspects of the annular core and the passive safety features of a standard block type HTGR. For such a study, the authors developed the code suit NEPTHIS/CAST3M which relied on CRONOS2.

In 2008, the Korea Atomic Energy Research Institute (KAERI) published an article [72] that presented CAPP. Its purposes are to conduct steady-state core physics analysis, core depletion analysis, and core transient analysis. The article validated the code with two benchmark problems: the IAEA PWR benchmark problem, and Phase I Exercise 1 of the OECD/NEA PBMR-400 Benchmark [103]. The calculations of both problems changed the number of finite elements and the orders of shape functions.

In 2011, Lee et al. published an article [73] in which they extended the functionalities of CAPP to prismatic HTGRs. To take into account the thermal feedback, the authors developed a simplified thermal-fluids analysis tool. To validate their model, the authors solved a two-dimensional model of the PMR-200 at the beginning of the equilibrium cycle. The PMR-200 is a pre-conceptual reactor designed by KAERI. Their validation compared the results against HELIOS[112], concluding with a strong accuracy. Moreover, the authors implemented a depletion solver based on the one-group flux determined by the diffusion solver. The authors validated the depletion solver by calculating the multiplication factor as a burnup function of a single fuel block of the PMR-200. They compared the results against HELIOS. The maximum error was less than 200 pcm.

Tak et al. [119] developed a coupling between CAPP and GAMMA+ [78]. GAMMA+ is a system code for thermal-fluids analysis and system transients. In such a study, they studied the steady-state performance of the PMR-200. The authors conducted several studies, such as a core depletion calculation with and without a critical control rod position search and the analysis of the bypass flow effects on the coupled calculations. Their results revealed that neglecting the bypass flow decreases the active core temperatures; consequently, the multiplication factor increases by approximately 300 pcm.

A recent article by Yuk et al. [134] added to CAPP the capability to conduct transient analyses. This capability solves the time-dependent neutron diffusion equation with the FEM. The primary motivation behind this feature was to perform reactivity insertion accidents. Additionally, the article introduced a new method to resolve the control rod cusping effect [61]. The new method integrates over partially rodded computation nodes, and the article referred to it as iPRN. To test its accuracy, the authors conducted two exercises with several techniques that reduce the rod cusping effect. The authors used the mesh reconstruction method to obtain the reference results, as such a method eliminates the rod cusping effect by updating the mesh at every time step. The iPRN technique showed higher accuracy than the other methods. To test the new transient capabilities, they analyzed two control

rod ejection scenarios and compared the results to those of the CAPP/GAMMA+ coupled code. Both showed similar results.

RattleSnake [131] is the MOOSE [39] based application for simulating the transport equation. INL had initially developed Pronghorn [114] to model Pebble Bed Modular Reactors (PBMRs). The MOOSE neutronics kernel library Yak incorporated the neutron diffusion models initially in Pronghorn. Currently, RattleSnake is the primary tool for solving the linearized Boltzmann neutron transport equation within MOOSE and relies heavily on Yak's use. Various solvers are available under RattleSnake, including low-order multigroup diffusion, spherical harmonics transport, and discrete ordinates transport, all solved with the FEM.

In 2012, INL published a study [59] that coupled Pronghorn and RELAP-7 [3]. Pronghorn solved the coupled equations defining the neutron diffusion, fluid flow, and heat transfer in a three-dimensional model. RELAP-7 is a MOOSE-based system code and solves the one-dimensional continuity, momentum, and energy equations for a compressible fluid. It was responsible for simulating the plant system layout, including the hot and cold ducts, the helium circulator, and the steam generator. To test the coupling, INL's team carried out the OECD/NEA MHTGR-350 Benchmark [89]. The original benchmark provides a set of 26 neutron energy group and temperature dependent cross sections. To simplify the debugging, the authors collapsed the 26 groups into two groups. Although using two groups reduces the accuracy of the model, the lower number of groups decreases the calculation time by at least a factor of ten. In this study, a two-dimensional cylindrical model replaced the three-dimensional geometry defined by the benchmark. The integrated system testing included two stages: (1) both stand-alone codes underwent several convergence studies, and (2) the integrated system solved the steady-state problem in an integrated manner. The authors concluded that the coupling between Pronghorn and RELAP-7 was successful.

In 2013, INL conducted the OECD/NEA MHTGR-350 Benchmark [114] without further simplifications. The INL team solved Phase I Exercise 1 using INSTANT-P1 [130], Pronghorn, and RattleSnake. INSTANT-P1 is a transport solver that relies on the spherical harmonics discretization of angles. The results for Pronghorn and RattleSnake were identical. By modifying the cross-sections, INSTANT-P1 returned the diffusion solution. Its results were within 30 pcm from Pronghorn and RattleSnake results. All presented results exhibited good agreement with the benchmark results.

2.1.1 Energy group structure analysis

The longer neutron mean free path in HTGRs compared to LWR increases the spectral interactions between elements. For this reason, HTGR analyses require more energy groups than conventional LWR analyses. Argonne National Laboratory (ANL) directed a study [71] to compare the accuracy of nodal diffusion calculations employing different energy group structures to generate the homogenized cross-sections. The cross-section homogenization used the

code DRAGON and the diffusion calculations utilized the code DIF3D. For the study, the ANL team implemented a one-dimensional fuel-reflector model in which they used 4, 7, 8, 14, and 23 energy groups. They also used alternative energy group structures for the same number of groups. For simplicity, the authors used the homogenized fuel compact model and generated all the cross-sections at 300 K. One of their conclusions was that the number of energy groups should be more than 4, and more than 6 would be sufficient for uranium fueled HTGRs. Another finding was that the accuracy of the diffusion calculation is sensitive to the energy group boundaries.

Han's MS thesis [44] focused on selecting energy groups for the reactor analysis of the PBMR. The author used COMBINE6 [41] for cross-section generation and the Penn State nodal diffusion code NEM [8] for the reactor analysis. The author compared the results against MCNP5 reference results. To simplify the setup, the model used uniformly distributed isotopes in the fuel. The study performed the calculations at 300 and 1000 K. To arrive at an optimal group structure, the author compared many combinations of group structures using a trial and error strategy. One conclusion of this work agrees with the previous bibliography [24] [32] in that the energy spectrum is critical to yield an accurate description of a nuclear reactor using a few groups.

ANL's study helps set up proper nodal diffusion calculations for an HTGR. Although we can extrapolate those conclusions to FEM diffusion solvers, such a study might be valuable. ANL's team conducted the study at 300 K - not in the operational range of any HTGRs. On the contrary, Han's thesis included an analysis at 1000 K, and his results showed that the temperature changes have a non-negligible impact. Additionally, ANL's study used the simplified model of the homogenized fuel compact. Han highlighted that homogenized fuel models of the PBMR underestimate criticality calculations. In 2015, INL presented their results [113] for an International Atomic Energy Agency (IAEA) Coordinated Research Project (CRP) [123] and showed that the homogenization of the compact material notably underestimates the multiplication factor. On the other hand, the open literature has not investigated the impact of such simplification over the homogenized cross-sections.

2.2 Prismatic HTGR Thermal-fluids

Thermal-fluids calculations enable the correct design of HTGRs. Predicting the maximum fuel temperature at a steady-state is of paramount importance to succeed in such a task. We emphasize this statement in the case that hydrogen production is desirable. Efficient hydrogen production requires higher coolant temperatures, leading to high fuel and reactor vessel temperatures.

The complex geometry of the hexagonal fuel assembly requires elaborate numerical calculations for obtaining accurate evaluations. Thermal-fluids studies for early HTGRs consisted mainly of support calculations for Nuclear Regulatory Commission (NRC) safety analysis reports. The analyses employed sets of independent codes that relied

on simplistic approximations. Simplified models help understand some fundamental aspects of prismatic HTGRs and have the advantage of reducing the computational expense of the calculations.

General Atomics [108] developed the first set of simplistic codes. The following list introduces and summarizes some of these and their features:

- FLAC: It determines the coolant flow distribution in the coolant channels and gaps. It solves the one-dimensional momentum equation for incompressible flow and the continuity equations for mass and energy.
- POKE: It determines the coolant mass flow, coolant temperature, and fuel temperature distribution. It solves the steady-state mass and momentum conservation equations for parallel channels.
- DEMISE: It determines the steady-state three-dimensional temperature distribution in a standard element. It solves the temperature in a network model.
- TAC2D: It is a general-purpose thermal analysis code. It solves the two-dimensional heat conduction equation.

Several studies have used these codes. For example, INL conducted in 2003 a design study [81] in support of the NGNP project. Such a study aimed to investigate options for the NGNP that increase the coolant temperature with the lowest possible inlet temperature and the highest overall core power. The authors conducted several parametric studies whose reference reactor was the GT-MHR [5]. Using POKE, they evaluated two major design modifications: reducing the bypass flow and better controlling the inlet coolant flow distribution. Reducing the bypass flow fraction from 20 to 10% reduces the peak fuel temperatures by about 50°C. Controlling the inlet flow distribution has a stronger effect. Other studies focused on the dimensions of the reactor and their impact on the maximum fuel temperature. Using POKE and TAC2D, the authors investigated taller and higher power reactor cores. The investigation included a 10-block-high 600 MWt, a 12-block-high 720 MWt, and 14-block-high 840 MWt.

Among the simplified approaches, we differentiate the flow network, equivalent cylindrical model, and unit cell model. Using the network analysis tool RELAP5-3D/ATHENA [57], Reza et al. [104] conducted a thermal-fluids study of the GT-MHR. Reza et al. increased the reactor outlet temperature to enable hydrogen production. Additionally, they evaluated alternative coolant inflow paths in an attempt to reduce the reactor vessel temperatures. After finding an optimal configuration, they evaluated the fuel and the reactor vessel's maximum temperatures during the low pressure conduction cool-down (LPCC) and the high pressure conduction cool-down (HPCC) events.

An example of codes using the equivalent cylindrical approach is GAMMA [92]. Its main objective is simulating the air ingress event following a LOCA. Following the depressurization of helium in the core, there exists the potential for air to enter the core through the break and oxidize the in-core graphite structure. The oxidation of graphite leads to exothermic chemical reactions and, thus, it is a significant concern. GAMMA solves heat conduction, fluid flow,

chemical reactions, and multi-component molecular diffusion. The code couples the solid and gas equations using the porous media model. Together with the multi-dimensional analysis feature, GAMMA has a one-dimensional analysis capability for modeling a flow network.

Takada et al. [121] carried out another study using the flow network and the equivalent cylindrical model. Focusing on the High Temperature Test Reactor (HTTR), they developed a thermal-fluids design code. This used the flow network analysis code FLOWNET [83] for calculating the coolant flow and temperature distributions. TEMDIM [83] solved the fuel temperatures using the equivalent cylindrical model. Finally, the authors validated the calculation scheme by comparing its results with the experimental data from the HTTR.

Nakano et al. [87] studied different fuel assembly configurations using several simplistic approximations. For determining the fuel temperature, they used TAC2D. A previous study calculated the flow distribution using FLOWNET. The fuel temperature calculation used the equivalent cylindrical model for a hot channel unit cell. However, the asymmetry of the unit cell configuration makes the temperature distribution asymmetric in the graphite block. The equivalent cylindrical model fails to capture this behavior.

In 2006, In et al. [53] conducted a more detailed analysis using a three-dimensional model of the unit cell in the hot-spot of an HTGR. The objective of the study was to predict the maximum fuel temperature at steady-state. The analysis focused on the GT-MHR 600 at the end of the equilibrium cycle. The CFD code CFX 10 [54] calculated the three-dimensional temperature profile. The results showed that the maximum fuel temperature surpassed the design limits, so the authors proposed a countermeasure accordingly.

Such simplified approaches are helpful to understand essential aspects of prismatic HTGRs but they may affect the temperature distribution. More detailed thermal-fluids evaluations were rare in the open literature until the last 15 years.

Cioni et al. [22] presented an article in 2005 in which they conducted three-dimensional simulations of fuel assemblies of an HTGR. The study's objective was to investigate an emergency situation due to the blocking of cooling channels in the core. They used the computational fluid dynamics (CFD) code Trio_U [10] to carry out the analysis. The numerical scheme solved the three-dimensional conduction equation in the solid coupled to the coolant's one-dimensional thermal-fluid equations. A preliminary study analyzed the consequences of two different blocking in a portion of a fuel assembly. A central blockage exhibited a stronger influence over the assembly's maximum temperatures compared to a peripheral blockage. Last, they investigated two configurations. First, six fuel elements surrounded the fuel element with the blockage. Second, five fuel elements and one reflector element surrounded the fuel element with the blockage. The blockage increased the temperature on the blocked fuel assembly only and it did not affect the surrounding elements due to the bypass flow. The results also show that the fuel temperature surpassed the design limits and that the reactor operators should counteract these effects with

active systems.

Simoneau et al. [110] analyzed the transient behavior of an HTGR during the depressurized conduction cooldown (DCC) and HPCC event. The CFD code STAR-CD [79] performed the calculations. It solved conductive, convective, and radiation heat transfer in a 30° section of the core and reactor vessel. It used the porous media model to accommodate the different spatial scales. The model did not resolve the boundary layer, and the use of coefficients prescribed the solid-fluid heat transfer and pressure drop across the core. The authors validated their model against explicit calculations using a single fuel block. One of their results showed that the maximum temperature in the HPCC event is lower than in the DCC event. However, the extra convective heat transfer caused a thermal stratification in the surrounding air, causing higher temperatures in the upper reactor structures.

In 2008, an article by Tak et al. [118] conducted a three-dimensional CFD analysis on a typical prismatic HTGR fuel column. The commercial code CFX 11 [56] performed the calculations. The fuel column under study was from the PMR-600, a pre-conceptual reactor designed by KAERI whose reference design is the GT-MHR. The study considered a one-twelfth section of the fuel due to its symmetry. The model determined the coolant distribution using the one-dimensional thermal-fluid equations. Such coolant distribution served as input to the CFD code. The friction in the channels is dependent on the viscosity, which is highly dependent on the temperature. Therefore, obtaining the mass flow rates from a separate solver may introduce errors [107]. As mentioned earlier, the unit cell model may introduce errors in the maximum temperature prediction. To assess the accuracy of the unit cell model, the authors compared the CFD results against the unit cell model results. The unit cell model does not consider the bypass flow between assemblies or the radial power distribution within the fuel assembly. Tak et al. conducted a parametric study that analyzed the bypass gap size's impact on the maximum fuel temperature. By increasing the bypass gap, the maximum fuel temperature grows. The results of this study indicate that the accuracy of the unit cell worsens for larger gaps. Another study imposed different radial peaking factors for the different fuel channels. Such a study showed the effects of considering a non-flat radial power distribution. The authors considered a radial power distribution that did not strongly impact on the maximum fuel temperature.

Another article [107] carried out CFD calculations of a typical prismatic HTGR with the commercial code FLUENT [55]. Their modeled a one-twelfth section of the fuel column of the GT-MHR. The authors conducted parametric studies changing several factors, such as bypass gap-width, turbulence model, axial heat generation profile, and geometry changes due to irradiation. Their most relevant results show that the bypass flow causes a large lateral temperature gradient in the block. Large temperature gradients cause excessive thermal stresses, which raise potential structural issues. The authors compared the results from different turbulence models: $k \sim \varepsilon$ and $k \sim \omega$. The $k \sim \omega$ model predicted bulk temperatures that are considerably lower than those from the $k \sim \varepsilon$ model. The maximum temperature difference was 49°C. The overall mass flow rate was about 10% greater for the

$k \sim \omega$ model. The study suggested that these turbulence models need more verification against prismatic HTGR experiments. Another study analyzed the effect of considering different peak radial factors. This consideration introduced variations of the maximum fuel temperature of up to 160 °C. Their last study focused on the effects of the graphite dimensional changes on the temperature profile. The shrunken column showed considerably lower temperatures in the fuel.

Despite the recent developments in CFD tools, a detailed full-core analysis for a prismatic HTGR still requires a tremendous computational expense. This requirement is mostly due to the three-dimensional CFD simulation of the coolant flow. Travis et al. [122] developed a method to compute full-core thermal-fluids analyses of HTGRs. The article presented a simplified method that reduces the computational time and memory requirements while maintaining accurate results. The method solves the three-dimensional heat conduction in the solid and the one-dimensional thermal-fluid equations in the channels. The fluid one-dimensional approximation avoids finer meshes near the walls as well as turbulence conservation equations [120]. The method's validation analyzed a fuel column and compared the results to those of a three-dimensional CFD simulation. The CFD simulation used the commercial software STAR-CCM+ [19]. The new computational scheme reduced the computation time to 2.5% of the CFD simulation time. The new method provided good predictions of the temperature distribution and the axial variation of the helium bulk temperature. However, it failed to resolve the velocity and temperature distribution within the boundary layer properly. Overall, the method showed good accuracy and less than a 2% difference to the CFD simulation.

Tak et al. [116] [120] developed CORONA, which uses a practical method for the whole core analysis. CORONA intends to combine the accuracy from CFD tools and the light computational expense of system analysis codes. The method solves the three-dimensional heat conduction equation in the solid and the one-dimensional thermal-fluid equations in the fluid. To enhance practicability, the code adopts a basic unit cell concept, which eliminates an elaborate grid generation process. The basic unit cell concept is an extension of the traditional unit cell method, which uses a single triangular unit cell. This method considers various shapes of unit cells as well as the heat transfer between them. The method provides a way for fast generating computational grids for modeling the solid regions. To validate CORONA, the authors compared its results against CFX and experimental results. The validation results showed that CORONA provided reasonably accurate results.

CFD techniques allow the detailed temperature profile over local models to be computed. The fine mesh requirement imposes high computational costs for a whole-core CFD analysis, restricting such methods. However, a whole-core thermal analysis has many advantages over local models. In general, the problem set up includes more accurate boundary conditions. Without whole-core modeling, the local models' mass flow distributions are average values of the core flow rate instead of their exact value [49]. This simplification leads to under-predicted

fuel temperatures for the assemblies with a lower flow rate than the average. Additionally, a coupled analysis with a reactor physics code requires a full-core model [116].

2.3 Prismatic HTGR Multi-physics

Historically, stand-alone simulations have solved the neutronics and thermal-fluids of HTGRs. Nonetheless, these physical aspects describe processes that rely heavily on one another. Hence, a coupled analysis is necessary to consider the interaction between the neutronics and thermal-fluids behavior [119].

In 2008, Damian et al. [25] conducted a study aimed to understand the physical aspects of the annular core and the passive safety features of a prismatic HTGR. They performed analyses on various geometrical scales, including: unit cell and fuel columns located at the core hot-spot and two-dimensional and three-dimensional core configurations, including the coupling between neutronics and thermal-fluids. The first part of the assessment concerns thermal calculations on steady-state core configurations. Such a study used CAST3M [115] to solve the three-dimensional heat conduction in the solid coupled with the one-dimensional thermal-fluid equations in the coolant. The second part of the assessment used the transport code APOLLO2 [106] on a two-dimensional core configuration to minimize the radial power peaking factor. The analyses included the variation of several parameters, such as fuel enrichment, fuel loading, and the fuel management scheme. The fuel enrichment variation had the most substantial impact. The last part of the study analyzed a three-dimensional core model using the coupled codes NEPTHIS [17] and CAST3M/Arcturus. NEPTHIS and CAST3M/Arcturus calculate the neutronics and the thermal-fluids, respectively. NEPHTIS uses a transport-diffusion calculation scheme that relies on APOLLO2 and the diffusion code CRONOS2. The CAST3M/Arcturus model uses a two-level approach. On the first level, the porous media model solves the homogenized system and the coolant. On the second level, CAST3M solves the thermal-fluids on the homogenized geometry. The authors conducted several parametric studies and assessed their impact on the power distribution. The studies included the variation of the helium bypass fraction, average power density, core geometry, reflector materials, and fuel loading strategy. One of their results exhibited that with the reduction of the bypass fraction, the average reflector temperature rises. Another result showed that using magnesium oxide as the reflector material yields lower temperatures for normal operation and transients.

In 2011, Lee et al. published an article [73] in which they extended the functionalities of CAPP to prismatic HTGRs. To take into account the thermal feedback, the authors integrated into CAPP a simplified thermal-fluids tool. This tool divides a fuel column into six triangular prisms. Each of them hosts a representative coolant channel. The code calculates the axial coolant temperature distribution solving the energy equation. After calculating the coolant temperature, a two-dimensional conduction model solves the moderator and fuel compact temperatures.

Through a TRISO particle conduction model, the model obtains the fuel temperature. Finally, a three-dimensional conduction model based on the FDM allows for solving the reflector temperature. To validate this model, the authors solved a two-dimensional model of the PMR-200 at the beginning of the equilibrium cycle. They compared the results against HELIOS reference results. The results showed good accuracy.

Tak et al. [117] developed a neutronics/thermal-fluids coupled code using DeCART [62] and CORONA. DeCART is a whole-core neutron transport code, and it was responsible for calculating the power distribution and the fast neutron fluence. CORONA calculated the temperature distribution. To validate the code, the authors conducted the OECD/NEA MHTGR-350 benchmark. The exercise's main objective was to validate the code and identify technical challenges for future development. The authors presented an interesting analysis in which they compared the coupled simulation results and the stand-alone simulations. The difference in the multiplication factor was as high as 2597 pcm. The axial offset and maximum fuel temperature exhibited significant differences as well. Such a result highlights the importance of the integration of both neutronics and thermal-fluid solvers.

Another article [119] introduced a coupling between CAPP and GAMMA+. GAMMA+'s primary motivation was to analyze the air ingress accident and thermo-fluid transients in HTGRs. It uses the one-dimensional form of the mass, momentum, energy, and species conservation equations to solve the fluid's flow and temperature distribution. For solids, it uses three different models: (1) heat conduction model of a TRISO particle, (2) implicit coupling to consider the heat exchange between a fuel compact and TRISO particle, and (3) multi-dimensional heat conduction model of the hexagonal fuel and reflector blocks. In such a study, the authors applied the coupled code to study the steady-state performance of the PMR-200. They analyzed the bypass flow effects on the coupled calculations. Some of their most relevant results showed that the maximum fuel temperature reaches a peak near the middle of the equilibrium cycle. Another result revealed that neglecting the bypass flow decreases the active core temperatures and increases the reflector temperatures. Consequently, the multiplication factor increased by approximately 300 pcm. On the other hand, the power density changes were not appreciable.

A recent article by Yuk et al. [134] added the capability to conduct transient analyses to CAPP. To take into account the thermal feedback, the authors developed a simplified thermal-fluids analysis tool. The tool divides a fuel column into six triangular prisms. Each of them hosts a representative coolant channel. After calculating the coolant temperature, a two-dimensional conduction model solves the moderator and fuel compact temperatures. CAPP code uses predetermined tables of thermal conductivity for each material. For a given fast neutron fluence and temperature, it obtains the thermal conductivity by interpolation. To test the new transient capabilities, they analyzed two control rod ejection scenarios. They compared the results to those from the coupled CAPP/GAMMA+ code. Both methods showed similar results.

The prismatic HTGR tools available have lagged behind state of the art compared to LWRs. This delay drives the

development of more accurate and efficient tools to analyze the reactor behavior for design and safety evaluations. In addition to the development of new methods, it is essential to define appropriate benchmarks to compare various tools' capabilities. In 2012, the Organisation for Economic Co-operation and Development (OECD)/Nuclear Energy Agency (NEA) defined a benchmark for the MHTGR-350 MW reactor [88]. The purpose of this benchmarking exercise is to compare various coupled reactor physics and thermal-fluid analysis methods. The MHTGR design serves as a basis for this benchmark. The scope of the benchmark is twofold: (1) to establish a well-defined problem, based on a common given data set, to compare methods and tools in core simulation and thermal-fluid analysis, and (2) to test the depletion capabilities of various lattice physics codes available for prismatic HTGRs. The OECD/NEA MHTGR-350 MW benchmark subdivides the coupled system calculation into three phases. Phase I corresponds to the stand-alone neutronics and thermal-fluids modeling, as well as the coupled neutronics/thermal-fluids steady-state modeling. Phase II consists of transient cases. Phase III focuses on lattice depletion calculations.

Sensitivity analysis and uncertainty analysis methods can assess the predictive capabilities of coupled neutronics/thermal-fluids simulations. In 2013, the IAEA launched a CRP [123] on the HTGR Uncertainty Analysis in Modeling. The CRP objective was to determine the uncertainty in HTGR calculations at all stages of coupled reactor physics/thermal-fluids and depletion calculations. This CRP is a natural continuation of the previous IAEA and OECD/NEA international activities [52][103] on Verification and Validation of available HTGR simulations capabilities. The technical approach is to establish and utilize a benchmark for uncertainty analysis. The benchmark defines a series of well-defined problems with complete sets of input specifications and reference experimental data. The CRP adopted the MHTGR-350 as the reference design and the GT-MHR as a second reference design. The design specification uses the OECD/NEA MHTGR-350 MW benchmark [88] code design specifications. The CRP subdivides the coupled system calculation into three phases. Phase I corresponds to the stand-alone neutronics and thermal-fluids modeling. Phase II consists of design calculations, coupled with steady-state neutronics/thermal-fluids calculations with and without a depletion calculation. Phase III focuses on safety calculations.

Chapter 3

Methodology

3.1 Computational tools

3.1.1 MOOSE

MOOSE[39] is a computational framework that supports engineering analysis applications. In a nuclear reactor, several partial differential equations describe the physical behavior. These equations are typically nonlinear, and they are often strongly coupled to each other. MOOSE targets such systems and solves them in a fully coupled manner.

MOOSE is an open-source code under a Lesser GNU Public License (LGPL). The code itself relies on LibMesh [65], an LGPL finite element library, and PetSc, a Berkeley Software Distribution (BSD)-licensed toolkit for solving nonlinear equations [6]. MOOSE applications define weak forms of the governing equations and modularize the physics expressions into "Kernels." Kernels are C++ classes containing methods for computing the residual and Jacobian contributions of individual pieces of the governing equations. MOOSE and LibMesh translate them into residual and Jacobian functions. These functions become inputs into PetSc solution routines.

MOOSE utilizes the mathematical structure present in Jacobian-Free Newton-Krylov (JFNK) methods [66]. JFNK methods are synergistic combinations of Newton-type methods for superlinearly convergence of nonlinear equations and Krylov subspace methods for solving the Newton correction equations. The Jacobian-vector product links the two methods. JFNK methods compute such products approximately without forming and storing the elements of the true Jacobian. The ability to perform a Newton iteration without forming the Jacobian gives JFNK methods potential for application throughout problems governed by nonlinear partial differential equations.

All the software built on the MOOSE framework shares a joint base code. The applications, by default, utilize monolithic and implicit methods. This feature facilitates relatively easy coupling between different phenomena and allows for great flexibility, even with a great variance in time scales [93]. Additionally, all codes use MPI for parallel communication and allow deployment on massively-parallel cluster-computing platforms.

3.1.2 Moltres

Moltres [80] is a MOOSE-based application initially designed for modeling fluid-fuelled MSRs. This simulation tool is open source and operates with an LGPL. It uses *git* for version control, emphasizing its openness and promoting quality through peer review.

Moltres solves arbitrary-group neutron diffusion, precursors, and temperature governing equations. It can solve the equations in a fully-coupled way or solve each system independently, allowing for great flexibility and making it applicable to a wide range of nuclear engineering problems.

3.1.3 Serpent

The Serpent Monte Carlo code [74] [76] is a three-dimensional continuous-energy neutron transport code developed by the VTT Technical Research Centre of Finland, and it has been in public distribution since 2009. Monte Carlo neutron transport codes have several reactor physics applications related to criticality safety analyses, radiation shielding problems, detector modeling, and validation of deterministic transport codes. The Monte Carlo method's main advantage is its capability to model geometry and interaction physics without significant approximations. The main disadvantage is that simulating complex systems is computing-intensive, restricting applications to some extent.

Serpent serves two primary purposes: (1) reactor modeling, and (2) group constant generation. In reactor modeling, the Monte Carlo simulation itself represents the solution to the full-scale problem. In group constant generation, the transport simulation produces input parameters for a deterministic code. Based on a few groups, deterministic codes allow for carrying out coupled full-core analyses.

In this work, Serpent produces group constants that serve as an input for *Moltres* and solves the heterogeneous system. This last step provides the reference solutions for the validation of the *Moltres* calculation scheme. We used Serpent 2.1.31 and the cross-section library JEFF3.1.2 for the calculations. The reason for using Serpent to generate cross-sections is due to its ability to run explicit simulations of randomly located TRISO particles. Applying a simple volume homogenization proves inaccurate due to the resonant self-shielding effect of the kernel and coated layers. Although the particles' explicit modeling is time-consuming, costly, and impractical for most applications, it is necessary.

3.2 Mathematical basis

3.2.1 Diffusion and precursors equations

Equations 3.1 and 3.2 describe the time dependent behavior of the neutronics.

$$\frac{1}{v_g} \frac{\partial}{\partial t} \phi_g = \nabla \cdot D_g \nabla \phi_g - \Sigma_g^r \phi_g + \sum_{g' \neq g}^G \Sigma_{g' \rightarrow g}^s \phi_{g'} + \chi_g^p \sum_{g'=1}^G (1-\beta) v \Sigma_{g'}^f \phi_{g'} + \chi_g^d \sum_i^I \lambda_i C_i \quad (3.1)$$

$$\frac{\partial}{\partial t} C_i = \sum_{g'=1}^G \beta_i v \Sigma_{g'}^f \phi_{g'} - \lambda_i C_i \quad (3.2)$$

where

v_g = group g neutron speed

ϕ_g = group g neutron flux

t = time

D_g = group g diffusion coefficient

Σ_g^r = group g macroscopic removal cross-section

$\Sigma_{g' \rightarrow g}^s$ = group g' to group g macroscopic scattering cross-section

χ_g^p = group g prompt fission spectrum

G = number of discrete energy groups

v = number of neutrons produced per fission

Σ_g^f = group g macroscopic fission cross-section

χ_g^d = group g delayed fission spectrum

I = number of delayed neutron precursor groups

β = delayed neutron fraction

λ_i = average decay constant of delayed neutron precursors in precursor group i

C_i = concentration of delayed neutron precursors in precursor group i .

(3.3)

We apply the vacuum boundary condition to the diffusion equation. The vacuum boundary condition states that no neutrons penetrate the boundary in the inward direction. In other words, the incoming current density

$(J^-(r_s, t))$ is equal to zero, equation 3.4 [32].

$$J^-(r_s, t) = \frac{1}{4}\phi(r_s, t) + \frac{D}{2}\hat{n}_s \cdot \nabla\phi(r_s, t) = 0 \quad (3.4)$$

3.2.2 Thermal-fluids

The governing equation for the temperature of the solids is the three-dimensional heat conduction equation [84].

Equations 3.5 to 3.7 allow for solving the temperature in the fuel, moderator, and reflector.

$$\rho_i c_{p,i} \frac{\partial}{\partial t} T_i = k_i \nabla^2 T_i + Q_i \quad (3.5)$$

$$Q_f = \sum_{g=1}^G \epsilon_g^f \Sigma_g^f \phi_g \quad (3.6)$$

$$Q_m = Q_r = 0 \quad (3.7)$$

where

$i = f$ (fuel), m (moderator), r (reflector)

ρ_i = material i density

$c_{p,i}$ = material i heat capacity

k_i = material i thermal conductivity

T_i = material i temperature

Q_i = material i volumetric heat source

ϵ_g^f = energy released per fission

Σ_g^f = group g macroscopic fission cross-section

ϕ_g = group g neutron flux.

The governing equation of the coolant is the one-dimensional form of the continuity, momentum, and energy conservation equations, equations 3.8 to 3.12 [132][116]. We determine the friction factor f using equation 3.13 [21]. We calculate the heat transfer coefficient h using the well-known Dittus-Boelter correlation 3.14.

$$\frac{\partial}{\partial t} \rho_c + \nabla \cdot (\rho_c u) = 0 \quad (3.8)$$

$$\rho_c \left(\frac{\partial}{\partial t} u + u \frac{\partial}{\partial z} u \right) = - \frac{\partial}{\partial z} p - \tau \frac{\varepsilon}{A} - \rho_c g \quad (3.9)$$

$$\rho_c \left(\frac{\partial}{\partial t} (c_{p,c} T_c) + u \frac{\partial}{\partial z} (c_{p,c} T_c) \right) = \frac{\partial}{\partial t} p + u \frac{\partial}{\partial z} p + q'''_{conv} \quad (3.10)$$

$$\tau = \frac{f}{2} \rho_c u^2 \quad (3.11)$$

$$q'''_{conv} = h \frac{\varepsilon}{A} (T_i - T_c) \quad (3.12)$$

where

ρ_c = coolant density

u = coolant velocity

p = coolant pressure

τ = shear stress

ε = wetted perimeter

A = cross-sectional area

g = gravity

$c_{p,c}$ = coolant specific heat capacity

T_c = coolant temperature

k_c = coolant thermal conductivity

q'''_{conv} = convective heat transfer

f = friction factor

h = heat transfer coefficient

T_i = solid temperature.

$$\begin{aligned}
f &= 8 \left[\left(\frac{8}{Re_{D_h}} \right)^{12} + \frac{1}{(A+B)^{3/2}} \right]^{1/12} \\
A &= \left\{ 2.457 \ln \left(\frac{1}{\left(\frac{7}{Re_{D_h}} \right)^{0.9} + 0.27 \frac{\varepsilon}{D_h} } \right) \right\}^{16} \\
B &= \left\{ \frac{37530}{Re_{D_h}} \right\}^{16}
\end{aligned} \tag{3.13}$$

where

ε = surface roughness.

$$Nu = \frac{hD_h}{k} = 0.023 Re_{D_h}^{0.8} Pr^{0.4} \tag{3.14}$$

where

Nu = Nusselt number

D_h = hydraulic diameter.

3.3 OECD/NEA MHTGR-350 MW Benchmark

The deterministic neutronic thermal-fluids and transient analysis methods available for prismatic HTGRs lag behind the state-of-the-art technologies of other reactors. This delay has motivated the development of more accurate tools for the design and safety evaluations of HTGRs. In addition to the development of new methods, it is essential to define appropriate benchmarks to compare these new methods' capabilities. The OECD/NEA defined such a benchmark [88] using the MHTGR-350 MW reactor [109] as the reference design. The scope of the benchmark is twofold: (1) establish a well-defined problem, based on a common given data set, to compare methods and tools in core simulation and thermal fluids analysis, and (2) test the depletion capabilities of various lattice physics codes available for prismatic HTGRs.

The benchmark defines several Phases and Exercises:

- Phase I: Steady State

1. Neutronics solution with fixed cross-sections.
 2. Thermal fluids solution with given heat sources.
 3. Coupled neutronics-thermal fluids steady state solution.
- Phase II: Transient Cases
 1. Depressurized Conduction Cooldown without reactor trip.
 2. Pressurized Conduction Cooldown with reactor trip.
 3. Water ingress with reactor trip.
 4. Power 100-80-100 load follow.
 - Phase III: Lattice Depletion Case

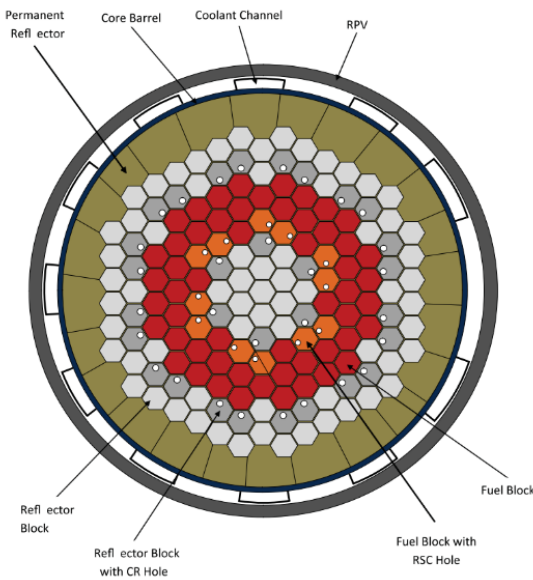
3.4 MHTGR-350 Reactor Description

This section describes the MHTGR-350 reactor. Table 3.1 lists its main characteristics. The core consists of an array of hexagonal fuel elements in a cylindrical arrangement, Figure 3.1. Nineteen graphite replaceable reflector elements compose the inner reflector region. A ring of identically sized graphite replaceable reflector elements surrounds the fuel elements. Then, a region of permanent reflector elements follows the replaceable reflectors. The reactor vessel encases all the elements.

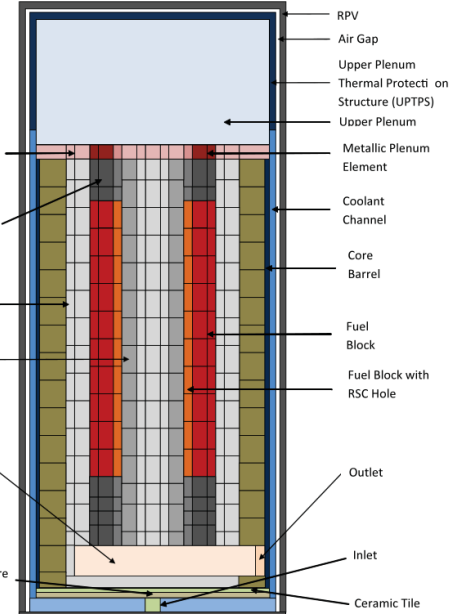
Table 3.1: MHTGR-350 Characteristics [88].

Characteristics	Value
Installed Thermal Capacity	350 MWt
Installed Electric Capacity	165 MWe
Core inlet/outlet Temperature	259/687°C
Power Density	5.9 MW/m ³
Reactor Vessel Outside diam.	6.8 m
Reactor Vessel Height	22 m
Active core radius	2.97 m
Active core height	7.93 m
Top reflector height	1.20 m
Bottom reflector height	1.60 m
Number of fuel columns	66
Number of inner reflector columns	19
Number of outer reflector columns	78

Ten layers of fuel elements stacked on top of each other compose the 66 fuel columns that integrate the active core. Figure 3.1b shows an axial view of the reactor. The core has two types of fuel elements: a standard element



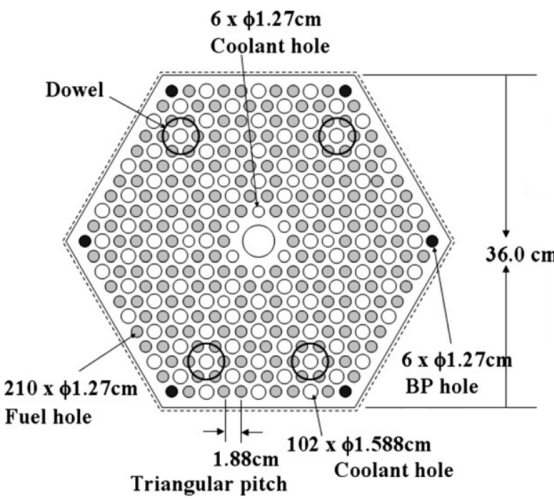
(a) Core radial layout. Image reproduced from [88].



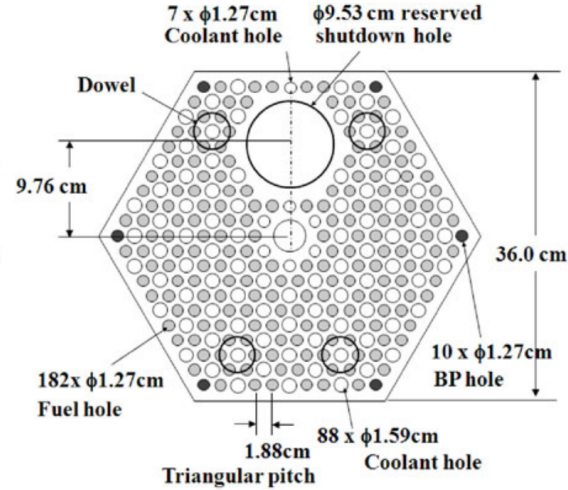
(b) Core axial layout. Image reproduced from [88].

Figure 3.1: MHTGR reactor layout.

and a reserve shutdown element that contains a channel for Reserve Shutdown Control (RSC), Figure 3.2. Table 3.2 specifies the details of the MHTGR-350 fuel elements. Twelve columns in the core contain RSC channels for reserve shutdown borated graphite pellets. Hoppers above the core house the pellets, and if the control rods (CRs) become inoperable, the pellets drop into the channels [88].



(a) Standard fuel assembly. Image reproduced from [118].



(b) RSC fuel assembly. Image reproduced from [116].

Figure 3.2: MHTGR-350 fuel assembly layout.

Table 3.2: MHTGR350 fuel element characteristics [88].

Shared characteristics	Value	Units
Block pitch (flat-to-flat)	36	cm
Fuel length	79.3	cm
Fuel handling diameter	3.5	cm
Fuel handling length	26.4	cm
RSC hole diameter	9.525	cm
RSC center to assembly center	9.756	cm
Fuel/coolant pitch	1.879	cm
Fuel hole radius	0.635	cm
Compacts per fuel hole	15	-
Large coolant hole radius	0.794	cm
Small coolant hole radius	0.635	cm
LBP hole radius	0.635	cm
Block graphite density	1.85	g/cm ³
Standard element		
Number of large coolant holes	120	-
Number of small coolant holes	6	-
Number of fuel holes	210	-
RSC element		
Number of large coolant holes	88	-
Number of small coolant holes	7	-
Number of fuel holes	186	-

The fuel elements contain blind holes for fuel compacts and full-length channels for helium coolant flow. Table 3.3 specifies the details of the TRISO particle and fuel compact designs of the MHTGR-350.

Table 3.3: TRISO and fuel compact characteristics [88].

Characteristic	Value	Units
Fuel	UC _{0.5} O _{1.5}	-
Enrichment (average)	15.5	wt%
Packing fraction (average)	0.35	-
Kernel radius	0.02125	cm
Buffer radius	0.03125	cm
IPyC radius	0.03475	cm
SiC radius	0.03825	cm
OPyC radius	0.04225	cm
Compact radius	0.6225	cm
Compact gap radius	0.6350	cm
Compact length	4.9280	cm
Kernel density	10.50	g/cm ³
Buffer density	1.00	g/cm ³
IPyC density	1.90	g/cm ³
SiC density	3.20	g/cm ³
OPyC density	1.90	g/cm ³
Compact matrix density	1.74	g/cm ³

A combination of Lumped Burnable Poison (LBP) and CRs controls the core reactivity. The LBP consists of boron carbide (B_4C) granules dispersed in graphite compacts. The current design uses six LBP rods per element. Table 3.4 displays the characteristics of the LBP compacts. The reactor has 30 CRs. Six of them are start-up CRs, and their location is the inner reflector. The remaining 24 are operating CRs and control the reactivity during power operation and a reactor trip.

Table 3.4: LBP compact characteristics [88].

Characteristic	Value	Units
Absorber	B_4C	-
Packing fraction	0.109	-
Kernel radius	0.0100	cm
Buffer radius	0.0118	cm
PyC radius	0.0141	cm
Compact radius	0.5715	cm
Compact gap radius	0.6350	cm
Rod length	72.187	cm
Kernel density	2.47	g/cm ³
Buffer density	1.00	g/cm ³
PyC density	1.87	g/cm ³
Compact matrix density	0.94	g/cm ³

Chapter 4

Neutronics

4.1 Preliminary studies

4.1.1 Homogeneous vs. heterogeneous isotope distribution

This section conducted a study to determine the proper way to treat the fuel compact heterogeneities in Serpent. This study modeled two different isotope distributions in a fuel compact: a homogeneous distribution of the isotopes and a heterogeneous distribution, in which we explicitly modeled the TRISO particles.

We used a hexagonal unit cell model that included the fuel compact, a helium gap, and the surrounding graphite. Table 3.3 specifies the model input parameters. The material temperature was 1200K, a case that represents the Hot Full Power (HFP) core state. Serpent ran 5×10^4 neutrons per cycle, 500 active cycles, and 50 inactive cycles for the calculations. The homogeneous distribution simulation took 1.73 and the heterogeneous distribution simulation 2.21 minutes using 256 cores — the heterogeneous calculation took 28% longer.

The multiplication factor (K_{eff}) was 1.17523 for the homogeneous distribution and 1.25106 for the heterogeneous distribution. Using the heterogeneous distribution as a reference, we calculated the relative error of some of the group constants in an eigenvalue calculation. Serpent generated the group constants using the three energy group structure in Table 4.2. The evaluated parameters were D_g , Σ_g^r , $\nu\Sigma_g^f$, and χ_g^t (see Equation 3.1). Figure 4.1 displays the relative errors for Σ_g^r (REMXS) and $\nu\Sigma_g^f$ (NSF), which were the group constants that changed the most. The figure does not include D_g and χ_g^t because their relative errors were less than 1%. The relative errors of Σ_g^r and $\nu\Sigma_g^f$ were less than 6%.

The results show that the homogenization of the fuel compact isotopes decreases the multiplication factor considerably. The impact on the group constants does not seem to be substantial; however, the multiplication factor's considerable difference suggests that the combined effect of the small variations in the group constants is significant. Based on these results, Serpent models the TRISO particles explicitly in the following sections.



Figure 4.1: Relative error of the group constants generated with a homogeneous isotope distribution.

4.1.2 Problem set-up

Diffusion calculations necessitate a spatial homogenization of the group constants. Depending on the desired level of detail, the type of homogenization could vary. For example, in PWR core calculations, the homogenization in space could be per assembly or pin-by-pin [67]. In a per assembly homogenization, the diffusion code models a global neutronic representation of the assembly (we will refer to diffusion calculations using this type as homogeneous calculations). A pin-by-pin homogenization treats the pin or assembly heterogeneities, yielding a detailed neutronic representation of the fuel pins (we will refer to diffusion calculations of this type as heterogeneous calculations).

Previous works [80][101] have used Moltres, a heterogeneous solver, for the analysis of MSRs. In such calculations, Moltres input files defined two materials: the moderator and the fuel. For such a configuration, a node in the mesh representing the moderator holds the neutronics and temperature information only for the moderator. The same is true in the fuel. A homogeneous calculation would not differentiate between moderator and fuel and would hold the information of both materials in each node.

Keeping in mind Moltres previous works, this work aimed for a heterogeneous calculation in a prismatic HTGR. We modeled a fuel column of the MHTGR-350 and generated the group constants using Serpent. Figure 4.2 displays the Serpent model geometry. We obtained the group constants for three materials: moderator, coolant, and fuel compact. Serpent ran 5×10^5 neutrons per cycle, 400 active cycles, and 100 inactive cycles for the calculations. Taking advantage of the problem's symmetry, Moltres modeled only one-twelfth of the fuel column shown in Figure 4.2. We made the geometry and mesh using Gmsh [40]. The diffusion calculation had 183667 degrees of freedom (DoFs)/energy-group. Moltres input file set an eigenvalue convergence tolerance of 1×10^{-8} . The calculation used a two energy group structure with a thermal cutoff at 0.625eV. The eigenvalue calculation did not converge. Although several factors could contribute to this behavior, we focused on the validity of the diffusion calculations in such a

system.

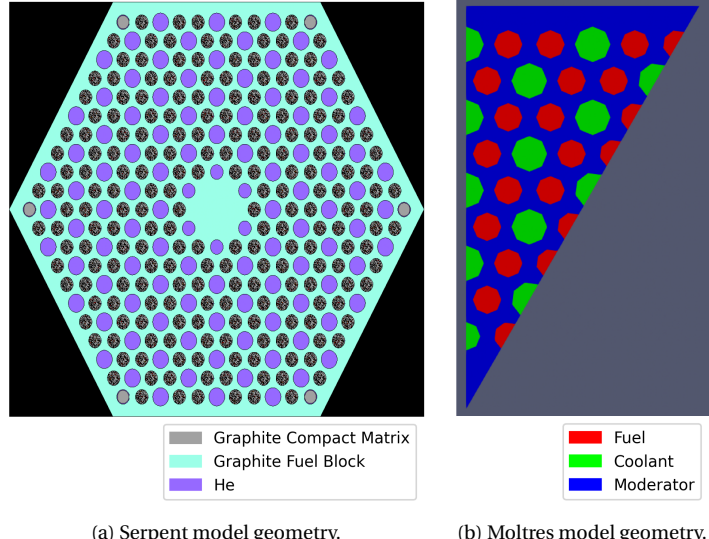


Figure 4.2: Fuel column of the MHTGR-350. xy -plane in the active core region.

The diffusion theory considers that the current density is proportional to the gradient of the flux [74]. Such an approximation relies on the following assumptions:

- The angular flux does not depend strongly on the angular variables.
- The fission source is isotropic.
- The time derivative of the current density is small compared to the mean collision time.
- The anisotropic energy-transfer is negligible in group-to-group scattering.

More detailed studies of the transport equation indicate that the following cases violate the assumption of a weak angular dependence [32]:

- Regions near vacuum boundaries and low-density material regions.
- Regions near strongly absorbing media.
- Regions near localized sources.

The diffusion theory applies best to geometries consisting of large homogeneous regions where the flux gradient is small. This is the case for material regions whose geometrical scales are considerably larger than the neutron mean free path. For this reason, we compared the neutron mean free path in the different fuel assembly materials, Table 4.1. The mean free path in the fuel compact and the moderator are in the order of the centimeters. In the

coolant, the mean free path magnitude is comparable to the fuel column dimensions. These results suggest that a heterogeneous diffusion calculation of the prismatic fuel column violates the diffusion theory assumptions.

Table 4.1: Neutron mean free path in different materials. Values expressed in cm .

	Fuel compact	Moderator	Coolant	Homogeneous fuel
Fast	2.71	2.70	1137.31	3.37
Thermal	2.22	2.36	1945.49	2.89

Next, we conducted a feasibility study for the homogeneous calculation of the fuel assembly in Moltres. Serpent calculated the homogeneous group constants of the fuel assembly. We homogenized the fuel, coolant, and moderator to create a 'homogeneous fuel.' This material's mean free path is in the order of the centimeters, Table 4.1. Next, Moltres used the homogeneous group constants to carry out an eigenvalue calculation. Comparing Moltres results with Serpent results, Serpent's K_{eff} was 1.41933 while Moltres' was 1.4078788. Moltres eigenvalue is smaller than Serpent's eigenvalue. Additionally, Figure 4.3 displays a comparison between the axial flux in the fuel column obtained with serpent versus Moltres. Serpent's flux is the average flux over the fuel column volume; Moltres flux is the point-wise flux over the z -axis. The fluxes are similar in shape and magnitude.

We empathize that this was a feasibility study. The following sections make a more in-depth analysis of more detailed results. Based on these results and discussion, we use Moltres for carrying out homogeneous calculations in the following sections.

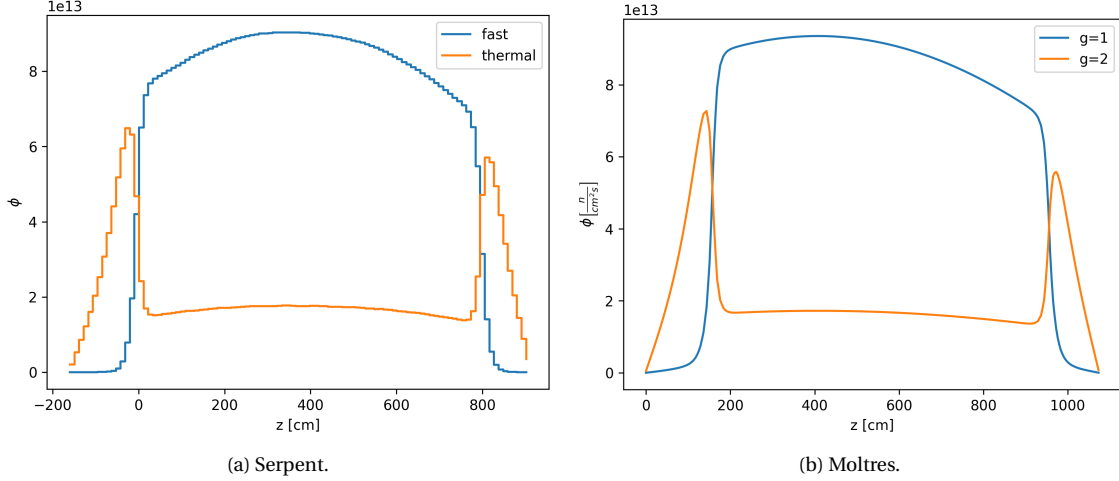


Figure 4.3: Two group axial flux comparison.

4.2 Serpent-Moltres comparison

4.2.1 Fuel column

Table 4.2: Energy group structure.

Upper boundary [eV]	26	21	18	15a	15b	15c	15d	15e	12	9	6	3
1.49E+07	1	1	1	1	1	1	1	1	1	1	1	1
7.41E+06	2											
3.68E+06	3	2	2	2	2	2	2	2	2	2		
6.72E+05	4											
1.11E+05	5	3	3	3	3	3	3	3	3	3	2	2
1.93E+04	6	4	4	4	4					4		
3.35E+03	7											
1.58E+03	8	5	5			4						
7.48E+02	9	6	6	5	5			4	4	5	3	
2.75E+02	10	7	7	6	6	5				6	4	
1.30E+02	11	8	8	7	7			5	5	7	5	3
6.14E+01	12	9			8	6						
2.90E+01	13	10	9	8	9			6	6			
1.37E+01	14	11	10	9						8	6	
8.32E+00	15	12	11	10	10	7	7	7	9			
5.04E+00	16											
2.38E+00	17	13	12	11	11	8	8	8	10	7	4	3
1.29E+00	18	14										
6.50E-01	19	15	13	12	12	9	9	9	11	8	5	
3.50E-01	20	16				10	10					
2.00E-01	21	17	14	13	13	11	11	10				
1.20E-01	22							11				
8.00E-02	23	18	15	14	14	12	12	12				
5.00E-02	24	19	16			13	13	13				
2.00E-02	25	20	17	15	15	14	14	14	12	9	6	
1.00E-02	26	21	18			15	15	15				

This section investigated the effects of the energy group structure on the diffusion simulations. We conducted two analyses: first, we varied the number of energy groups, second, we varied the energy group structures with a constant number of energy groups. To reduce the computational expense, we narrowed down our focus to a fuel column of the MHTGR-350, Figure 4.2. Tables 3.2 and 3.3 specify the model input parameters.

The first step in the calculation was to obtain the group constants using Serpent. Figure 4.2 displays a xy -plane of the model. To simplify Serpent's model, we did not consider the fuel handling holes or the bottom and top reflectors' coolant channels. HTGRs use LBPs to reduce the power peaking factors in different active core regions. Some reactors could have LBPs in the rings closer to the reflectors, and no LBPs in the middle rings. This characteristic motivated the analysis of two cases: one fuel column that does not have LBPs and one that does. The LBPs' locations are the six corners of the fuel assembly, Figure 3.2. The material temperatures were 600K and 1200K, cases that

represent the Cold Zero Power (CZP) and the HFP core states. Serpent ran 4×10^5 neutrons/cycle, 360 active cycles, and 40 inactive cycles for the calculations.

Taking advantage of the problem's symmetry, Moltres modeled only one-twelfth of the fuel column. We made the geometry and mesh, which had 37,120 elements and 22,862 nodes, using Gmsh.

The diffusion calculations had 22,862 DoFs/energy-group. The Moltres input files set an eigenvalue and a flux convergence tolerance of 1×10^{-8} . Moltres calculations used different energy group structures listed in Table 4.2.

To compare the results from Serpent and Moltres, we present a comparison of the three-group axial fluxes. Moltres ran the calculations for 26 energy groups and collapsed the results into three energy groups to facilitate the results' visualization. Note that Serpent's flux is an average over the volume, while the Moltres' flux is the point-wise flux over a line. Another figure compares the eigenvalue from Serpent and eigenvalues from Moltres for the different energy group structures. The last analysis is for the Moltres axial flux. Considering the 26 group structure as the reference value, we obtained the L_2 -norm of the active core's axial flux relative error.

To recapitulate, we simulated four operational cases: no LBP at 600K, no LBP at 1200K, LBP at 600K, and LBP at 1200K. Figures 4.4 to 4.7 display the axial flux from the Serpent and the Moltres simulations for all cases. For the no LBP at 600K case, the fluxes are close in shape and magnitude. For the no LBP at 1200K case, the fluxes look similar. The flux in Moltres has a straighter shape. The thermal flux peak in the bottom reflector is bigger. For the LBP at 600K case, the flux in Moltres has a larger magnitude. Additionally, the shape of the Moltres flux is concave, while the Serpent flux is convex. For the LBP at 1200K case, the flux in Moltres is larger and more concave than Serpent flux. Overall, the fluxes in Moltres and Serpent are close in shape and magnitude.

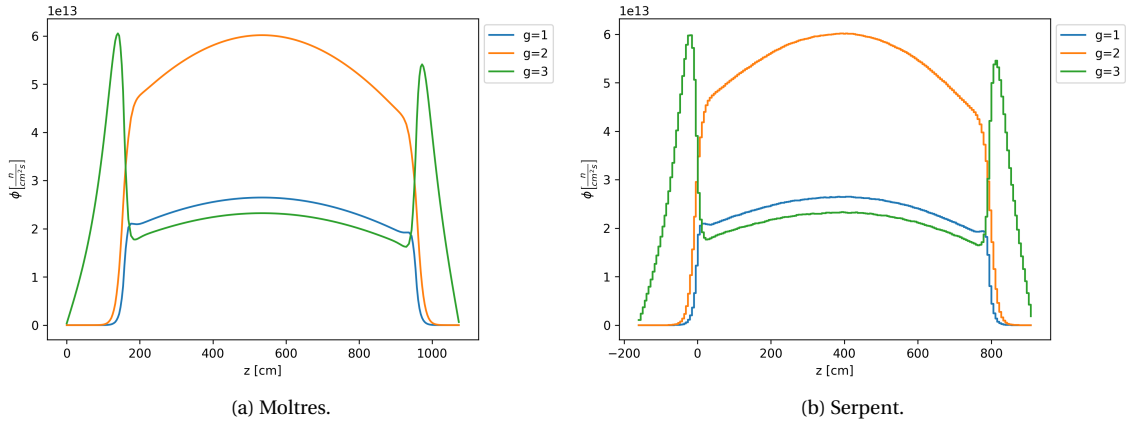


Figure 4.4: Case no LBP at 600K. 3-group axial neutron flux.

Table 4.3 exhibits the reactivity difference ($\Delta\rho$) between the Serpent and Moltres eigenvalues. We used equation 4.1 to obtain $\Delta\rho$. The eigenvalues in Moltres differ slightly from the eigenvalues in Serpent. Overall, the reactivity difference is less than 50 pcm. We note that the number of energy groups does not affect the accuracy of the



(a) Moltres. (b) Serpent.

(a) Moltres. (b) Serpent.

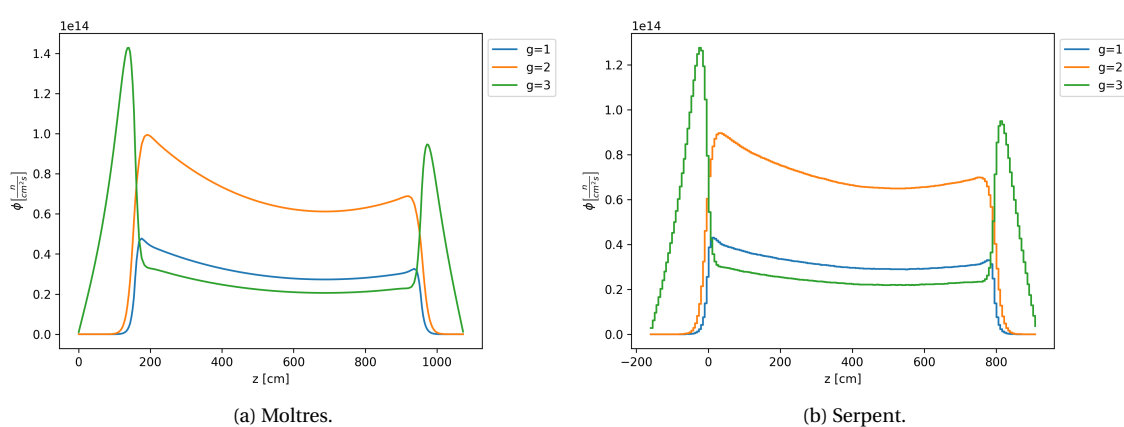
Figure 4.5: Case no LBP at 1200K. 3-group axial neutron flux.



(a) Moltres. (b) Serpent.

(a) Moltres. (b) Serpent.

Figure 4.6: Case LBP at 600K. 3-group axial neutron flux.



(a) Moltres. (b) Serpent.

(a) Moltres. (b) Serpent.

Figure 4.7: Case LBP at 1200K. 3-group axial neutron flux.

eigenvalue calculations in Moltres.

$$\Delta\rho = \left| \frac{k_1 - k_2}{k_1 k_2} \right| \quad (4.1)$$

where

k_1 = Serpent eigenvalue

k_2 = Moltres eigenvalue.

Table 4.3: Serpent and Moltres eigenvalues.

	Serpent	$\Delta\rho$ [pcm]							
		3	6	9	12	15	18	21	26
no LBP, 600K	1.43800	10	7	6	6	5	6	6	12
no LBP, 1200K	1.37771	23	15	4	3	2	2	1	11
LBP, 600K	1.12861	44	21	24	25	25	24	19	9
LBP, 1200K	1.06554	36	40	29	32	44	43	25	25

Figures 4.8 and 4.9 show the L_2 -norm of the relative error for the different energy group structures. The no LBP case's relative error is smaller than the LBP case's relative error. Overall, the relative error decreases with an increase in the number of energy groups. Nonetheless, this is not always the case. For example, in Figure 4.8b, going from 12 to 15 groups, the thermal flux improves, but the fast flux worsens. Additionally, we observe that a low number of energy groups yields more than 100% error. In which case, we can conclude that the solution is wrong.

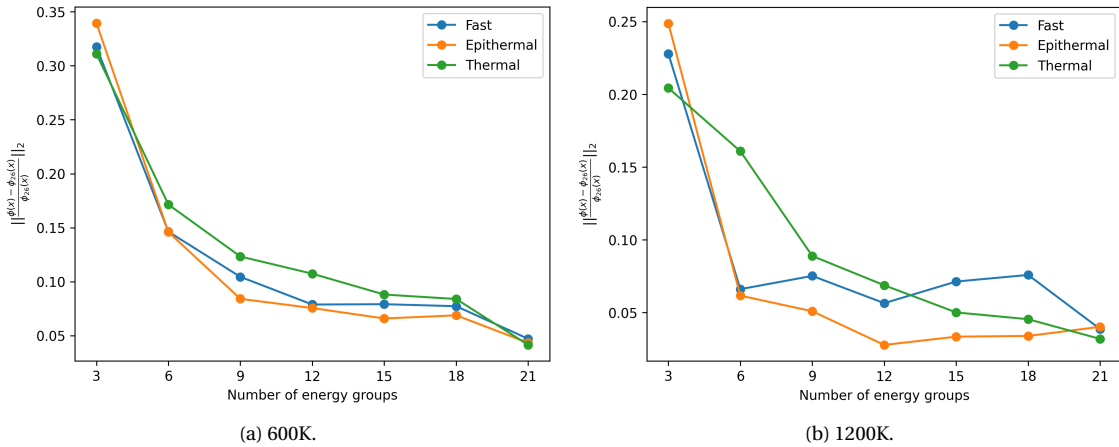


Figure 4.8: No LBP case. L_2 -norm relative error for different number of energy group structures.

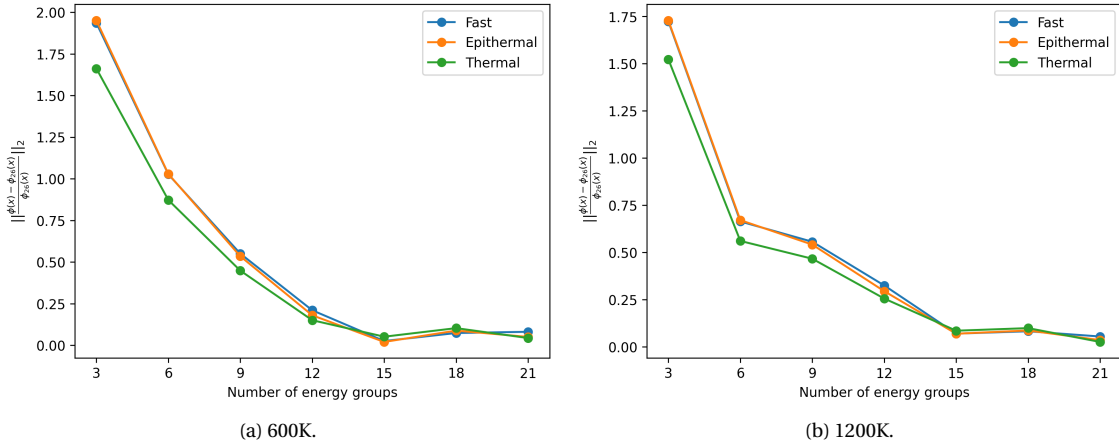


Figure 4.9: LBP case. L_2 -norm relative error for different number of energy group structures.

We added to the analysis the computational time and the peak memory usage during the simulations, Figure 4.10. All the simulations used 128 cores. We present only the cases at 600K because the impact of the temperature change was not significant. The computational requirements rise with an increase in the number of energy groups. As the geometry uses a constant number of elements, the DoFs/energy-group is constant for all the simulations. Thus, the total number of DoFs is proportional to the number of energy groups. We also discern that the overall time of the LBP cases is higher than the no LBP cases.

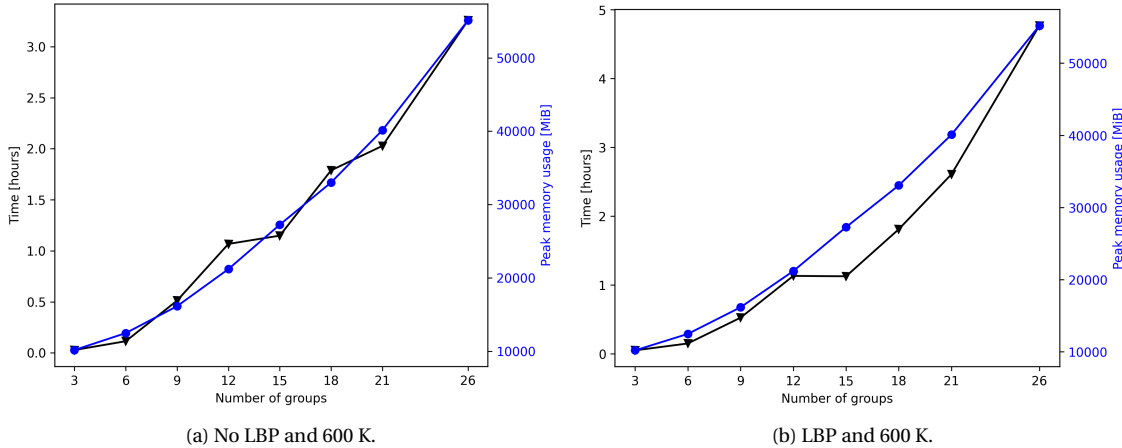


Figure 4.10: Computational time and memory requirements for different number of energy group structures.

Finally, we analyzed the impact of changing the energy group structure for a constant number of energy groups. We chose 15 energy groups, as it yields a good overall accuracy and a not so high computational expense. Table 4.2 holds the different energy group structures. Table 4.4 exhibits the L_2 -norm of the relative error for the different energy group structures. The energy group structure has an impact on accuracy. Some energy group structures

yield better results for some cases while giving worse results for others. For example, the structure 15d gives better results for the LBP at 600K case than for the no LBP case at 600K. To choose the best performing structure, we used a weighted average for the different groups. We arbitrarily chose the weights to be 0.5, 0.3, and 0.2 for the thermal, epithermal, and fast fluxes. Using this averaging scheme, we determined the group structure 15d to be the best one.

Table 4.4: Axial flux relative error L_2 -norm for various energy group structures. Values expressed in percentage.

LBP	Temperature [K]	Flux	15a	15b	15c	15d	15e
No	600	Fast	7.9	8.0	8.2	8.1	9.1
		Epithermal	6.6	6.5	8.6	8.2	9.2
		Thermal	8.8	8.5	10.6	10.7	12.9
	1200	Fast	7.1	7.7	5.7	5.1	4.5
		Epithermal	3.3	3.9	6.2	5.1	3.4
		Thermal	5.0	4.7	8.5	8.2	8.4
Yes	600	Fast	24.0	24.8	2.6	2.3	3.7
		Epithermal	21.0	21.7	2.0	1.6	2.7
		Thermal	18.1	18.8	5.2	5.5	5.7
	1200	Fast	36.2	37.3	6.9	6.6	25.9
		Epithermal	33.2	34.2	6.9	6.5	25.1
		Thermal	29.6	30.6	8.5	8.3	20.3
Weighted average			17.3	17.8	6.3	6.0	10.8

4.2.2 Full-core

This section compared the results from Serpent and Moltres for a full-core simulation. The first step in the calculation was to obtain the group constants using Serpent. Figure 4.11 displays the xy -plane of the model, which includes the bottom and top reflectors. Tables 3.1, 3.2, and 3.3 specify the model input parameters. For simplicity, all the fuel columns were standard. The model considered a fresh core, and it did not include the fuel handling holes nor the bottom and top reflectors' coolant channels. Based on the previous section analyses, we chose the energy group structure 15d in Table 4.2. The material temperatures were 600K and 1200K, cases that represent the CZP and the HFP core states. Serpent ran 8×10^5 neutrons per cycle, 500 active cycles, and 100 inactive cycles for the calculations.

Taking advantage of the problem's symmetry, Moltres modeled only one-twelfth of the fuel column, Figure 4.11. We made the geometry and mesh, which had 300,720 elements and 160,035 nodes, using Gmsh. The diffusion calculations had 160,035 DoFs/energy-group and a total of 2,400,525 DoFs. The Moltres input files set an eigenvalue and a flux convergence tolerance of 1×10^{-8} .

Between Serpent and Moltres, we compared the K_{eff} , the power distribution, and the flux shape and magnitude in different zones of the reactor. Table 4.5 exhibits the K_{eff} from Serpent and Moltres. Moltres values are larger than Serpent's. The values are within a 300 pcm difference.



Figure 4.11: MHTGR-350 full-core models.

Table 4.5: Serpent and Moltres eigenvalues.

	Serpent	Moltres	$\Delta\rho$ [pcm]
600K	1.10869	1.11150	228
1200K	1.06138	1.06468	292

Figures 4.12 and 4.13 show Serpent and Moltres radial power distributions. The following analysis applies to both temperatures. Regarding the power distribution, the results are symmetric with respect to a 60° line. This suggests that we could reduce the mesh size by almost half by considering only one-twelfth of the reactor. Next, we observe that Moltres result exhibits a higher power density than Serpent in the inner and outer rings but a lower power density in the middle ring. The largest difference occurs at 600K, Figure 4.12. It is in the inner ring and has a magnitude of 0.29 MW.

We placed axial and radial flux detectors in arbitrary regions of the reactor to compare the fluxes, Figure 4.14 shows their locations. Both the Serpent and Moltres radial detector's axial location was the middle of the active core's height. Note that the flux in Serpent is an average over the fuel column's volume, while the flux in Moltres is the point-wise flux over the fuel column's centerline. The Serpent radial detector's volume had a 2° -angle and a fuel assembly's height. Moltres ran the calculations for 15 energy groups and collapsed the results into three groups to facilitate the results' visualization. Figures 4.15 and 4.16 show the axial and radial fluxes at 600K. The axial flux shapes are similar, but Figure 4.15 shows that the fast and epithermal axial fluxes in Moltres are larger, while the axial thermal flux is smaller. The axial epithermal and thermal fluxes are closer in magnitude in the active core in Serpent's simulation. In Figure 4.16, Serpent fluxes present some 'noise.' A higher number of generations per cycle in Serpent simulations or using a detector with a larger volume would eliminate this. Additionally, the



Figure 4.12: Radial power distribution at 600 K.



Figure 4.13: Radial power distribution at 1200 K.

radial flux in Serpent reveals the location of the LBPs in the fuel assemblies. A diffusion solver fails to capture such localized effects as the group constants are homogeneous in the fuel assembly. The radial fast flux in Moltres is larger, while the radial epithermal and thermal fluxes have almost the same magnitudes. Figures 4.17 and 4.18 display the fluxes at 1200K, which differ from the 600K case. Still, we observe the same behavior for both axial and radial fluxes. Overall, Moltres and Serpent fluxes are comparable in magnitude and shape.

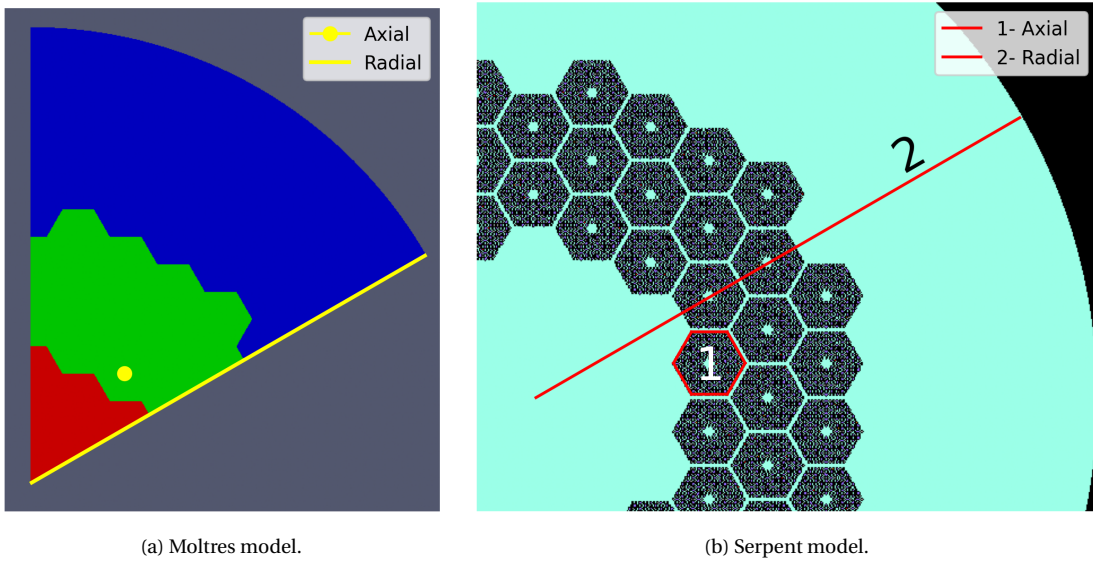


Figure 4.14: Axial view of the flux detector locations.

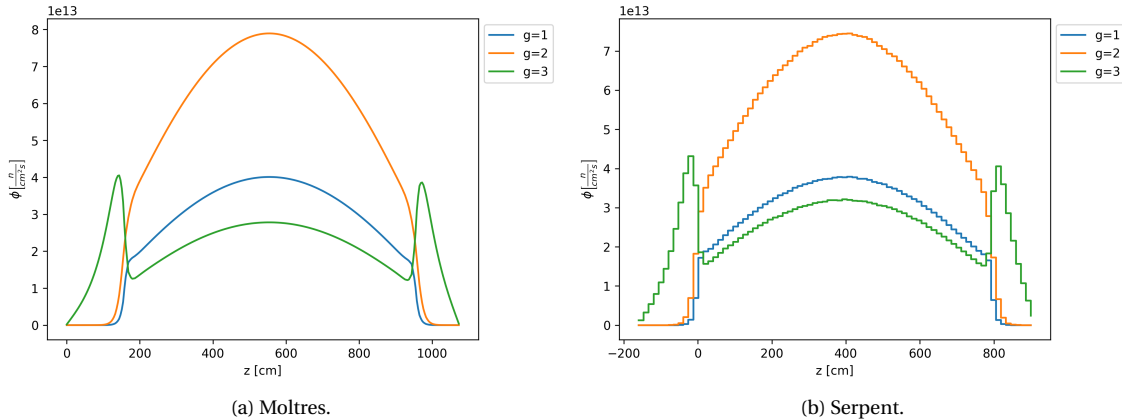


Figure 4.15: Axial flux at 600 K.



Figure 4.16: Radial flux at 600 K.



Figure 4.17: Axial flux at 1200 K.



Figure 4.18: Radial flux at 1200 K.

4.3 OECD/NEA MHTGR-350 MW Benchmark: Phase I Exercise 1

This section conducted Phase I Exercise 1 of the benchmark with Moltres and compared the results with those already published [89]. The benchmark specifies the group constants required to conduct the exercise. The group constants provision ensures a common dataset among various benchmark participants and allows for comparing stand-alone neutronic predictions with no thermal-fluids feedback. The exercise requests the reporting of the global parameters: K_{eff} , CR worth ($\Delta\rho_{CR}$), and axial offset (AO). It also requires the reporting of a power distribution map [88]. Equations 4.2 and 4.3 define $\Delta\rho_{CR}$ and AO .

$$\Delta\rho_{CR} = \frac{k_{out} - k_{in}}{k_{out}k_{in}} \quad (4.2)$$

where

k_{out} = eigenvalue with CR out (at position 1184.8 cm)

k_{in} = eigenvalue with CR in (at position 391.81 cm)

and

$$AO = (TP_{top} - TP_{bottom}) / (TP_{top} + TP_{bottom}) \quad (4.3)$$

where

TP_{top} = total power produced in the top half core

TP_{bottom} = total power produced in the bottom half core.

Moltres modeled one-third of the reactor, Figure 4.19. The model included the bottom and top reflectors, and the core comprised 232 hexagonal subdomains for which the benchmark provides group constants. Table 4.6 lists the six macroscopic regions that we can differentiate in the model. The simulations required two meshes: one for the CR out and one for the CR in. The simulation with the CR out had 268,393 DoFs/energy-group, and a total of 6,978,218 DoFs. The simulation with the CR in had 227,592 DoFs/energy-group, and a total of 5,917,392 DoFs. The Moltres input files set an eigenvalue convergence tolerance of 1×10^{-8} .

The benchmark exercise specifies the group constants and a map with their location. The benchmark definition used DRAGON-4 [82] to obtain the group constants from a full block configuration. The dataset contains 26 energy



Figure 4.19: 1/3-rd of the MHTGR-350 geometry.

Table 4.6: Macroscopic regions.

Macroscopic region	Subdomains
Fuel	1 to 220
Bottom reflector	221 to 224
Inner reflector	225
Outer reflector	226-227
Top reflector	228 to 231
Control Rod	232

groups. Because the benchmark group constant format differs from the Moltres format, we made a Python script to handle the differences. Among the benchmark group constants, we find Σ_g^t , D_g , $\nu\Sigma_g^f$, Σ_g^f , χ_g^t , and $\Sigma_{g' \rightarrow g}^s$ (see equation 3.1).

The benchmark exercise sets periodic boundary conditions (BCs) on the sides of the geometry; however, a memory issue did not allow for implementing those BCs in our 26-group Moltres input file. We approximated the periodic BC with the reflective BC. Section 4.3.1 discusses further the use of periodic and reflective BCs.

On average, the simulations took 4.22 hours using 1024 cores. Table 4.7 shows the main results. These include: Moltres predicting a K_{eff} larger than the reference result, the reactivity difference being 99 pcm, Moltres yielding a smaller control rod worth (difference being 312 pcm), and the axial offset for the Moltres simulation being 4% higher than the reference result. We attribute the discrepancies to the use of the reflective BCs instead of the periodic BCs. Once again, Section 4.3.1 discusses further the use of periodic and reflective BCs.

Table 4.7: Global parameters.

Parameter	Benchmark	Moltres
K_{eff}	1.06691	1.06804
$\Delta\rho_{CR}$ [pcm]	822.1	509.8
AO	0.168	0.1753

Figure 4.20 shows the radially averaged axial power distribution. Figure 4.21 shows the axially averaged radial power distribution. In both figures, Moltres' values are similar to the reference results. Moltres' power distribution in the inner ring is larger. The differences are within 0.25 W/cm³.

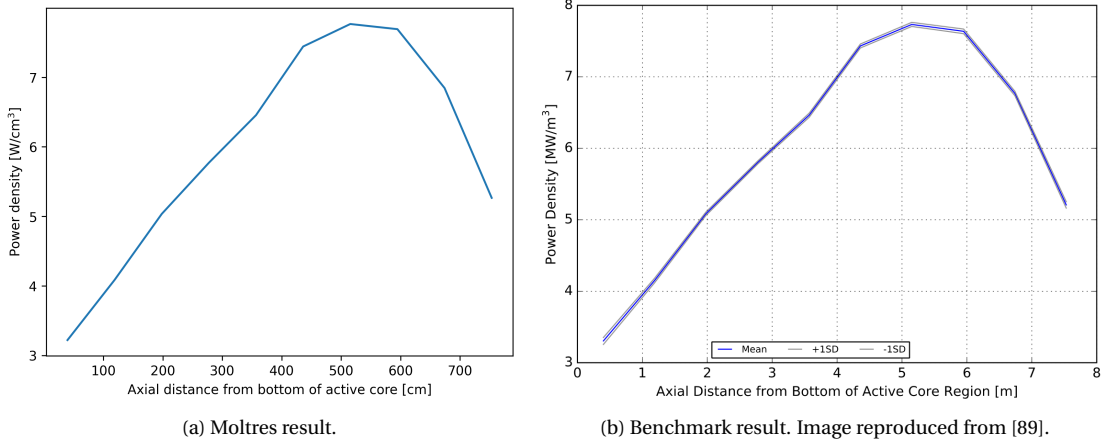


Figure 4.20: Radially averaged axial power distribution.

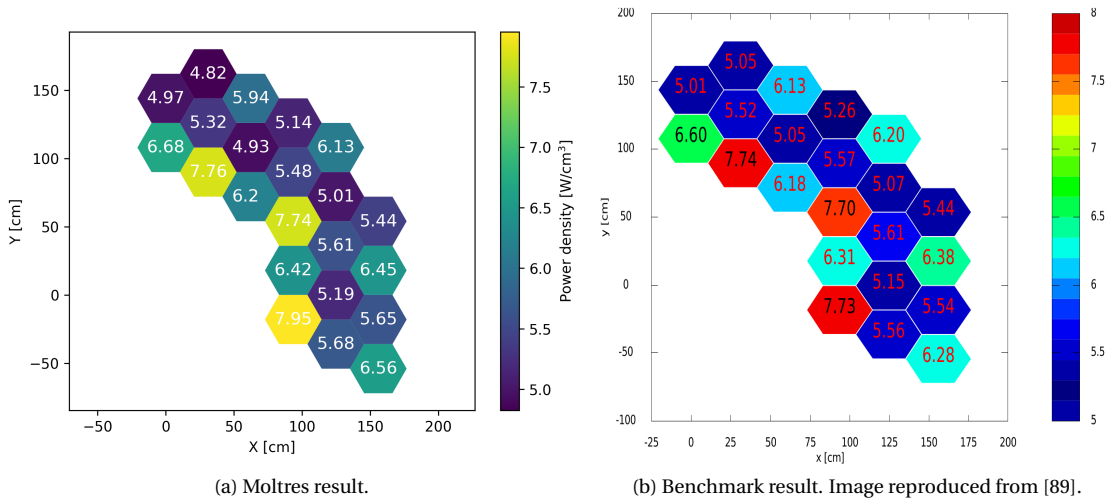


Figure 4.21: Axially averaged radial power distribution.

4.3.1 Periodic vs Reflective Boundary Conditions

In the last section, we observed deviations in Moltres results. This section will analyze the discrepancies that the reflective BC approximation may introduce. As the previous section mentioned, the simulation's memory requirements restrict the use of periodic BCs. To reduce the memory requirements, we collapsed the group constants to a smaller number of energy groups. We simulated two cases: one that uses a 3-group structure and one that uses a 6-group structure (see Table 4.2).

The simulations required two meshes each: one for the CR out and one for the CR in. The 3-group simulation had 62,118 DoFs/energy-group (total of 186,354 DoFs) and 61,596 DoFs/energy-group (total of 184,788 DoFs) for the CR out and CR in cases, respectively. The 6-group simulation had 16,898 DoFs/energy-group (total of 101,388 DoFs) and 19,116 DoFs/energy-group (total of 114,696 DoFs) for the CR out and CR in cases, respectively. We highlight that the 6-group simulation had to use a coarser mesh; otherwise, it would not run. This fact confirms the suspicion that the simulation's memory requirements prevent it from running.

We ran simulations with periodic and reflective boundary conditions for both cases and compared their results, as seen in Table 4.8. K_{eff} rises with the reflective BC. With the CR out, the raise is small. However, with the CR in, the increase is considerable. The combined effect of both increases leads to a decrease in the control rod worth. The BC approximation barely affects the axial offset.

Table 4.8: Global parameters comparison for different types of BCs.

Energy groups	Type of BCs	$K_{eff,out}$	$K_{eff,in}$	$\Delta\rho_{CR}$ [pcm]	AO
3	Periodic	1.07571	1.06776	692.6	0.237
	Reflective	1.07586	1.07021	490.5	0.237
6	Periodic	1.07182	1.06356	724.3	0.185
	Reflective	1.07197	1.06610	513.3	0.186

4.4 Conclusions

The preliminary studies focused on several aspects of the simulations. The first aspect was the effect of distributing the fuel compact isotopes homogeneously in the Serpent model. The results showed that the homogenization of the fuel compact isotopes decreased the multiplication factor considerably, as the heterogeneous calculation took 28% longer. Additionally, the homogeneous distribution appeared not to have a substantial impact on the group constants. However, the multiplication factor's considerable difference suggested that the combined effect of the group constants' small variations was significant. Although the particles' explicit modeling is time-consuming, it is necessary.

The next section studied the problem set-up in Moltres. Moltres uses a heterogeneous diffusion solver, making it applicable to reactor technologies that allow for heterogeneous diffusion calculations. In this work, we aimed to use Moltres to solve prismatic HTGRs. Nevertheless, the diffusion approximation fails to properly model regions where the mean free path is comparable to the region's dimensions. The presence of helium in the fuel assembly of a prismatic HTGR prohibits heterogeneous diffusion calculations. Based on this discussion, we adapted the input group constants to use Moltres as a homogeneous diffusion solver.

Focusing on a fuel column of the MHTGR-350, we investigated the effects of the energy group structure on the diffusion calculations. We considered four different operational cases: a fuel column without LBPs and a fuel column with LBPs, both cases at 600K and 1200K. Serpent obtained the homogenized group constants of the fuel column. Then, Moltres took such constants as input with a Gmsh mesh. The first study compared the Moltres axial flux to Serpent axial flux. Moltres used a 26 energy group structure to run the simulations. Overall, the axial fluxes were close in shape and magnitude. A different study focused on the effects of the energy group structure on the K_{eff} . The number of energy groups did not affect the accuracy of the Moltres eigenvalue calculations. We also compared the L_2 -norm of the axial flux relative error in the active core using different energy group structures. For the four operational cases, increasing the number of energy groups improved the accuracy. Additionally, we presented the simulation's computational expense for the different number of energy groups. The simulation time and memory requirement rose by increasing the number of energy groups. The computational time increased as well for the fuel column with LBPs. Finally, we analyzed the impact of using different 15-group structures on the

L_2 -norm of the axial flux relative error. We chose $15d$ as the best-performing energy group structure.

Based on the fuel column analysis results, we compared Moltres full-core results with Serpent reference results. We considered two operational cases: 600K and 1200K. Serpent obtained the homogenized group constants of the different regions of the reactor, and again, Moltres took such constants as input with a Gmsh mesh. The first analysis compared the Serpent and Moltres eigenvalues — Moltres results were bigger, but the overall differences were less than 300 pcm. The second analysis compared the radial power distributions from both codes. These results showcased the symmetry of the problem. Reducing the problem size by half, other simulations could reduce their computational expense. For the most part, Moltres radial power distribution showed proximity to the Serpent's result. We also compared Moltres and Serpent fluxes in two directions (axial and radial) in arbitrary core regions. The axial fluxes showed small discrepancies, mostly in their magnitude. The radial fluxes were close in shape and magnitude; however, the radial flux in the diffusion calculation failed to capture the flux variation near the LBPs. Overall, the fluxes were similar.

The simulation capabilities for prismatic HTGRs have not reached state of the art of LWRs. This development delay motivated OECD/NEA to define a benchmark, which uses the MHTGR-350 as the reference design, to carry out code-to-code comparisons. We conducted Phase I Exercise 1 with Moltres, using the group constants defined by the benchmark. The group constants have a 26-energy group structure, and the exercise sets periodic BCs on the sides of the geometry. The simulation's high memory requirements have challenged such implementation in Moltres. To circumvent this, we approximated the periodic BC with a reflective BC. Two out of three global parameters exhibited good agreement with the reference results; however, the control rod worth presented a large discrepancy, a consequence of the BC approximation. Reducing the problem's size by collapsing the group constants to 3 and 6-energy groups, we compared the K_{eff} using the periodic and reflective BCs. A reflective BC for the CR out case did not substantially impact the K_{eff} , but the BC choice for the CR in case had a significant effect. The combined effect of the approximation led to a large error in the CR worth, while it had only a small influence on the axial offset.

Chapter 5

Thermal-fluids

5.1 Preliminary studies

This section carries out some preliminary studies using Moltres and MOOSE heat conduction module to solve the prismatic HTGR thermal-fluids.

5.1.1 Verification of the thermal-fluids model

To verify our methodology, this section solved a simplified cylindrical model whose analytical solution we know. Section 8.2 presents the analytical solution of the problem. Moltres/MOOSE obtained the numerical solution of the thermal-fluid equations from Section 3.2.2.

Figure 5.1 displays the model geometry, which differentiates five subregions: fuel compact, helium gap, moderator, film, and coolant. Table 5.1 summarizes the geometry dimensions and the input parameters. The model reference design was the GT-MHR. The calculated moderator radius is the fuel/coolant pitch minus the fuel compact and coolant channel radii, which is the minimum distance between the fuel and coolant channels in the unit cell. We obtained the calculated coolant radius by preserving the coolant channel volume. The model assumed a sinusoidal power profile in the z -direction.

Figure 5.2 shows the axial and radial temperature profiles. Both analytical and numerical solutions exhibit good agreement. The outlet coolant temperature is 770.2 °C whereas the average outlet coolant temperature of the reference reactor is 950 °C. Note that this is a simplified model only for verifying that the numerical solution agrees with the analytical solution. Also, the model considers only one fuel channel while in the GT-MHR unit cell, two fuel channels deposit their heat into one coolant channel.

5.1.2 Unit cell problem

This section solved the unit cell problem in the hot spot of an HTGR. We intended to reproduce In et al. 2006 [53] in an effort to validate the unit-cell model. We chose this article as it solves a three-dimensional unit-cell model and gives one of the most complete descriptions in the open literature. Table 5.2 presents the problem characteristics.

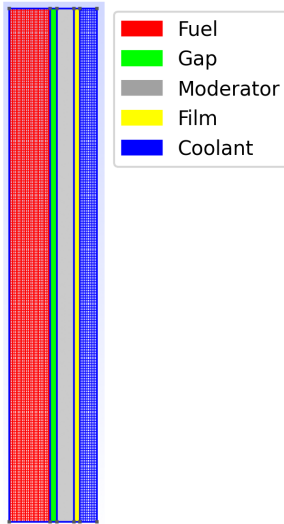


Figure 5.1: Scaled-down version of the model geometry.

Table 5.1: Problem characteristics.

Parameter	Symbol	Value	Units	Reference
Fuel compact radius	R_f	0.6225	cm	[53]
Fuel channel radius	R_g	0.6350	cm	[53]
Coolant channel radius	-	0.7950	cm	[53]
Fuel/coolant pitch	-	1.8850	cm	[53]
Fuel column height	L	793	cm	[53]
Coolant mass flow rate	\dot{m}	0.0176	kg/s	[53]
Average power density	q_{ave}	35	W/cm ³	[53]
Coolant inlet temperature	T_{in}	400	°C	[53]
Helium inlet pressure	P	70	bar	[53]
Helium density	ρ_c	4.940×10^{-6}	kg/cm ³	[91]
Helium heat capacity	$c_{p,c}$	5188	J/kg/K	[91]
Fuel compact thermal conductivity	k_f	0.07	W/cm/K	[118]
Gap thermal conductivity	k_g	3×10^{-3}	W/cm/K	[118]
Moderator thermal conductivity	k_m	0.30	W/cm/K	[118]
Calculated parameters				
Calculated moderator radius	R_m	1.080	cm	-
Coolant film radius	R_i	1.090	cm	-
Calculated coolant radius	R_c	1.349	cm	-
Coolant average velocity	v_c	1794.33	cm/s	-
Film thermal conductivity	k_i	1.722×10^{-3}	W/cm/K	-

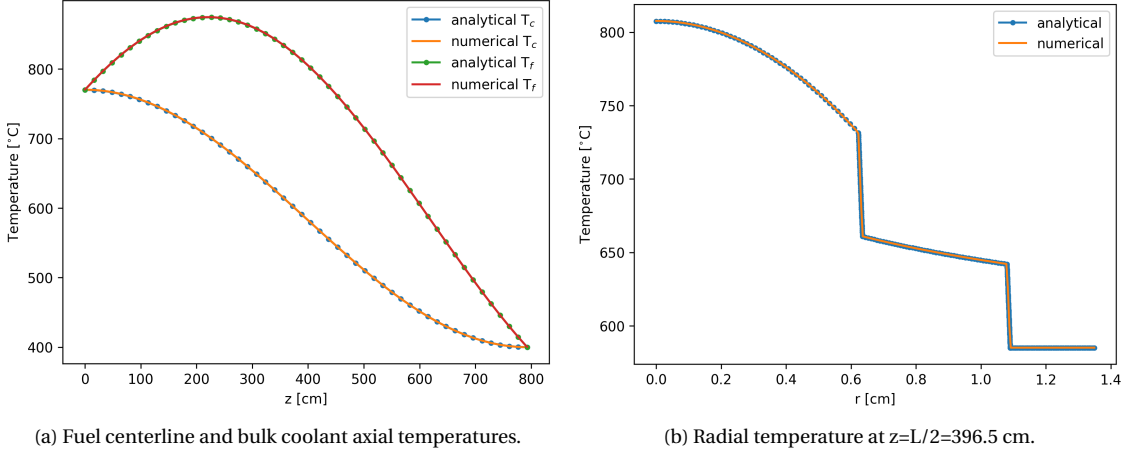


Figure 5.2: Temperature profiles.

The material properties specification of the solids is missing in the article, and we replaced them with parameters from Tak et al. 2008 [118]. Figure 5.3 displays a XY -plane of the model geometry and the material properties that depend on the temperature. Additionally, In et al. used a chopped cosine as the power profile. To simplify the analysis, we used the average value of the power profile.

Table 5.2: Problem characteristics.

Parameter	Symbol	Value	Units	Reference
Fuel compact radius	R_f	0.6225	cm	[53]
Fuel channel radius	R_g	0.6350	cm	[53]
Coolant channel radius	R_c	0.7950	cm	[53]
Fuel/coolant pitch	p	1.8850	cm	[53]
Fuel column height	L	793	cm	[53]
Coolant channel mass flow rate	\dot{m}	0.0176	kg/s	[53]
Average power density	q_{ave}	35	W/cm^3	[53]
Inlet coolant temperature	T_{in}	400	°C	[53]
Helium inlet pressure	P	70	bar	[53]
Helium density	ρ	4.94×10^{-6}	kg/cm^3	[91]
Helium heat capacity	c_p	5188	J/kg/K	[91]
Calculated parameters				
Coolant film radius	R_i	0.8050	cm	-
Coolant average velocity	v_c	1794.33	cm/s	-
Film thermal conductivity	k_i	1.731×10^{-3}	$\text{W}/\text{cm}/\text{K}$	-

Figure 5.4 shows the temperature profiles. The axial temperatures increase from the top to the bottom of the reactor. The moderator and coolant temperatures are parallel as the model assumes a film thermal conductivity independent of the temperature. The fuel and moderator temperature difference decreases. As the thermal conductivities of the different materials increase with temperature, the thermal resistance between the moderator

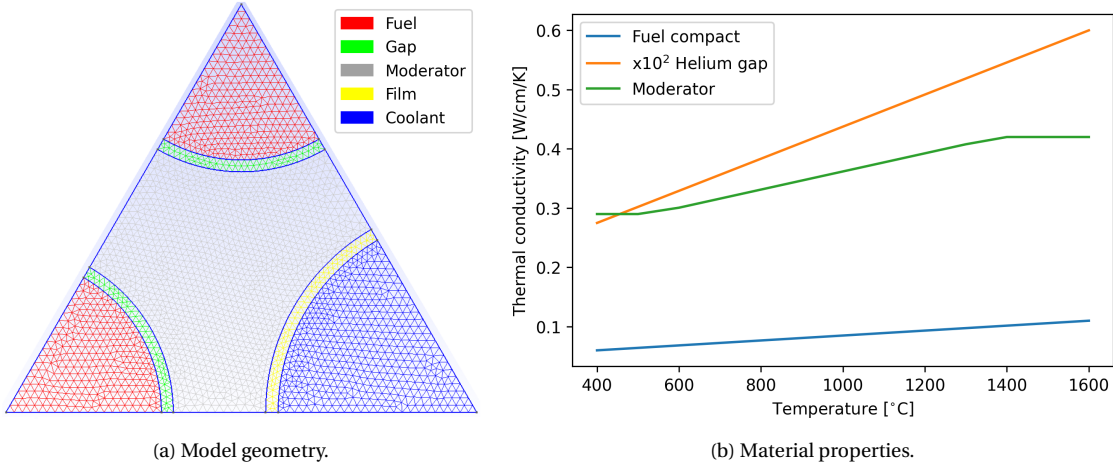


Figure 5.3: Moltres/MOOSE input parameters.

and the fuel decreases. Table 5.3 summarizes the results. Moltres/MOOSE coolant temperature is smaller by 4°C. The moderator temperature is larger by 9°C. The fuel temperature is larger by 22°C. The cause of the fuel temperature discrepancy is the power profile simplification. For a sinusoidal power profile the fuel-to-coolant temperature difference is small in the outlet, as we have seen in the previous section. The opposite extreme scenario is the uniform power profile, where the fuel-to-coolant temperature difference is larger. In et al. used a chopped cosine power profile. This is the case in between a uniform and a sinusoidal power profile. Hence, our model yields a larger fuel-to-coolant temperature at the outlet. Overall, our model results showed good agreement with In et al. results.

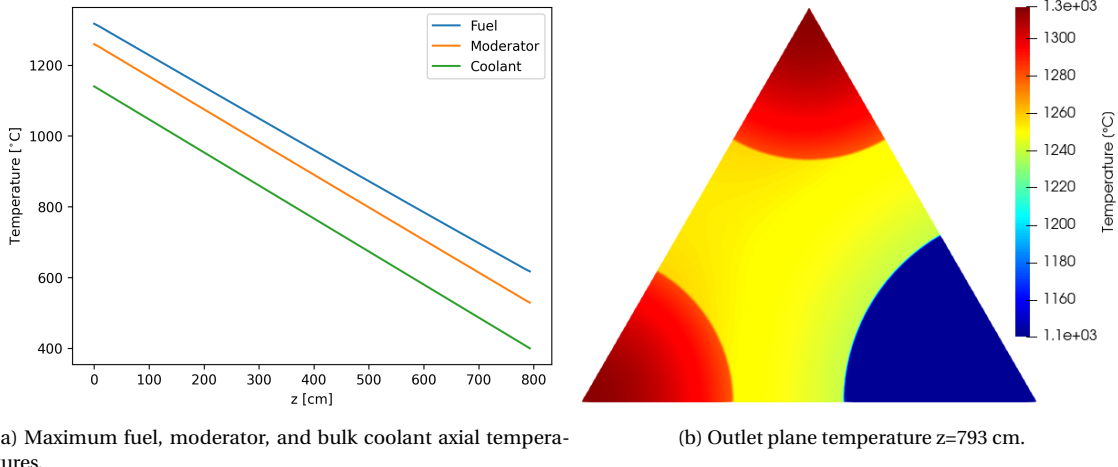


Figure 5.4: Temperature profiles.

Table 5.3: Comparison between In et al. and Moltres/MOOSE results.

Parameter	In et al.	Moltres/MOOSE
Maximum coolant temperature [°C]	1144	1140
Maximum moderator temperature [°C]	1250	1259
Maximum fuel temperature [°C]	1295	1317

5.2 Fuel column

This section solved an HTGR fuel column. It aimed to reproduce some of the analyses in Sato et al. 2010 [107] in an effort to validate the fuel column model. We chose this article as it gives a thorough description of the problem making it easier to reproduce. First, we analyzed a column with no bypass-gap. Second, we studied a column with a 3mm-gap.

The study used the GT-MHR as the reference reactor for the calculations. Figure 5.5a exhibits the model geometry. The model included only a one-twelfth portion of the column due to symmetry. The GT-MHR shares the geometry dimensions with the MHTGR, which Table 3.2 specifies.

Equation 5.1 evaluates the solid material properties [60]. Table 5.5 displays the fuel compact and moderator thermal conductivities coefficients. Table 5.4 lists the helium properties and several input parameters. Figure 5.5b shows the temperature dependent material properties.

$$\phi(T) = A_1 + A_2 T + A_3 T^2 + A_4 T^3 + A_5 T^4 \quad (5.1)$$

The model assigns a number to each coolant channel and the bypass-gap, see Figure 5.5a. In this exercise, we use the mass flow distribution from Sato et al. Table 5.6 shows the mass flow rate in each channel.

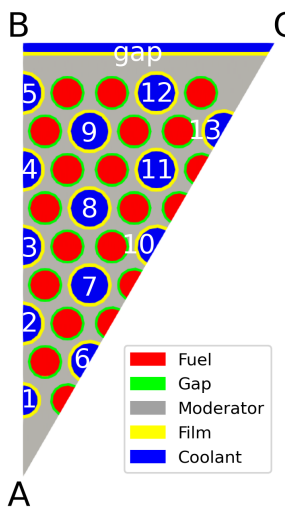
Table 5.4: Problem characteristics.

Parameter	Symbol	Value	Units	Reference
Inlet coolant temperature	T_{in}	490	°C	[107]
Helium inlet pressure	P	70	bar	[107]
Helium density	ρ	4.37×10^{-6}	kg/cm ³	[91]
Helium heat capacity	c_p	5188	J/kg/K	[91]
Average power density	q_{ave}	27.88	W/cm ³	[107]
<hr/>				
Calculated parameters				
Coolant film radius	R_i	0.804	cm	-
Film thermal conductivity	k_i	2.09×10^{-3}	W/cm/K	-

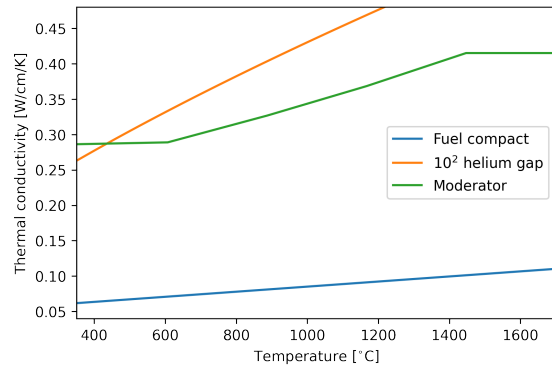
Table 5.7 compares Moltres/MOOSE results to Sato's results. In the no gap case, Moltres/MOOSE's maxi-

Table 5.5: Thermal conductivity coefficients.

Temperature range [K]	Moderator			Fuel compact
	255.6-816	816-1644.4	1644.4-1922.2	255.6-2200
A1	28.6	1.24E+2	41.5	3.94
A2	-	-3.32E-1	-	3.59E-3
A3	-	4.09E-4	-	-1.98E-9
A4	-	-2.11E-7	-	3.19E-12
A5	-	4.02E-11	-	-9.77E-16



(a) Model geometry.



(b) Material properties.

Table 5.6: Mass flow rate [g/s]. Values form [107].

Channel	1	2	3	4	5	6	7
No gap	6.18	11.34	11.37	11.38	11.43	11.33	22.70
3mm gap	5.88	10.80	10.85	10.91	11.08	10.80	21.58
Channel	8	9	10	11	12	13	Gap
No gap	22.73	22.73	11.38	22.77	22.91	11.44	-
3mm gap	21.67	21.83	10.88	21.81	22.20	11.10	16.56

mum coolant temperature is 2 °C lower and the maximum fuel temperature is 4°C higher. In the 3mm-gap case, Moltres/MOOSE's maximum coolant temperature is 2 °C lower and the maximum fuel temperature is 1°C lower. The results showed good agreement.

Figure 5.5 displays the outlet temperature along lines A-B and A-C from Figure 5.5a. The temperature is higher closer to the column center. The bypass-flow causes the temperature in the center to rise while reducing the peripheral temperature. The presence of the gap produces a larger temperature gradient in the assembly.

Table 5.7: Maximum temperatures.

	No gap		3mm gap	
	Sato et al.	Moltres/MOOSE	Sato et al.	Moltres/MOOSE
Bulk coolant	985	983	1007	1005
Fuel	1090	1094	1115	1114

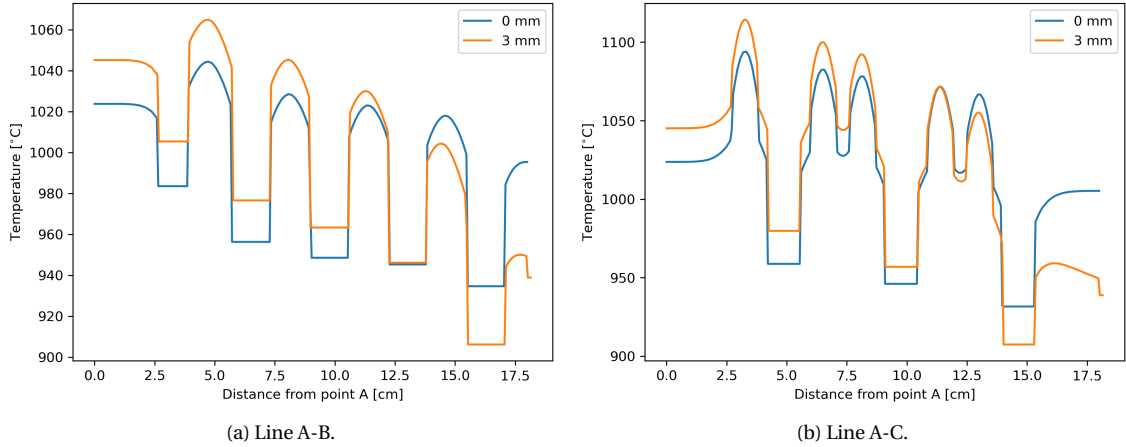


Figure 5.5: Outlet plane temperature along the line A-B and line A-C.

5.2.1 Flow distribution analysis

As described in Section 2.2, several authors calculate the flow distribution using various methods. This section compares the effects of different methods on the results. To carry out such comparison, the chosen metrics are the maximum coolant and fuel temperatures and the mass flow distribution. The model assigns a number to each coolant channel and the bypass-gap, see Figure 5.5a. Note that channel 1 is a small coolant channel while channels 2 to 13 are large coolant channels.

We analyzed the following cases:

- Case 1: uses the mass flow distribution from Sato et al.

- Case 2: uses a flat velocity profile (every channel and gap have the same velocity).
- Case 3: uses the incompressible flow model with a temperature independent helium viscosity.
- Case 4: uses the incompressible flow model with a temperature dependent helium viscosity.
- Case 5: uses the low-Mach number model with a temperature dependent helium viscosity.

To calculate the different flow distributions, we used the following equations. Equation 5.2 calculated the flow distribution in case 1. Equation 5.3 [84] calculated the pressure drop in cases 3 and 4. Case 4 differs from case 3 as the friction factor f depends on the average channel temperature. Equation 5.4 [84] calculated the pressure drop in case 5. For cases 3 to 5, the pressure drop is proportional to the channel mass flow, equation 5.5. Equations 5.3 and 5.4 calculated B_i . Equations 5.6 and 5.7 [84] solved the mass flow distribution iteratively. As cases 4 and 5 mass flow distributions depend on the temperature, the calculations required another level of iterations to obtain the final mass flow distribution. The convergence criteria was 1°C for the maximum coolant and fuel temperatures.

$$\dot{m}_i = \frac{A_i}{\sum_j A_j} \quad (5.2)$$

$$\Delta P = \frac{1}{\rho} \left(\frac{\dot{m}_i}{A_i} \right)^2 f \frac{2L}{D_h} \quad (5.3)$$

$$\Delta P = \frac{\dot{m}_i^2}{2\rho A_i^2} \left[\frac{4fL(T_i + T_o)}{2DT_i} + \frac{T_o - T_i}{T_i} \right] \quad (5.4)$$

$$\Delta P = B_i \dot{m}_i^2 \quad (5.5)$$

$$\Delta P = \left(\frac{\dot{m}_T}{\sum_i \frac{1}{\sqrt{B_i}}} \right)^2 \quad (5.6)$$

$$\dot{m}_i = \sqrt{\Delta P / B_i} \quad (5.7)$$

where

$$\dot{m}_i = \text{channel } i \text{ mass flow rate}$$

$$A_i = \text{channel } i \text{ cross-sectional area}$$

$$\Delta P = \text{pressure drop}$$

$$T_i = \text{channel inlet coolant temperature}$$

$$T_o = \text{channel outlet coolant temperature}$$

$$\dot{m}_T = \text{total mass flow rate}$$

(5.8)

Table 5.8 displays the results for the mass flow rates. Case 2 yields the largest small coolant channel mass flow, and the smallest large coolant channel mass flow. Case 3 and 4 barely differ. Not taking into account the temperature dependency of the viscosity yields a simpler method and the accuracy loss is negligible. Case 5 arrives to the closest values to the reference solution.

Table 5.9 summarizes the maximum temperatures. For the maximum coolant temperature, case 2 yields the largest difference which is less than 10°C. Case 5 yields the closest results to the reference values. For the maximum fuel temperature, case 2 and 5 yield the best results. Again, case 3 and 4 barely differ.

The low-Mach number model yielded the closest results to the reference solution. However, such method required two levels of an iterative solver. From a computational point of view, case 2 model is the simplest method as it does not require an iterative solver. Additionally, case 2 model yields the simplest Moltres input file. For these reasons, the rest of the thesis uses case 2 model for the fluid flow distribution.

Table 5.8: Mass flow rates [g/s].

Channel	1	2	3	4	5	6	7
Case 1	5.88	10.80	10.85	10.91	11.08	10.80	21.58
Case 2	6.66	10.41	10.41	10.41	10.41	10.41	20.82
Case 3	5.98	10.91	10.91	10.91	10.91	10.91	21.82
Case 4	5.97	10.90	10.90	10.91	10.92	10.90	21.80
Case 5	5.83	10.75	10.81	10.90	11.09	10.73	21.58
Channel	8	9	10	11	12	13	Half-gap
Case 1	21.67	21.83	10.88	21.81	22.20	11.10	8.28
Case 2	20.82	20.82	10.41	20.82	20.82	10.41	8.20
Case 3	21.82	21.82	10.91	21.82	21.82	10.91	8.55
Case 4	21.81	21.83	10.91	21.82	21.85	10.92	8.55
Case 5	21.71	21.92	10.84	21.87	22.26	11.08	8.63

Table 5.9: Comparison of the maximum temperatures that the different cases yield.

	Case 1	Case 2	Case 3	Case 4	Case 5
Coolant	1005	994	999	1000	1007
Fuel	1114	1116	1109	1110	1116

5.3 Mesh convergence analysis

The remainder of this Chapter intends to solve the full-core problem. This section aims to identify some possible problems introduced by the large mesh size requirement of the full-core problem. This section conducts a mesh convergence analysis of the full-fuel column problem. Figure 5.6 displays the model geometry. Table 5.10 presents the results. The convergence criteria was 1°C for the maximum coolant and fuel temperatures. The coolant temperature converged for the fifth mesh. The fuel temperature did not reach convergence. Further refinement of the mesh was not possible as the simulation memory requirements were too high.

This analysis reveals a potential problem. The high level of detail in our geometry requires a large number of elements in the mesh. Moving forward, the problem dimensions will increase and the number of elements in the mesh will do so too. Potentially, this method will not be able to solve the three-dimensional full scale problem due to a high memory requirement. For this reason, the next section intends to solve the full scale problem using a two-dimensional cylindrical model.

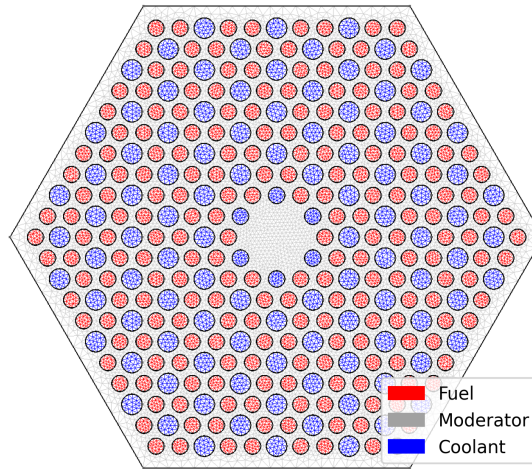


Figure 5.6: Full fuel column model geometry.

Table 5.10: Maximum temperatures.

	Mesh 1	Mesh 2	Mesh 3	Mesh 4	Mesh 5
Number of elements [$\times 10^6$]	1.025	1.306	1.833	2.596	3.006
Number of DoFs [$\times 10^6$]	0.524	0.666	0.932	1.317	1.525
Maximum coolant temperature	1060.41	1062.23	1064.00	1065.13	1065.32
Maximum fuel temperature	1204.49	1217.32	1225.57	1233.44	1234.93

5.4 OECD/NEA MHTGR-350 MW Benchmark: Phase I Exercise 2

This section conducted Phase I Exercise 2 of the benchmark with Moltres/MOOSE. Phase I Exercise 2 defines a thermal-fluids standalone calculation. The exercise purpose is to ensure that the thermal-fluid model differences between participants are negligible and that they will not affect the coupled exercises. The benchmark specifies the power density of each fuel region and defines the mass flow distribution and material properties for four sub-cases:

- Exercise 2a: No bypass flow and fixed thermophysical properties. The model does not account for the bypass flow and the thermo-physical properties are constant.
- Exercise 2b: Bypass flow type I and fixed thermophysical properties. This exercise prescribes the bypass flow distribution and the thermo-physical properties are constant.
- Exercise 2c: Bypass flow type I and variable thermophysical properties. This exercise prescribes the bypass flow distribution and the thermo-physical properties depend on different simulation parameters.
- Exercise 2d: Bypass flow type II and variable thermophysical properties. This exercise solves the bypass flow distribution through the explicit modeling of the bypass gaps. The thermo-physical properties depend on different simulation parameters.

The exercise requires the reporting of the average and maximum values of the reflector, Reactor Pressure Vessel (RPV), fuel, moderator, and coolant temperatures. It also requires the reporting of the RPV heat flux and the mass flow rate distribution in the coolant channels and the bypass gaps. This data is helpful to trace the source of possible differences in the primary parameters between participants. OECD/NEA did not publish this exercise's results. This section compares Moltres/MOOSE results to INL's benchmark results [114], and presents only a subset of available data that illustrate the main characteristics of the exercise.

Figure 5.7 displays the model geometry. To simplify the simulation of the exercise, the model uses several simplifications. In the axial direction, it does not consider the upper plenum and the outlet plenum. The axial boundaries are the upper face of the top reflector and the lower face of the bottom reflector. The upper face of the top reflector and the inlet coolant flow are at 259 °C. The lower face of the bottom reflector is adiabatic. The outlet

coolant uses an outflow boundary condition. In the radial direction, the model does not consider the core barrel and the helium gap. After the outer reflector comes the RPV and after it the outside air. The outer boundary of the air region is at 30 °C.

The core model geometry uses INL's model as the reference design. Nine rings define the core solid structures and other nine rings the coolant flow in the core. We calculated the rings radii by preserving the assemblies volume. The coolant thickness is constant for all the rings and preserves the coolant volume in the core. Table 5.11 presents the material properties. All the graphite regions assume the grade H-451 graphite material properties.

Table 5.12 displays some of the results. Our model considerably under-predicts the inner reflector rings temperature, while it over-predicts the coolant rings temperature. With the purpose of better understanding this behavior, Figure 5.8 shows the temperature across the reactor on the bottom of the active core ($z=200$ cm). This figure exposes that the temperatures in the core are well above the other region temperatures. Although such a behavior is normal, the temperature profile reveals some heat transfer disconnection between the different rings. In other words, the heat transfer from the fuel rings to the rest of the core structures seems to be small compared to the heat transfer to the coolant rings. For that reason, the reflector temperatures are too low and the coolant temperatures are too high. These results indicate that Moltres model fails to capture some heat transfer mechanism that INL's model captures. The most notorious difference between the models is the inclusion of the radiative heat transfer. Future works will focus on confirming this supposition and also on adding the capability to model the radiative heat transfer.

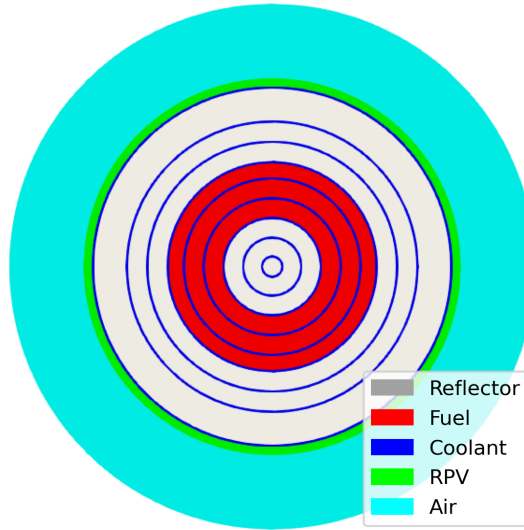


Figure 5.7: Model geometry.

To circumvent this barrier, we developed a second model based on Stainsby's approach [111]. The calculation

Table 5.11: Problem characteristics.

Parameter	Value	Units	Reference
Fuel compact thermal conductivity	20	W/m/K	[88]
Fuel block thermal conductivity	37	W/m/K	[88]
Graphite thermal conductivity	66	W/m/K	[88]
RPV thermal conductivity	40	W/m/K	[88]
Coolant thermal conductivity	0.41	W/m/K	[88]
Air thermal conductivity	0.068	W/m/K	[88]
Helium density	5.703×10^{-6} kg/cm ³		[91]
Helium heat capacity	5188	J/kg/K	[91]

Table 5.12: First bottom core level average temperatures.

	Reflector			Coolant		
	Ring 1	Ring 2	Ring 3	Ring 4	Ring 5	Ring 6
INL	790	794	802	797	636	673
Moltres/MOOSE	268	313	769	1424	1597	1157

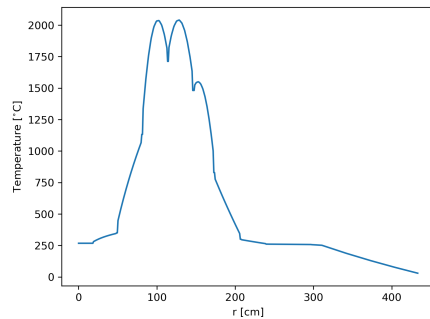


Figure 5.8: Model geometry.

uses a global model to obtain the coolant temperature in the core and then it uses a sub-channel model to obtain the fuel and moderator average temperature. Figure 5.9 displays the global model geometry. The sub-channel model uses half of the unit cell in Section 5.1.2. The global model uses three rings to define the core solid structures and other three for the coolant flow in the core. We calculated the rings radii by preserving the assemblies volume. The middle ring defines the fuel rings, which encompasses three fuel rings (see Figure [88]). The coolant ring volumes preserve the coolant volume in each of the fuel rings. The model uses the material properties from Table 5.11.

Figure 5.10 presents the coolant and solid temperatures in the different fuel rings. The coolant temperature increases from the top to the bottom of the core. The temperature is constant in the bottom and top reflector regions, and it increases in the active core region. The highest coolant, fuel, and moderator temperatures are in fuel ring 1.

Table 5.13 compares Moltres/MOOSE results to INL's. We focus on the coolant temperature of the different rings. Moltres predicts a smaller temperature in fuel ring 1 while it predicts higher temperatures in fuel rings 2 and 3. For some reason, the global model fails to distribute properly the heat produced in the fuel rings into the coolant rings. A possible cause of this discrepancy is the flat velocity approximation. Section 5.2.1 showed that a flat velocity distribution of the coolant is reasonable in the fuel column model. However, one of the assumptions of that model was that the power density is uniform. In this exercise, the power density is not uniform, and that could be causing the discrepancies. Further studies will study the cause of the discrepancies.

Additionally, Moltres predicts a smaller coolant-to-moderator temperature difference for fuel rings 1 and 2. The largest discrepancy is in fuel ring 1. INL's model coolant-to-moderator temperature difference is 46°C while Moltres/MOOSE predicts a difference of 30°C. The flat velocity approximation might be again the source of these discrepancies. Finally, The moderator-to-fuel temperature difference from INL and Moltres/MOOSE are close. In fuel ring 1, it is 20°C and 22°C for INL and Moltres/MOOSE results, respectively. In fuel ring 2, the difference is 16°C and 17°C for INL and Moltres/MOOSE results, respectively.

Table 5.13: First bottom core level average temperatures.

	Fuel ring 1		fuel ring 2		fuel ring 3	
	INL	Moltres/MOOSE	INL	Moltres/MOOSE	INL	Moltres/MOOSE
Coolant	797	718	636	646	673	696
Moderator	843	748	672	669	Not shown	721
Fuel	863	770	688	686	722	739

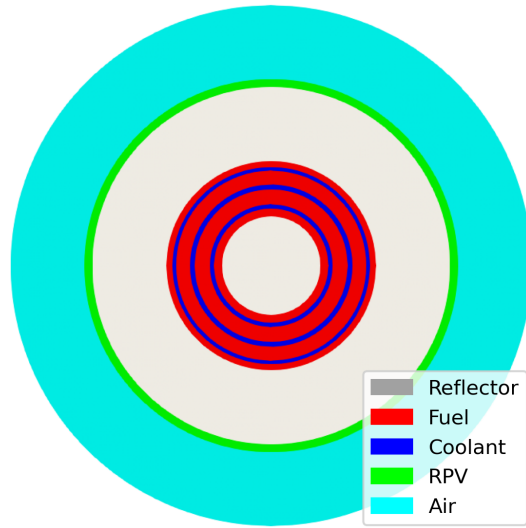


Figure 5.9: Model geometry.

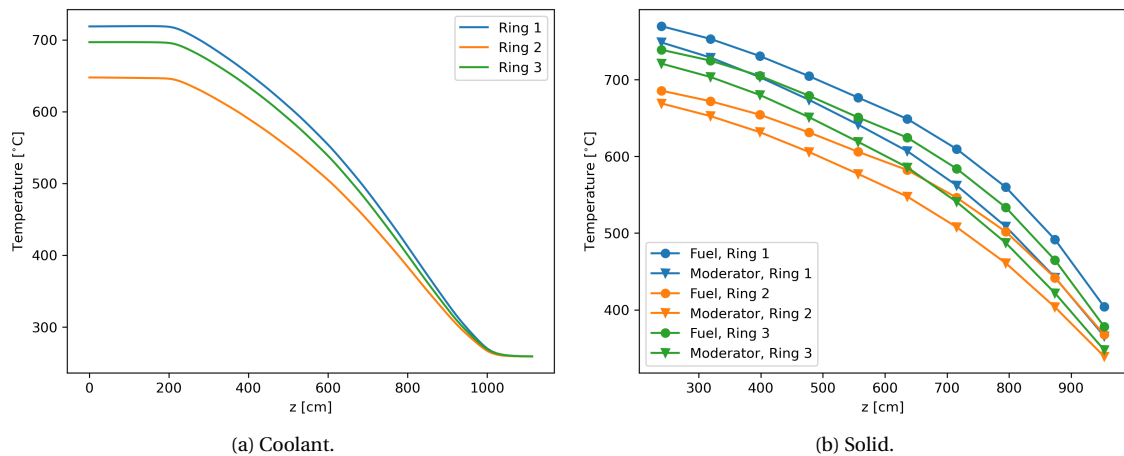


Figure 5.10: Axial temperatures.

5.5 OECD/NEA MHTGR-350 MW Benchmark: Phase I Exercise 3

This section sets the road-map for conducting Phase I Exercise 3 of the benchmark with Moltres/MOOSE. Exercise 3 combines all the data from the first two exercises, and the participants need to determine a coupled neutronic and thermal-fluids solution. The benchmark specifies the group constants required to conduct the exercise. The group constants depend on four state parameters: moderator and fuel temperature and xenon-135 and hydrogen concentration. In addition to this data, the benchmark provides fluence maps to determine the thermal conductivity of graphite.

Two sub-cases compose Exercise 3:

- Exercise 3a: It uses the same thermal-fluids problem definition from Exercise 2c.
- Exercise 3b: It uses the same thermal-fluids problem definition from Exercise 2d.

This exercise requires the reporting of the same parameters reported in Exercises 1 and 2 combined.

Follow [59]. 'The initial coupling model was unable to correctly calculate the thermal coefficient in the fuel because it did not take into account the difference between the moderator and the fissile isotopes temperatures. One of the major improvements of the coupling model is a de-homogenization calculation which guarantees a better description of the local thermal calculation in the fuel.' [25].

5.6 Conclusions

The preliminary studies focused on the verification of the thermal-fluids model and the validation of the unit-cell model. The verification of the thermal-fluids model studied a simplified cylindrical model comparing the Moltres/MOOSE numerical solution to the problem analytical solution. Both solutions were in agreement. This study set the basis for the unit cell problem set-up. The unit cell problem use thermal-fluids model from the previous verification. In an effort to validate the unit cell model, Section 5.1.2 compared Moltres/MOOSE results to In et al. [53]. The results present some discrepancies. The outlet coolant and moderator temperatures differ by less than 10°C while the fuel temperature differs by 22°C. We expected some variability in the results as some of our simulation parameters may differ from the original study. In's article is missing the materials definition and Section 5.1.2 adopted the material properties from Tak et al. [118]. Additionally, In uses a chopped cosine power profile and Section 5.1.2 model simplifies the calculation using a uniform power density.

The following section's focus of analysis was a one-twelfth section of an HTGR fuel column. In an effort to validate the model, Section 5.2 intended to reproduce some of Sato et al. [107] results. Section 5.2 conducted two studies: one with no bypass-gap, and one with a 3mm-bypass-gap. To simplify the analysis, our model adopted

the coolant channel mass flow rates from Sato's article. For both case studies, the maximum temperatures in the coolant and the fuel showed good agreement. Section 5.2 also presented the temperature profile in two of the edges of the geometry. Such analysis exhibits the effects of the bypass flow on the temperature. The presence of the gap makes the center temperature rise while it reduces the peripheral temperature. The overall consequence is an increase in the temperature gradient inside the column.

The next analysis studied different mass flow distribution in the coolant channels and bypass-gap of the fuel column. Section 5.2.1 adopted Sato's mass flow distribution as the reference value and calculated the mass flow distribution using four different methods. From case 2 to case 5, the complexity of the methods increases as some of the them require iterative solvers. Overall, case 2 proved to be the simplest method and its application does not considerably deteriorate the results' accuracy. For that reason, the following studies adopted case 2 mass flow distribution method.

Keeping in mind that the ultimate objective of this work is to conduct full-scale simulations, Section 5.3 studied the feasibility of extending this methodology to larger meshes. Section 5.3 conducted a mesh convergence analysis on the full-fuel column problem. As the model uses the one-dimensional coolant equations, the coolant temperature converges relatively fast compared to the fuel temperature. The fuel temperature did not reach convergence in this analysis as the increase in the mesh discretization imposed a high memory requirement on the simulations. This analysis concluded that modeling the thermal-fluids with such a level of detail is computationally too expensive, and it suggests searching for other methods. The following sections adopted a two-dimensional cylindrical model for the full-core analyses.

Section 5.4 described Phase I Exercise 2 of the OECD/NEA MHTGR-350 MW Benchmark. This exercise encompasses four sub-cases with different definitions of bypass-flow and material properties. The simplest exercise is *2a*, as it does not model the bypass flow and provides the definition of the material properties. Section 5.4 used Moltres/MOOSE to conduct it. As OECD/NEA did not publish this exercise's results, Section 5.4 compared Moltres/MOOSE results to INL results [114]. Additionally, this thermal-fluids model bases its definition on INL's model. However, the large discrepancies between Moltres/MOOSE results suggest that our model does not capture some heat transfer mechanism that INL model does. One of the known differences between the models is the inclusion of the radiative heat transfer mechanism. As Moltres does not model that mechanism, it could be the cause of the differences. To circumvent this drawback, Section 5.4 used a global and a unit cell model based on Stainsby's approach [111]. The global model is responsible for calculating the coolant temperature while the unit cell model focuses on the moderator and fuel temperatures. With this approach, Moltres/MOOSE results were closer to INL results. The results showed some discrepancies which indicates that some assumption/model simplification is not accurate enough. A flat velocity approximation might be the cause of such discrepancies. Further studies

should analyze the origin of the discrepancies.

Chapter 6

Hydrogen Production

6.1 Introduction

Energy is one of the most vital contributors to economic growth. In the future, economies and populations will continue to expand, and their energy demand will accompany such change [16] [34]. Meeting these future needs requires the development of clean energy sources to ease the increasing environmental concerns. As seen in Figure 6.1, electricity generation was one of the economic sectors that released the most greenhouse gases (GHGs) in the US in 2017. As carbon dioxide (CO_2) is the main component in GHGs, decarbonizing electricity generation will allow us to meet the increases in energy demand and address the environmental concerns simultaneously.

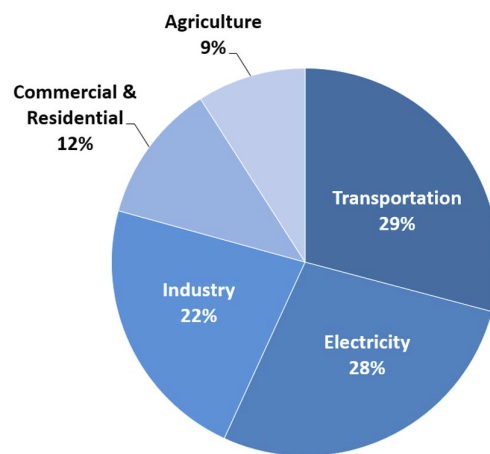


Figure 6.1: Total US GHG emissions by economic sector in 2017. Image reproduced from [36].

To address these concerns, utility companies are relying more and more on renewable energy resources, such as wind and solar [85]. However, high solar adoption creates a challenge. The need for electricity generators to quickly ramp up increases when the sun sets and the contribution from the photovoltaics (PV) falls [95]. The "duck curve" (or duck chart) in Figure 6.2 depicts this phenomenon. The California ISO (CAISO) developed the duck curve to illustrate the grid's net load [12]. We define the net load as the difference between the forecasted load and expected electricity production from solar.

Moreover, the duck curve reveals another issue. Over-generation may occur during the middle of the day, and high-levels of non-dispatchable generation may exacerbate the situation. As a consequence, the market would experience sustained zero or negative prices during the middle of the operating day [12].

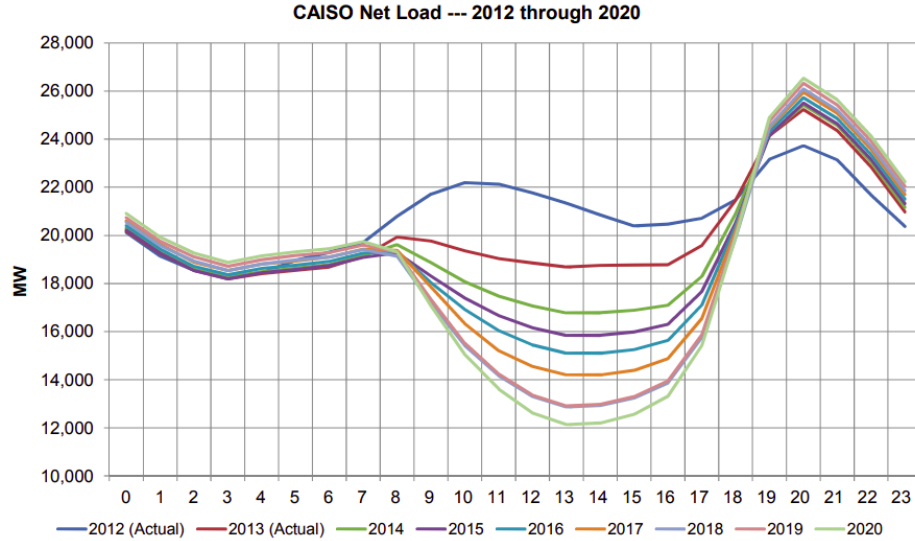


Figure 6.2: The duck curve. Image reproduced from [12].

The simplest solution to a demand ramp-up is to increase dispatchable generation, which uses resources with fast ramping and fast starting capabilities such as natural gas and coal [12], consequently decreasing non-dispatchable generation, such as geothermal, nuclear, and hydro. Nonetheless, an approach like this is inconsistent with the goal of reducing carbon emissions. Hence, our focus drifts to other potential low-carbon solutions, like nuclear generation and electricity storage through hydrogen (H_2) production.

Unfortunately, a carbon-neutral electric grid will be insufficient to halt climate change because transportation is a significant contributor to GHG emissions. As seen in Figure 6.1, transportation released the most GHGs in the US in 2017. Thus, decarbonizing transportation underpins global carbon reduction. One possible strategy is to develop a hydrogen economy, as Japan is currently doing. Japan's strategy rests on the firm belief that H_2 can be a decisive response to its energy and climate challenges. It could foster deep decarbonization of the transport, power, industry, and residential sectors while strengthening energy security [86]. In the transportation sector, Japan plans to deploy fuel cell vehicles, trucks, buses, trains, and ships. Although H_2 technologies release zero CO_2 , any H_2 production method is only as carbon-free as the energy source it relies on (electric, heat, or both). Nuclear reactors introduce a clean energy option to manufacture H_2 .

The University of Illinois at Urbana-Champaign (UIUC) is leading by example and actively working to reduce GHG emissions from electricity generation and transportation (among other sectors) on its campus. In pursuance of those efforts, the university has developed the Illinois Climate Action Plan (iCAP).

6.2 Illinois Climate Action Plan

In 2008, UIUC signed the American College and University Presidents' Climate Commitment, formally committing to becoming carbon neutral as soon as possible, no later than 2050. The university developed the iCAP in 2010 as a comprehensive roadmap toward a sustainable campus environment [97]. The iCAP defines a list of goals, objectives, and potential strategies for six topical areas.

- Energy Conservation and Building Standards:

Focuses on maintaining or reducing campus gross square footage, strengthening conservation efforts, and engaging the campus community in energy conservation.

- Energy Generation, Purchasing, and Distribution:

Explores 100% clean campus energy options. This includes expanding on-campus solar energy production, extending the purchase of clean energy from low-carbon energy sources, and offsetting all emissions from the National Petascale Computing Facility.

- Transportation:

Comprises the efforts to reduce air travel emissions, reduce Urbana-Champaign campus fleet emissions, and study scenarios for the complete conversion of the campus fleet to renewable fuels.

- Water and Stormwater:

Focuses on improving the water efficiency of cooling towers, performing a water audit to establish water conservation targets, determining upper limits for water demand by end-use, and implementing projects to showcase the potential of water and stormwater reuse.

- Purchasing, Waste, and Recycling:

Attempts to standardize purchasing office paper, cleaning products, computers, and other electronics as well as freight delivery services. It also attempts to facilitate recycling by reducing non-durable goods purchases and reducing municipal solid waste going to landfills.

- Agriculture, Land Use, Food, and Sequestration:

Will perform a comprehensive assessment of GHG emissions from agricultural operations, develop a plan to reduce these emissions, implement a project that examines the foodservice carbon footprint for Dining, and increase carbon sequestration in campus soils.

6.3 Objectives

As mentioned earlier, we place our attention on two areas: electricity generation and transportation. We will turn our attention to electricity generation and transportation on the UIUC campus. Consequently, this work's objective aligns with the efforts in two of the six target areas defined on the iCAP.

Regarding electricity generation, our analysis focuses on the UIUC grid. The present work quantifies the magnitude of the duck curve in such a grid. To mitigate the risk of over-generation, we propose to use the over-generated energy to manufacture H₂. We chose a nuclear reactor to be the primary source of energy. The next step is to quantify how much H₂ different production methods can produce. Section 6.4 discusses a few hydrogen production methods considered for our analysis. Finally, we will calculate how much electricity we would generate using the H₂ produced.

Regarding transportation, we study the conversion of the UIUC fleet on campus to Fuel Cell Electric Vehicles (FCEVs). Additionally, the analysis includes the conversion of the Champaign-Urbana Mass Transit District (MTD) fleet as well. The first step is to determine the fuel consumed by both fleets and how much H₂ enables the fleets' complete conversion. Finally, we consider a few reactor designs and analyze which of them could produce enough H₂ to fulfill both fleet requirements.

Both studies propose the same solution - a nuclear reactor coupled to a hydrogen plant. In terms of electricity generation, this solution will decrease the need for dispatchable sources and, consequently, reduce carbon emissions. In terms of transportation, it will eliminate carbon emissions.

In both analyses, many reactor choices can satisfy our needs. The typical UIUC's grid demand is smaller than 80 MW [30]. Accordingly, we consider reactors of small capacities, such as microreactors and Small Modular Reactors (SMRs). Section 6.5 discusses their characteristics.

6.4 Hydrogen production methods

This section introduces several hydrogen production processes and their energy requirements.

6.4.1 Electrolysis

The electrolysis of water is a well-known method whose commercial use began in 1890. This process produces approximately 4% of H₂ worldwide. The process is ecologically clean because it does not emit GHGs. However, in comparison with other methods, electrolysis is a highly energy-demanding technology [63].

Three electrolysis technologies exist. Alkaline-based is the most common, the most developed, and the lowest in capital cost. It has the lowest efficiency and, therefore, the highest electrical energy cost. Proton exchange

membrane electrolyzers are more efficient but more expensive than Alkaline electrolyzers. Solid Oxide Electrolysis Cells (SOEC) electrolyzers are the most electrically efficient but the least developed. SOEC technology has challenges with corrosion, seals, thermal cycling, and chrome migration [63]. The first two technologies work with liquid water and the latter requires high-temperature steam, so we will refer to the first two as Low-Temperature Electrolysis (LTE) and the latter as High-Temperature Electrolysis (HTE).

Water electrolysis converts electric and thermal energy into chemical energy stored in hydrogen. The process enthalpy change ΔH determines the required energy for the electrolysis reaction to take place. Part of the energy corresponds to electric energy ΔG and its rest to thermal energy $T \cdot \Delta S$, as in Equation 6.1.

$$\Delta H = \Delta G + T\Delta S \quad (6.1)$$

where

ΔH = Specific total energy [kWh/kg-H₂]

ΔG = Specific electrical energy [kWh/kg-H₂]

$T\Delta S$ = Specific thermal energy [kWh/kg-H₂].

In LTE, electricity generates the thermal energy. Hence, ΔH alone determines the process's required energy. ΔH is equal to 60 kWh/kg-H₂ considering a 67% electrical efficiency [126].

In HTE, a high-temperature heat source is necessary to provide thermal energy. ΔG decreases with increasing temperatures as seen in Figure 6.3. Decreasing the electricity requirement results in higher overall production efficiencies since heat-engine-based electrical work has a thermal efficiency of 50% or less [58]. Figure 6.3 shows ΔG and $T\Delta S$. We considered the SOEC's ΔG to have an electrical efficiency of 88% [46]. $T\Delta S$ accounts for the latent heat of water vaporization. Note that the process is at 3.5 MPa. ΔG increases with pressure. However, we chose a high pressure to save energy, as compressing liquid water is cheaper than compressing H₂ [99].

Finally, equations 6.2 and 6.3 determine the electrical P_{EH2} and thermal power P_{TH2} required by the hydrogen plant.

$$P_{EH2} = \dot{m}_{H2}\Delta G \quad (6.2)$$

$$P_{TH2} = \dot{m}_{H2}T\Delta S \quad (6.3)$$

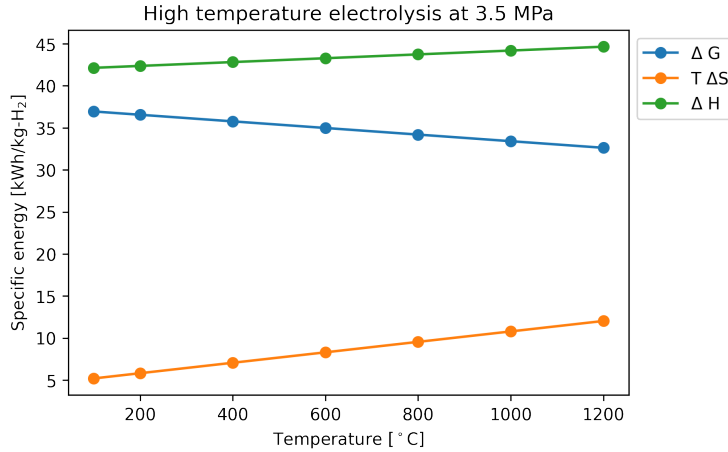


Figure 6.3: Energy required by HTE at 3.5 MPa.

where

$$P_{EH2} = \text{Total electrical power [kW]}$$

$$P_{TH2} = \text{Total thermal power [kW]}$$

$$\dot{m}_{H2} = \text{H}_2 \text{ production rate [kg/h].}$$

6.4.2 Sulfur-Iodine Thermochemical Cycle

Thermochemical water-splitting is converting water into hydrogen and oxygen by a series of thermally driven chemical reactions. The direct thermolysis of water requires temperatures above 2500 °C for significant hydrogen generation. At this temperature, the process can decompose a 10% of the water. A thermochemical water-splitting cycle accomplishes the same overall result using much lower temperatures.

General Atomics, Sandia National Laboratories, and the University of Kentucky compared 115 cycles that would use high-temperature heat from an advanced nuclear reactor [15]. The report specifies a set of screening criteria used to rate each cycle. Some of the cycles' desirable characteristics were minimal chemical reactions and separation steps, a high abundance of the elements, a minimal solids flow, and good compatibility between heat input temperature and the permitted materials high temperature. The highest scoring method was the Sulfur-Iodine (SI) cycle.

The SI cycle consists of the three chemical reactions represented in Figure 6.4. The whole process takes in water and high-temperature heat and releases hydrogen and oxygen. The process operates without any electricity. The process recycles all reagents and lacks effluents [133]. The chemical reactions are:

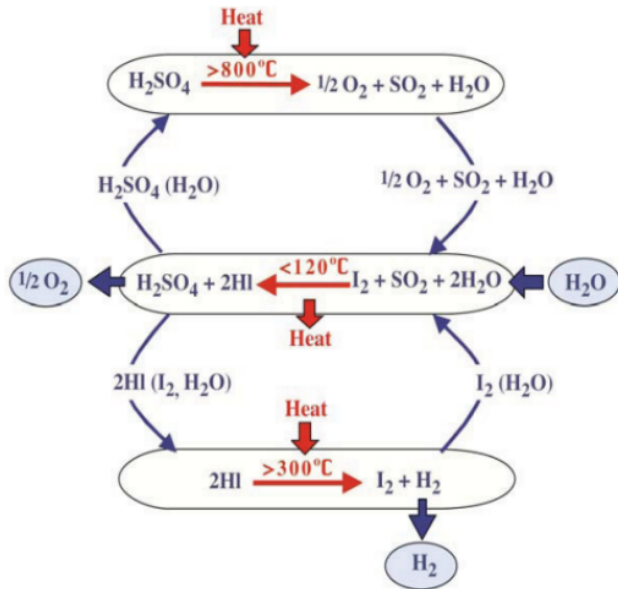


Figure 6.4: Diagram of the Sulfur-Iodine Thermochemical process. Image reproduced from [9].

Figure 6.5 presents the specific energy requirements of the cycle ΔH . Several sources disagree on the minimum temperature for the process to be viable. Our analysis considers the process feasible only for temperatures above $800^\circ C$. Finally, equation 6.7 determines the thermal power P_{TH2} required by the hydrogen plant.

$$P_{TH2} = \dot{m}_{H2}\Delta H \quad (6.7)$$

where

P_{TH2} = Total thermal power [kW]

\dot{m}_{H2} = H_2 production rate [kg/h]

ΔH = Specific energy [kWh/kg-H₂].

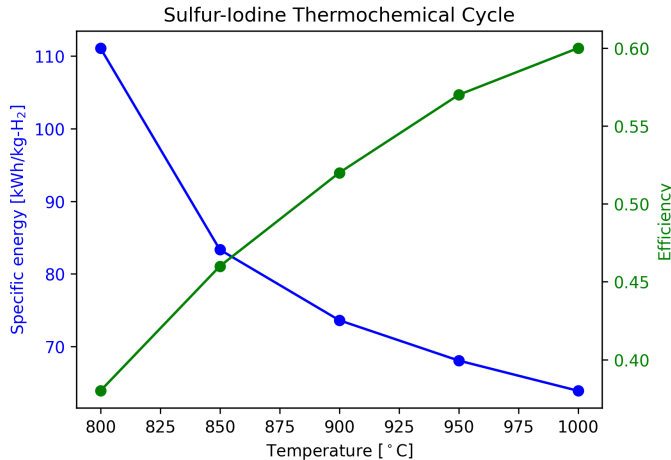


Figure 6.5: Energy required by the Sulfur-Iodine Thermochemical Cycle.

6.5 Microreactors and Small Modular Reactors

These reactor concepts share several features. The reactors require limited on-site preparation as their components are factory-fabricated and shipped out to the generation site. This feature reduces up-front capital costs, enables rapid deployment, and expedites start-up times. These reactors allow for black starts and islanding operation mode. They can start up from an utterly de-energized state without receiving power from the grid. They can also operate connected to the grid or independently. Moreover, these types of reactors are self-regulating, minimize electrical parts, and use passive safety systems to prevent overheating and safely shutdown.

Microreactors have the distinction that they are transportable. Small designs make it easy for vendors to ship the entire reactor by truck, shipping vessel, or railcar. These features make the technology appealing for a wide range of applications, such as deployment in remote residential locations and military bases.

The DOE defines a microreactor as a reactor that generates from 1 to 20 MWt [125]. The IAEA describes an SMR as a reactor whose power is under 300 MWe. It defines, as well, a 'very small modular reactor' as a reactor that produces less than 15 MWe [4]. As the definitions of these reactor concepts overlap, we will consider reactors of less than 100 MWt regardless of their specific classification.

6.6 Methodology

In this analysis, the energy source (electric and thermal) is a nuclear reactor with co-generation capabilities. The nuclear reactor supplies the grid with electricity P_E while providing a hydrogen plant with electricity P_{EH2} and thermal energy P_{TH2} , see the diagram in Figure 6.6. β and γ determine the distribution of the reactor thermal power P_{th} into P_E , P_{EH2} , and P_{TH2} , see Equations 6.8 to 6.10.

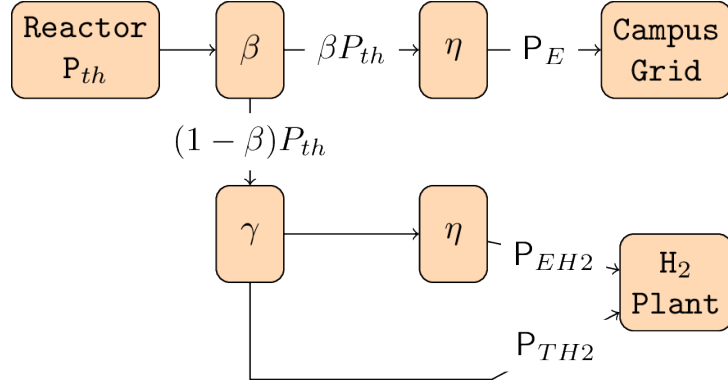


Figure 6.6: Diagram of a reactor coupled to a hydrogen plant.

$$P_E = \eta\beta P_{th} \quad (6.8)$$

$$P_{EH2} = \eta\gamma(1 - \beta)P_{th} \quad (6.9)$$

$$P_{TH2} = (1 - \gamma)(1 - \beta)P_{th} \quad (6.10)$$

where

η = thermal-to-electric conversion efficiency

$$\beta = \frac{P_E/\eta}{P_E/\eta + P_{TH2}/(1 - \gamma)}$$

$$\gamma = \frac{P_{EH2}/\eta}{P_{EH2}/\eta + P_{TH2}}.$$

If $\beta = 1$, the reactor only supplies the grid with electricity P_E and the hydrogen plant does not produce H_2 . If $\beta = 0$, the reactor only supplies the hydrogen plant and electricity does not go into the grid. Table 6.1 summarizes the values that γ takes for the various methods.

Method	γ	P_{EH2}	P_{TH2}
LTE	1	$\neq 0$	0
HTE	$0 < \gamma < 1$	$\neq 0$	$\neq 0$
SI	0	0	$\neq 0$

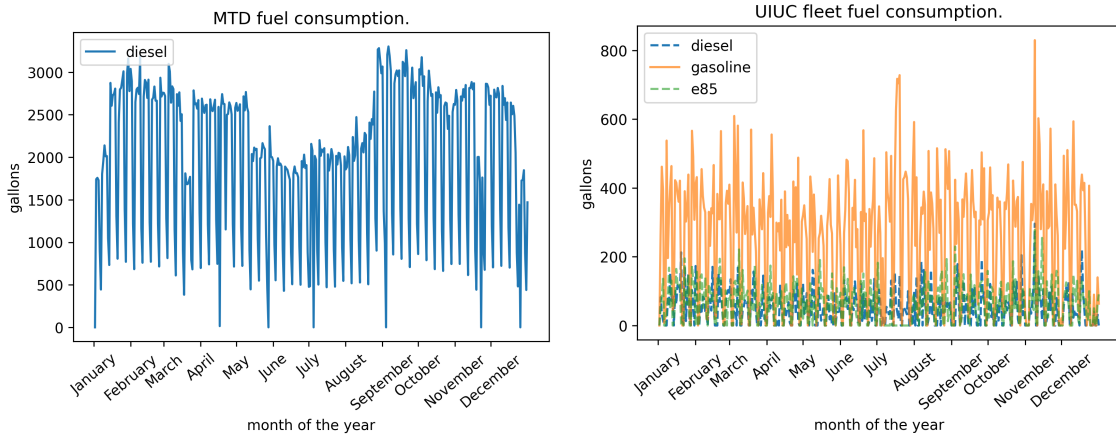
Table 6.1: Energy requirements of the different methods.

6.7 Results

This section holds the results of the multiple analyses.

6.7.1 Transportation

This subsection centers its focus on the transportation sector. Figure 6.7 displays the fuel consumed per day by MTD and UIUC fleet. Using the values shown in Table 6.2, we calculated the H₂ requirement for MTD and UIUC fleets, Figure 6.8. Table 6.3 summarizes the results.



(a) MTD fleet. Data go from July 1, 2018, until June 30, 2019 [29]. (b) UIUC fleet. Data go from January 1, 2019, until December 31, 2019 [128].

Figure 6.7: Fuel consumption data.

Table 6.2: H₂ necessary to replace a gallon of fuel [96] [20].

	Hydrogen Mass [kg]
Gasoline	1
Diesel	1.13
E85	0.78

Table 6.3: H₂ requirement for MTD and UIUC fleets.

Total [tonnes/year]	943
Average [kg/day]	2584
Average [kg/h]	108
Maximum in one day [kg]	4440

Using Table 6.4, we calculated the CO₂ savings caused by replacing all the fossil fuels with H₂. Table 6.5 displays the CO₂ savings for both fleets.

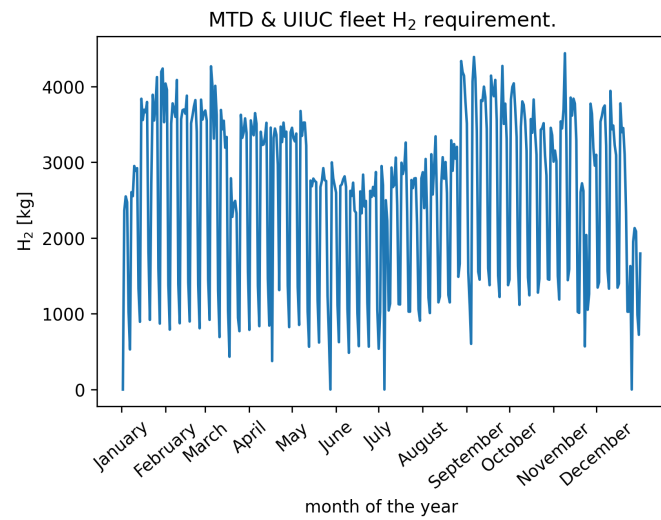


Figure 6.8: H₂ requirement for MTD and UIUC fleets.

Table 6.4: CO₂ savings in pounds per gallon of fuel burned [1].

	CO ₂ produced [lbs/gallon]
Gasoline	19.64
Diesel	22.38
E85	13.76

Table 6.5: CO₂ yearly savings.

	CO ₂ mass [tonnes/year]
MTD	7306
UIUC	1143
Total	8449

We have determined the H₂ requirement by the fleets, and now we seek a microreactor design capable of meeting such demand. For our analysis, we chose a few microreactor designs summarized in Table 6.6. Further studies could include other designs as well.

Figure 6.9 shows the hourly production rates for the different reactors and H₂ production processes. The figure includes a continuous line that represents the hydrogen requirement of both fleets. Note that the SI process's required high temperatures allow for the coupling with only one microreactor design, which has an outlet temperature of more than 800°C.

Table 6.6: Microreactor designs.

Reactor	P[MWt]	T _o [°C]
MMR [127]	15	640
eVinci [47]	5	650
ST-OTTO [45]	30	750
U-battery [28]	10	750
Starcore [94]	36	850

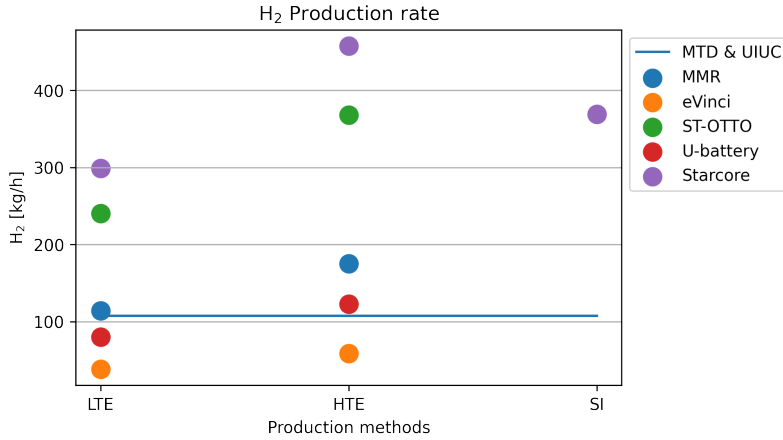
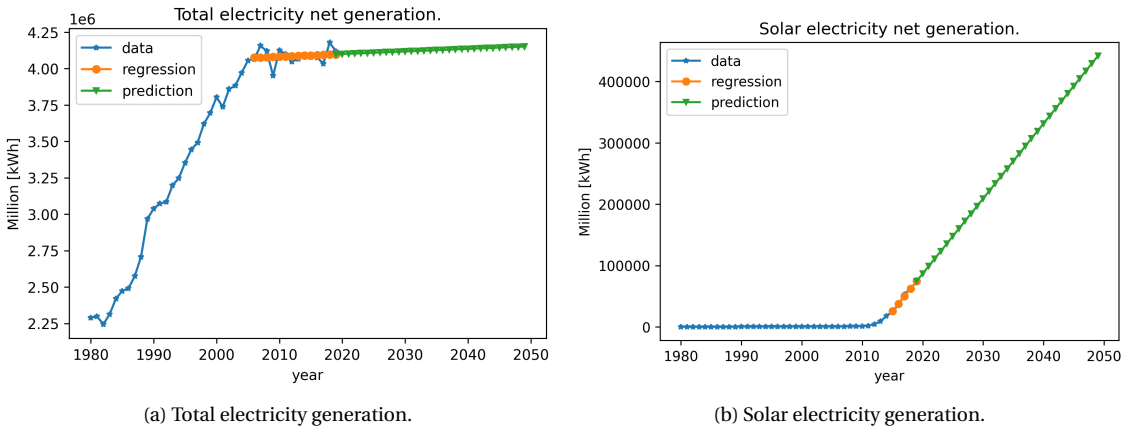


Figure 6.9: Hydrogen production rate by the different microreactor designs.

6.7.2 Electricity Generation

This subsection centers its focus on the electricity generation sector and the duck curve problem. To quantify the duck curve's magnitude, we have to predict the UIUC grid's load and the expected electricity production from solar. As the iCAP's main objective is to become carbon neutral before 2050, we make our prediction for that year. UIUC solar farm is relatively new, and more data is necessary to produce a reliable forecast. To go around this barrier, we use the available data for the whole US. Figure 6.10 displays the prediction for 2050. We carry out the prediction using a linear regression that produces the worst-case scenario. In such a scenario, the total load increases minimally, whereas the solar generation increases considerably.



(a) Total electricity generation. (b) Solar electricity generation.

Figure 6.10: Prediction of the electricity generation in the US for 2050. Data from [2].

The next step was to apply the same growth factor from the predictions to the UIUC grid's load and solar electricity. To obtain a prediction for 2050, we applied the growth factor to the hourly data. We chose a spring day when solar production is higher, as it is sunny, but the total load is low since people are less likely to use electricity for air conditioning or heating [95]. Finally, we subtracted the solar production from the total load, obtaining the net load or demand (D_{NET}).

We narrowed our analysis' focus to April 4th, when the net demand reached the lowest value in the 2019's spring. Figure 6.11 shows these results. In 2050, the peak net demand will be 46.9 MWh at 5 PM. The lowest net demand will be 15 MWh at 11 AM. These results yield a demand ramp of 31.9 MWh in 4 hours. These results show that the grid requires an available capacity of dispatchable sources of at least 31.9 MW.

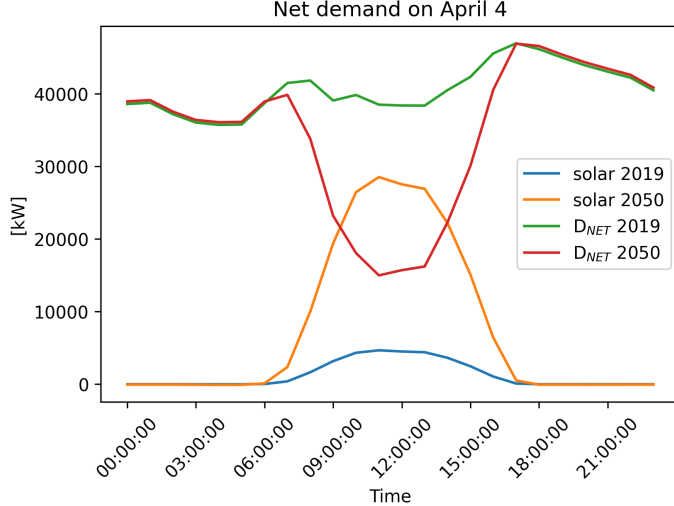


Figure 6.11: Prediction of the UIUC's net demand for 2050.

Once we calculated the net demand, the next step was to figure the over-generated electricity. For that purpose,

we arbitrarily chose a reactor of 25 MW. For the LTE case, any reactor is a valid option. We chose an η of 33%, which yields a reactor power of 75.8 MWt. For the HTE case, the reactor's choice is an HTGR with an outlet temperature of 850°C. We consider an η of 49.8%, which yields a reactor of 50.2 MWt.

The reactor operates at full capacity at all times. However, the reactor electricity (P_E) equals the net demand (D_{NET}) once smaller than 25 MW. Note that P_E has power units while D_{NET} has energy units. We chose time steps of 1 hour for our analysis, hence P_E and D_{NET} differ by the constant h . As P_E is lower than 25 MW, and the reactor is at full thermal capacity, the hydrogen plant takes the excess of thermal energy. We used equation 6.11 with equations 6.8 to 6.10 to calculate the hydrogen produced. Figure 6.12 displays the results. The total H₂ production reaches 660, 1009, and 815 kg for LTE, HTE, and SI.

$$P_E = D_{NET}$$

$$\frac{P_E}{25[MW]} = \frac{\eta\beta P_{th}}{\eta P_{th}} = \beta \quad (6.11)$$

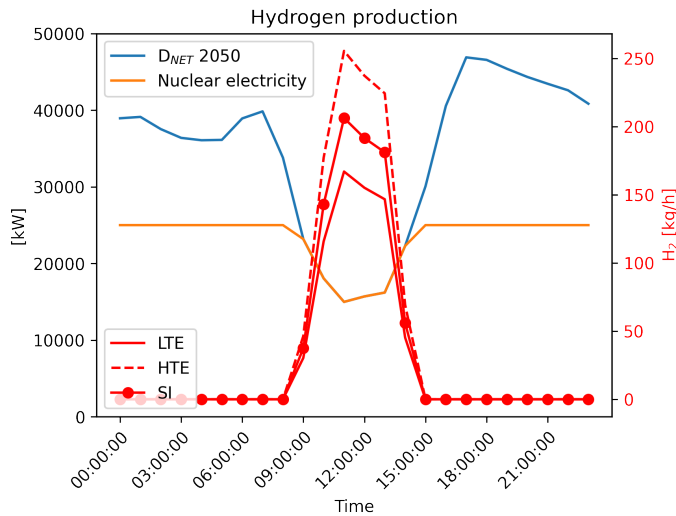


Figure 6.12: H₂ production.

Our analysis' last step is to calculate the peak demand reduction by using the hydrogen to produce electricity. The energy produced by hydrogen is 285 kJ/mol, equal to 40 kWh/kg [124]. However, conventional fuel cells can use up to 60% of that energy [35]. Knowing the mass of hydrogen produced, we calculated the total electricity produced. We reduced the peak demand by distributing the electricity over a specific range of hours. We chose to distribute the electricity for over 6 hours. We calculated the new peak using equation 6.12. Figure 6.13 shows these results. The different H₂ processes can generate 15.84 MWh, 24.2 MWh, and 19.6 MWh, respectively. This

generation accounts for a peak reduction of 5 MW, 6.4 MW, and 5.6 MW, respectively.

$$NP = \frac{\sum_{i=0}^N D_{NET,i} - TH}{N} \quad (6.12)$$

where

NP = New peak magnitude

$D_{NET,i}$ = Hourly net demand

TH = Total mass of hydrogen

N = Total number of hours if we use the H_2

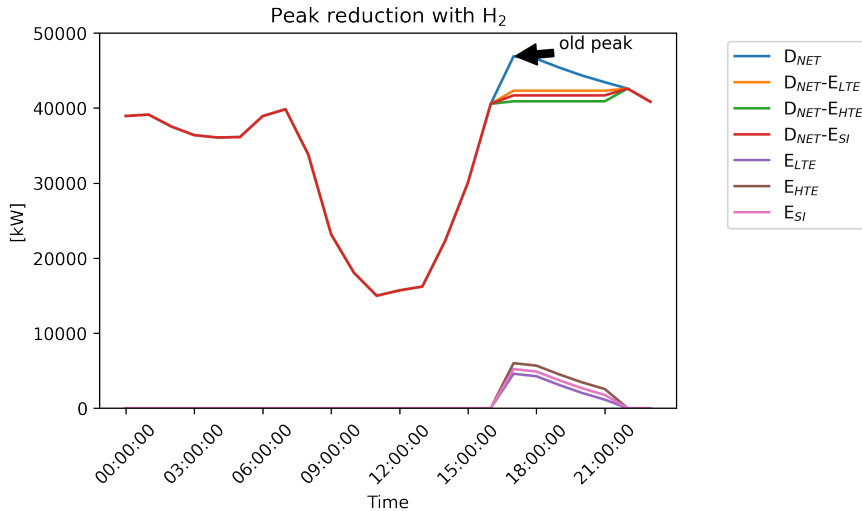


Figure 6.13: Peak reduction by using the produced H_2 .

6.8 Conclusions

The world faces energy challenges that compromise the efforts to stop climate change. The electricity generation and transportation sectors contribute the most to GHG emissions and, hence, are the major contributors to climate change. These challenges underscore the need for cleaner sources. Nonetheless, the common belief that renewable energy is the solution to the problem presents several drawbacks. The duck curve is an example of such drawbacks. Moreover, a carbon-neutral electric grid will be insufficient to halt climate change. The transportation sector needs

to survey some possible alternatives to become carbon-free as well. In this work, we proposed combining nuclear energy and hydrogen production that represents a possible solution to these challenges.

To seek a solution for the challenge described above, we narrowed down our focus on a more particular case, the University of Illinois. Through the implementation of the iCAP, the University of Illinois is actively working to reduce GHG emissions on its campus. This work's objective aligns with the efforts in two of the six target areas defined on the iCAP: electricity generation, and transportation.

Regarding hydrogen production methods, we surveyed three different processes: LTE, HTE, and SI. We developed a tool to calculate their energy requirements, regarding electricity and heat, and hydrogen production rates. This tool is applicable to a stand-alone hydrogen plant and a nuclear power plant that produces both electricity and hydrogen.

In the transportation sector analysis, we quantified the fuel requirements of MTD and UIUC fleets. We calculated the mass of hydrogen necessary to replace 100% of the fleet's fossil fuel usage. Finally, we chose several microreactor designs, and we calculated their hydrogen production rates. The microreactors that can meet both fleet hydrogen needs are the MMR, ST-OTTO, U-battery, and Starcore. The Starcore design is the only one that could use the SI process.

In the electricity generation sector analysis, we predicted the duck curves' magnitude in UIUC's grid in 2050. This result exhibits how an increased solar penetration into the grid worsens the duck curve. We proposed a mitigation strategy that uses a microreactor of 25 MWe. For such a reactor, we calculated the mass of hydrogen produced by the different methods during the day. Finally, we estimated a peak demand reduction by using the hydrogen produced during the day. This last result highlights that hydrogen introduces a means to store energy that reduces the reliance on dispatchable sources. This analysis emphasizes how nuclear energy and hydrogen production are an approach to mitigate climate change.

Chapter 7

Conclusions

7.1 Contribution

The development of the HTGR technology begun almost 60 years ago. HTGRs have several desirable features that make them a good candidate for deployment in the near-term. Some of those features are reliance on passive heat transfer mechanisms, use of TRISO particles, and high operating temperatures. Higher temperatures offer increased cycle efficiencies and enable a wide range of process heat applications, such as hydrogen production. Hydrogen can be a decisive response to energy and climate challenges, as it can decarbonize the transport and power sectors. Several hydrogen production processes benefit from high temperatures, such as high-temperature electrolysis or thermochemical water splitting. Utilizing high-temperature nuclear power plants as the energy source of the process eliminates the need to burn fossil fuels.

To support the evolution of the HTGR technology, this work focused on the extension of Moltres capabilities to prismatic HTGRs. Modeling and prediction of core thermal-hydraulic behavior is necessary for assessing the safety characteristics of a reactor. The fuel blocks' complex geometry requires elaborate numerical calculations. The characteristics of an HTGR are different from those of conventional Light Water Reactors (LWRs). Such differences demand for new reactor analysis tools. Historically, the operator-splitting technique allowed for coupling stand-alone neutronics solver to a thermal-hydraulics solver and modeling a reactor. However, solving the fully-coupled system is preferable over using the operator-splitting technique. Moltres can solve systems of equations in a fully-coupled way or solve systems of equations independently. This feature makes Moltres suitable for solving multi-physics problems and a wide range of nuclear engineering problems.

This work extends Moltres modeling capabilities to prismatic HTGRs.

Additionally, this work studied different hydrogen production that can be coupled to a nuclear power plant.

7.2 Future Work

This section introduces some possible future work as a continuation of this thesis.

- 3D Thermal-fluids - radiative heat transfer - porous media model - Multi-physics - Thermo-mechanics
- HTE with steam temperature boosting

This simplified algorithms allow for solving the mass flow rate distribution in the core for steady-state cases, and for transient cases as an approximation. However, in coupled analyses, the flow distribution depends on the temperature and will change with respect to time. This creates the necessity for developing tools integrated into Moltres. Currently, MOOSE has a module for modeling the incompressible Navier-Stokes equations. Integrating that module into the solver could improve the accuracy. This task will be part of the future work.

Appendix

8.2 Verification of the thermal-fluids model

The analytical solution of this problem is

$$T_c(r, z) = T_{in} + \frac{q_{ave} R_f^2 L}{2 \rho c_p v \pi R_c^2} \left[1 + \cos\left(\frac{\pi}{L} z\right) \right] \quad (8.1)$$

$$T_3(z) = T_c(z) + \frac{q_{ave} \pi}{2} \sin\left(\frac{\pi}{L} z\right) R_f^2 \frac{\ln(R_i/R_m)}{2k_i}$$

$$T_2(z) = T_3(z) + \frac{q_{ave} \pi}{2} \sin\left(\frac{\pi}{L} z\right) R_f^2 \frac{\ln(R_m/R_g)}{2k_m}$$

$$T_1(z) = T_2(z) + \frac{q_{ave} \pi}{2} \sin\left(\frac{\pi}{L} z\right) R_f^2 \frac{\ln(R_g/R_f)}{2k_g}$$

$$T_f(r=0, z) = T_1(z) + \frac{q_{ave} \pi}{2} \sin\left(\frac{\pi}{L} z\right) R_f^2 \frac{1}{4k_f} \quad (8.2)$$

$$T_f(r, z=L/2) = \frac{q_{ave}}{4k_f} \left(R_f^2 - r^2 \right) + T_1(z=L/2) \quad (8.3)$$

$$T_g(r, z=L/2) = \frac{T_1(z=L/2) - T_2(z=L/2)}{\ln(R_f/R_g)} \ln(r/R_g) + T_1(z=L/2) \quad (8.4)$$

$$T_m(r, z=L/2) = \frac{T_2(z=L/2) - T_3(z=L/2)}{\ln(R_g/R_m)} \ln(r/R_m) + T_2(z=L/2) \quad (8.5)$$

$$T_i(r, z=L/2) = \frac{T_3(z=L/2) - T_c(z=L/2)}{\ln(R_m/R_i)} \ln(r/R_i) + T_3(z=L/2) \quad (8.6)$$

$$T_c(r, z=L/2) = T_c(z=L/2) \quad (8.7)$$

where

T_c = bulk coolant temperature

T_{in} = inlet coolant temperature

q_{ave} = average power density

R_f = fuel compact radius

L = fuel column height

ρ = helium density

c_p = helium heat capacity

v = average helium velocity

R_c = coolant channel radius

R_g = gap radius

R_m = moderator radius

R_i = film radius

k_f = fuel compact thermal conductivity

k_g = gap thermal conductivity

k_m = moderator thermal conductivity

k_i = film thermal conductivity = $hR_i \ln(R_i/R_m)$

References

- [1] Administration, E. I. (2014). How much carbon dioxide is produced by burning gasoline and diesel fuel?
- [2] Administration, U. E. I. (2020). Electric Power Monthly with data for February 2020.
- [3] Andrs, D., Berry, R., Gaston, R., Martineau, R., Peterson, J., Zhang, H., Zhao, H., and Zou, L. (2012). RELAP-7 level 2 milestone report: Demonstration of a steady state single phase pwr simulation with relap-7.
- [4] Association, W. N. (2020). Small nuclear power reactors - World Nuclear Association.
- [5] Atomics, G. (1996). Gas Turbine-Modular Helium Reactor (GT-MHR) Conceptual Design Description Report.
- [6] Balay, Brune, Buschelman, Gropp, Karpeyev, Knepley, McInnes, C., Rupp, Smith, and Zhang (2016). PETSc Users Manual.
- [7] Ballinger, R. G., Wang, C. Y., Kadak, A., Todreas, N., Mirick, B., Demetri, E., and Koronowski, M. (2004). Balance of Plant System Analysis and Component Design of Turbo-Machinery for High Temperature Gas Reactor Systems. Technical Report 828709, Massachusetts Institute of Technology, Northern Engineering and Research.
- [8] Bandini, B. (1990). *A Three-dimensional Transient Neutronics Routine for the TRAC-PF1 Reactor Thermal Hydraulic Computer Code*. Ph.D., The Pennsylvania State University.
- [9] Benjamin Russ (2009). Sulfur Iodine Process Summary for the Hydrogen Technology Down-Selection. Technical Report INL/EXT-12-25773, 1047207, INL.
- [10] Bieder, U., Calvin, C., and Emonot, P. (2000). PRICELES: an object oriented code for industrial large eddy simulations.
- [11] Bostelmann, F., Hammer, H. R., Ortensi, J., Strydom, G., Velkov, K., and Zwermann, W. (2016). Criticality calculations of the Very High Temperature Reactor Critical Assembly benchmark with Serpent and SCALE/KENO-VI. *Annals of Nuclear Energy*, 90:343–352.
- [12] Bouillon, B. (2014). Prepared Statement of Brad Bouillon on behalf of the California Independent System Operator Corporation.
- [13] Breeze, P. (2014). Nuclear Power. In *Power Generation Technologies*, pages 353–378. Elsevier.
- [14] Brey, H. (2001). Development History of the Gas Turbine Modular High Temperature Reactor.
- [15] Brown, L., Besenbruch, G., Lentsch, R., Schultz, K., Funk, J., Pickard, P., Marshall, A., and Showalter, S. (2003). HIGH EFFICIENCY GENERATION OF HYDROGEN FUELS USING NUCLEAR POWER. Technical report, GENERAL ATOMICS (US).
- [16] Burke, P. J., Stern, D. I., and Bruns, S. B. (2018). The Impact of Electricity on Economic Development: A Macroeconomic Perspective. *International Review of Environmental and Resource Economics*, 12(1):85–127.
- [17] Cavalier, C., Damian, F., Trakas, C., and Groizard, M. (2005). Presentation of the HTR Neutronic Code System.
- [18] Cavdar, S. and Ozgener, H. (2004). A finite element/boundary element hybrid method for 2-D neutron diffusion calculations. *Annals of Nuclear Energy*, 31(14):1555–1582.

- [19] CD-Adapco (2012). STAR-CCM+ release 7.04.
- [20] Center, A. F. D. (2014). Fuel Properties Comparison.
- [21] Churchill, S. W. (1977). friction-factor equation spans all fluid-flow regimes.
- [22] Cioni, O., Marchand, M., Geffraye, G., and Ducros, F. (2005). 3D thermal-hydraulic calculations of a modular block-type HTR core. *Nuclear Engineering and Design*, 236(5-6):565–573.
- [23] Collection, R. C. C. (2003). MCNP5 Monte Carlo N-Particle Transport Code System.
- [24] Company, G. O. (1973). Nuclear Design Methods and Experimental Data in Use at Gulf General Atomic.
- [25] Damian, F. (2008). VHTR Core Preliminary Analysis Using NEPHTIS3 / CAST3M Coupled Modelling. In *Fourth International Topical Meeting on High Temperature Reactor Technology, Volume 1*, pages 419–429, Washington, DC, USA. ASMEDC.
- [26] Delp, D., Fischer, D., Harriman, J., and Stedwell, M. (1964). FLARE, A three-dimensional boiling water reactor simulator.
- [27] Demkowicz, Paul, P. (2019). TRISO Fuel: Design, Manufacturing, and Performance.
- [28] Ding, M., Kloosterman, J. L., Kooijman, T., and Linssen, R. (2011). Design of a U-Battery. Technical Report PNR-131-2011-014, Urenco, and Koopman and Witteveen.
- [29] District, C.-U. M. T. (2019). Champaign-Urbana Mass Transit District Public Records.
- [30] Dotson, S. G. and Huff, K. D. (2020). Optimal Sizing of a Micro-Reactor for Embedded Grid Systems. In *Transactions of the American Nuclear Society Student Conference*, Raleigh, N.C. American Nuclear Society.
- [31] Downar, T., Lee, D., Xu, Y., and Kozlowski, T. (2004). PARCS v2.6 US NRC Core Neutronics Simulator THEORY MANUAL.
- [32] Duderstadt, J. J. and Hamilton, L. J. (1976). *Nuclear Reactor Analysis*. Wiley, New York, 1 edition edition.
- [33] Duracz, T. (1981). A Nodal Method in Hexagonal Geometry. In *International Meeting on Advances in Mathematical Methods for Solution of Nuclear Engineering Problems*, Munich, Germany.
- [34] El-Shafie, M., Kambara, S., and Hayakawa, Y. (2019). Hydrogen Production Technologies Overview. *Journal of Power and Energy Engineering*, 07(01):107–154.
- [35] Energy, D. E. E. a. R. (2015). Fuel cells fact sheet.
- [36] EPA, U. (2020). Sources of Greenhouse Gas Emissions.
- [37] Fitzpatrick, W. (1995). *Developments in Nodal Reactor Analysis Tools for Hexagonal Geometry*. PhD thesis, University of Illinois at Urbana-Champaign, Urbana, IL.
- [38] Fitzpatrick, W. E. and Ougouag, A. M. (1992). HEXPEDITE: A Net Current Multigroup Nodal Diffusion Method for Hexagonal-z Geometry.
- [39] Gaston, D., Newman, C., Hansen, G., and Lebrun-Grandié, D. (2009). MOOSE: A parallel computational framework for coupled systems of nonlinear equations. *Nuclear Engineering and Design*, 239(10):1768–1778.
- [40] Geuzaine, C. and Remacle, J.-F. (2020). Gmsh: a three-dimensional finite element mesh generator with built-in pre- and post-processing facilities.
- [41] Grimesey, R. (1994). COMBINE/PC-A Portable ENDF/B Version 6 Neutron Spectrum and Cross Section Generation Program.
- [42] Gupta, N. K. (1981). NODAL METHODS FOR THREE-DIMENSIONAL SIMULATORS. page 23.

- [43] Hales, J., Williamson, R., Novascone, S., Perez, D., Spencer, B., and Pastore, G. (2013). Multidimensional multiphysics simulation of TRISO particle fuel. *Journal of Nuclear Materials*, 443(1-3):531–543.
- [44] Han, J. S. (2008). Sensitivity Study on the Energy Group Structure for High Temperature Reactor Analysis.
- [45] Harlan, B. (2018). X-energy Xe-100 Reactor initial NRC meeting.
- [46] HELMETH (2020). High temperature electrolysis cell (SOEC).
- [47] Hernandez, R., Todosow, M., and Brown, N. R. (2019). Micro heat pipe nuclear reactor concepts: Analysis of fuel cycle performance and environmental impacts. *Annals of Nuclear Energy*, 126:419–426.
- [48] Herranz, L., Linares, J., and Moratilla, B. (2009). Power cycle assessment of nuclear high temperature gas-cooled reactors. *Applied Thermal Engineering*, 29(8-9):1759–1765.
- [49] Huning, A. (2016). A NOVEL CORE ANALYSIS METHOD FOR PRISMATIC HIGH TEMPERATURE GAS REACTORS.
- [50] Huning, A. J. (2014). A STEADY STATE THERMAL HYDRAULIC ANALYSIS METHOD FOR PRISMATIC GAS REACTORS.
- [51] IAEA (2001). Current status and future development of modular high temperature gas cooled reactor technology.
- [52] IAEA (2003). Evaluation of high temperature gas cooled reactor performance: Benchmark analysis related to initial testing of the HTTR and HTR-10.
- [53] In, Lee, Lim, and Lee (2006). Three-Dimensional Analysis of the Hot-Spot Fuel Temperature in Pebble Bed and Prismatic Modular Reactors.
- [54] Inc., A. (2006). CFX 10.
- [55] Inc, F. (2006). FLUENT.
- [56] Incorporated, A. (2006). CFX 11 Manuals.
- [57] INL (2005). RELAP5-3D/ATHENA Code Manual.
- [58] J. E. O'Brien, C. M. Stoots, J. S. Herring, M. G. McKellar, E. A. Harvego, M. S. Sohal, and K. G. Condie (2010). High Temperature Electrolysis for Hydrogen Production from Nuclear Energy TechnologySummary. Technical Report INL/EXT-09-16140, 978368, INL.
- [59] J. Ortensi, D. Andrs, A.A. Bingham, R.C. Martineau, and J.W. Peterson (2012). Initial Coupling of the RELAP-7 and PRONGHORN Applications. Technical Report INL/EXT-12-27350, 1060984, INL.
- [60] Johnson, R. W., Sato, H., and Schultz, R. R. (2009). CFD Analysis of Core Bypass Phenomena. page 60.
- [61] Joo, H.-S. (1984). Resolution of the control rod cusping problem for nodal methods.
- [62] KAERI (2007). DeCART v1.2 User's Manual.
- [63] Kalamaras, C. M. and Efstathiou, A. M. (2013). Hydrogen Production Technologies: Current State and Future Developments. *Conference Papers in Energy*, 2013:1–9.
- [64] Kang, C. M. and Hansen, K. F. (1973). Finite Element Methods for Reactor Analysis. *Nuclear Science and Engineering*, 51(4):456–495.
- [65] Kirk, B. S., Peterson, J. W., Stogner, R. H., and Carey, G. F. (2006). libMesh : a C++ library for parallel adaptive mesh refinement/coarsening simulations. *Engineering with Computers*, 22(3-4):237–254.
- [66] Knoll, D. and Keyes, D. (2004). Jacobian-free Newton–Krylov methods: a survey of approaches and applications. *Journal of Computational Physics*, 193(2):357–397.

- [67] Krebs, J., Laigle, M., Lenain, R., Mathonniere, G., and Nicolas, A. (1990). Calculational Methods for PWRs.
- [68] Lautard, J., Loubiere, S., and Magnaud, C. (1990). CRONOS, A Modular Computational System for Neutronic Core Calculations.
- [69] Lawrence, R. (1983). The DIF3D Nodal Neutronics Option for Two- and Three-Dimensional Diffusion-Theory Calculations in Hexagonal Geometry.
- [70] Lawrence, R. (1986). Progress in nodal methods for the solution of the neutron diffusion and transport equations. *Progress in Nuclear Energy*, 17(3):271–301.
- [71] Lee, Zhong, Taiwo, Yang, Smith, and Palmiotti (2006). Status of Reactor Physics Activities on Cross Section Generation and Functionalization for the Prismatic Very High Temperature Reactor, and Development of Spatially-Heterogeneous Codes.
- [72] Lee, H., Jo, C., and Noh, J. (2008). DEVELOPMENT OF CAPP CODE BASED ON THE FINITE ELEMENT METHOD FOR THE ANALYSIS OF VHTR CORES. In *Proceedings of the 4th International Topical Meeting on High Temperature Reactor Technology*, Washington, DC USA.
- [73] Lee, H. C., Jo, C. K., and Noh, J. M. (2011). Development of the CAPP code for the Analysis of Block Type VHTRs.
- [74] Leppänen, J. (2007). *Development of a New Monte Carlo Reactor Physics Code*. PhD thesis, Helsinki University of Technology, Espoo, Finland.
- [75] Leppänen, J. (2015). Serpent – a Continuous-energy Monte Carlo Reactor Physics Burnup Calculation Code.
- [76] Leppänen, J., Aufiero, M., Fridman, E., Rachamin, R., and van der Marck, S. (2014). Calculation of effective point kinetics parameters in the Serpent 2 Monte Carlo code. *Annals of Nuclear Energy*, 65:272–279.
- [77] Lewis, E. and Dilber, I. (1986). Finite element, nodal and response matrix methods: A variational synthesis for neutron transport. *Progress in Nuclear Energy*, 18(1-2):63–74.
- [78] Lim, H. S. and No, H. C. (2006). GAMMA Multidimensional Multicomponent Mixture Analysis to Predict Air Ingress Phenomena in an HTGR. *Nuclear Science and Engineering*, 152(1):87–97.
- [79] Limited, C. D. (2004). STAR-CD Version 3.24 User Guide.
- [80] Lindsay, A., Ridley, G., Rykhlevskii, A., and Huff, K. (2018). Introduction to Moltes: An application for simulation of Molten Salt Reactors. *Annals of Nuclear Energy*, 114:530–540.
- [81] MacDonald, P. E. (2003). NGNP Point Design - Results of the Initial Neutronics and Thermal-Hydraulic Assessments During Fy-03. Technical Report INEEL/EXT-03-00870 Rev. 1, INL, Idaho Falls.
- [82] Marleau, G., Hebert, A., and Roy, R. (2016). A USER GUIDE FOR DRAGON VERSION4. page 318.
- [83] Maruyama, S., Murakami, T., Kiso, Y., and Sudo, Y. (1988). Verification of in-vessel thermal and hydraulic analysis code FLOWNET.
- [84] Melese, G. and Katz, R. (1984). *Thermal and flow design of helium-cooled reactors*. American Nuclear Society, La Grange Park, Ill., USA.
- [85] Ming, Z., Olson, A., Jiang, H., Mogadali, M., and Schlag, N. (2019). Resource Adequacy in the Pacific Northwest.
- [86] Nagashima, M. (2018). JAPAN's HYDROGEN STRATEGY AND ITS ECONOMIC AND GEOPOLITICAL IMPLICATIONS. Technical report, IFRI.
- [87] Nakano, Tsuji, and Tazawa (2008). Conceptual Reactor Design Study of Very High Temperature Reactor (VHTR) with Prismatic-Type Core.
- [88] NEA, O. (2017). Benchmark of the Modular High-Temperature Gas-Cooled Reactor MHTGR-350 MW Core Design. Technical Report NEA/NSC/R(2017)4, OECD.

- [89] NEA, O. (2020). Coupled Neutronic/Thermal- Fluid Benchmark of the MHTGR-350 MW Core Design: Results for Phase I Exercise 1.
- [90] Neylan, A., Graf, D., and Millunzi, A. (1988). The modular high temperature gas-cooled reactor (MHTGR) in the U.S. *Nuclear Engineering and Design*, 109(1-2):99–105.
- [91] NIST (2020). Thermophysical Properties of Fluid Systems.
- [92] No, H. C., Lim, H. S., Kim, J., Oh, C., Siefken, L., and Davis, C. (2007). Multi-component diffusion analysis and assessment of GAMMA code and improved RELAP5 code. *Nuclear Engineering and Design*, 237(10):997–1008.
- [93] Novak, A. J., Zou, L., Peterson, J. W., Martineau, R. C., and Slaybaugh, R. N. (2018). Pronghorn: A Porous Media Thermal-Hydraulics Core Simulator and its Validation with the SANA Experiments.
- [94] Nuclear, S. C. (2015). Star Core Spec Sheet.
- [95] of Energy, U. D. (2017). Confronting the Duck Curve: How to Address Over-Generation of Solar Energy.
- [96] of Energy Efficiency and Renewable Energy, D. O. (2020). Hydrogen Production Processes. Library Catalog: www.energy.gov.
- [97] of Illinois at Urbana-Champaign, U. (2015). Illinois Climate Action Plan.
- [98] Ortensi, J., Cogliati, J., Pope, M., Bess, J., Ferrer, R., Bingham, A., and Ougouag, A. (2010). Deterministic Modeling of the High Temperature Test Reactor with DRAGON-HEXPEDITE. In *Proceedings of HTR 2010*, Prague, Czech Republic.
- [99] O'Brien, J. E., Herring, J. S., Stoots, C. M., McKellar, M. G., Harvego, E. A., Condie, K. G., Housley, G. K., and Hartvigsen, J. J. (2010). Status of the INL High- Temperature Electrolysis Research Program – Experimental and Modeling. In *Fourth Information Exchange Meeting on the Nuclear Production of Hydrogen*, page 13.
- [100] Park, H., Knoll, D. A., Gaston, D. R., and Martineau, R. C. (2010). Tightly Coupled Multiphysics Algorithms for Pebble Bed Reactors. *Nuclear Science and Engineering*, 166(2):118–133.
- [101] Pater, M. (2019). Multiphysics simulations of Molten Salt Reactors using the Moltres code. Master's thesis, Universite Paris-Saclay, Copenhagen, Denmark.
- [102] Ragusa, J. C. and Mahadevan, V. S. (2009). Consistent and accurate schemes for coupled neutronics thermal-hydraulics reactor analysis. *Nuclear Engineering and Design*, 239(3):566–579.
- [103] Reitsma, F., Han, J., Ivanov, K., and Sartori, E. (2008). The OECD-NEA/NSC PBMR400 MW coupled neutronics thermal hydraulics transient benchmark - Steady-state results and status.
- [104] Reza, S. M., Harvego, E., Richards, M., Shenoy, A., and Pddicord, K. (2006). Design of an Alternative Coolant Inlet Flow Configuration for the Modular Helium Reactor.
- [105] Rohde, U., Baier, S., Duerigen, S., Fridman, E., Kliem, S., and Merk, B. (2012). Development and verification of the coupled 3D neutron kinetics/thermal-hydraulics code DYN3D-HTR for the simulation of transients in block-type HTGR. *Nuclear Engineering and Design*, 251:412–422.
- [106] Sanchez, Hebert, Stankovski, Coste, Loubiere, der Gucht, V., and Zmijarevic (1999). APOLLO2 Twelve Years Later.
- [107] Sato, H., Johnson, R., and Schultz, R. (2010). Computational fluid dynamic analysis of core bypass flow phenomena in a prismatic VHTR. *Annals of Nuclear Energy*, 37(9):1172–1185.
- [108] Shenoy, A. and McEachern, D. (1974). HTGR Core Thermal Design Methods and Analysis.
- [109] Silady, F., Cunliffe, J., and Walker, L. (1988). The licensing experience of the Modular High-Temperature Gas-Cooled Reactor (MHTGR). *Energy*, 16(1-2):417–424.

- [110] Simoneau, J.-P., Champigny, J., Mays, B., and Lommers, L. (2007). Three-dimensional simulation of the coupled convective, conductive, and radiative heat transfer during decay heat removal in an HTR. *Nuclear Engineering and Design*, 237(15-17):1923–1937.
- [111] Stainsby, R. (2008). Investigation of Local Heat Transfer Phenomena in a Prismatic Modular Reactor Core. Technical report, AMEC NSS Limited.
- [112] Stamml'er, R. (1998). HELIOS Methods.
- [113] Strydom, G., Bostelmann, F., and Yoon, S. J. (2015). Results for Phase I of the IAEA Coordinated Research Program on HTGR Uncertainties. Technical Report INL/EXT-14-32944, 1173079, INL.
- [114] Strydom, G., Ortensi, J., Sen, S., and Hammer, H. (2013). INL Results for Phase I and III of the OECD/NEA MHTGR-350 Benchmark.
- [115] Studer, E., Beccantini, A., Gounand, S., Dabbene, F., Magnaud, J., Paillère, H., Limaiem, I., Damian, F., Golfier, H., Bassi, C., and Garnier, J. (2007). CAST3M/ARCTURUS: A coupled heat transfer CFD code for thermal-hydraulic analyzes of gas cooled reactors. *Nuclear Engineering and Design*, 237(15-17):1814–1828.
- [116] Tak, Kim, Lim, and Noh (2012). A practical method for Whole-Core Thermal Analysis of a Prismatic Gas-Cooled Reactor.
- [117] Tak, N.-i., Han, T. Y., and Lee, H. C. (2016a). Coupled Neutronics and Thermo-Fluid Simulation of Full-Core Prismatic Gas-Cooled Reactor Using DeCART/CORONA Code System. In *Transactions of the Korean Nuclear Society Autumn Meeting*, page 4, Gyeongju, Korea.
- [118] Tak, N.-i., Kim, M.-H., and Lee, W. J. (2008). Numerical investigation of a heat transfer within the prismatic fuel assembly of a very high temperature reactor. *Annals of Nuclear Energy*, 35(10):1892–1899.
- [119] Tak, N.-i., Lee, H. C., Lim, H. S., and Han, T. Y. (2016b). CAPP/GAMMA+ code system for coupled neutronics and thermo-fluid simulation of a prismatic VHTR core. *Annals of Nuclear Energy*, 92:228–242.
- [120] Tak, N.-I., Lee, S. N., Kim, M.-H., Lim, H. S., and Noh, J. M. (2014). DEVELOPMENT OF A CORE THERMO-FLUID ANALYSIS CODE FOR PRISMATIC GAS COOLED REACTORS. *NUCLEAR ENGINEERING AND TECHNOLOGY*, page 14.
- [121] Takada, E., Nakagawa, S., Fujimoto, N., and Tochio, D. (2004). Core thermal-hydraulic design. *Nuclear Engineering and Design*, 233(1-3):37–43.
- [122] Travis, B. W. and El-Genk, M. S. (2013). Thermal-hydraulics analyses for 1/6 prismatic VHTR core and fuel element with and without bypass flow. *Energy Conversion and Management*, 67:325–341.
- [123] Tyobeka, B., Reitsma, F., and Ivanov, K. (2011). HTGR REACTOR PHYSICS, THERMAL-HYDRAULICS AND DEPLETION UNCERTAINTY ANALYSIS: A PROPOSED IAEA COORDINATED RESEARCH PROJECT. In *International Conference on Mathematics and Computational Methods Applied to Nuclear Science and Engineering*, Rio de Janeiro, Brazil. American Nuclear Society.
- [124] Ursua, A., Gandia, L. M., and Sanchis, P. (2012). Hydrogen Production From Water Electrolysis: Current Status and Future Trends. *Proceedings of the IEEE*, 100(2):410–426.
- [125] US-DOE (2019). The Ultimate Fast Facts Guide to Nuclear Energy. Fact Sheet DOE/NE-0150, Department of Energy Office of Nuclear Energy, Washington D.C. <https://www.energy.gov/ne/downloads/ultimate-fast-facts-guide-nuclear-energy>.
- [126] USDRIVE (2017). Hydrogen Production Tech Team Roadmap.
- [127] USNC (2019). MMR - USNC.
- [128] Varney, P. (2020). Personal Communication.

- [129] Wagner, M. R. (1989). Three-Dimensional Nodal Diffusion and Transport Theory Methods for Hexagonal- z Geometry. *Nuclear Science and Engineering*, 103(4):377–391.
- [130] Wang, Y., Rabiti, C., and Palmiotti, G. (2011). Krylov Solvers Preconditioned with the Low-Order Red-Black Algorithm for The Pn Hybrid FEM for the INSTANT Code. In *International Conference on Mathematics and Computational Methods Applied to Nuclear Science and Engineering*, Rio de Janeiro, Brazil.
- [131] Wang, Y., Schunert, S., and Laboure, V. (2019). Rattlesnake Theory Manual.
- [132] White, F. (2006). *Viscous Fluid Flow*. McGraw Hill, third edition.
- [133] Yildiz, B. and Kazimi, M. (2006). Efficiency of hydrogen production systems using alternative nuclear energy technologies. *International Journal of Hydrogen Energy*, 31(1):77–92.
- [134] Yuk, Cho, Jo, Tak, and Lim (2020). Time-dependent neutron diffusion analysis using finite element method for a block-type VHTR core design.